FABRICATION OF ARRAYS OF BALLISTIC EPITAXIAL GRAPHENE NANORIBBONS

A Dissertation
Presented to
The Academic Faculty

By

Dogukan Deniz

In Partial Fulfillment
of the Requirements for the Degree
Doctor of Philosophy in the
School of Physics

Georgia Institute of Technology

May 2018

FABRICATION OF ARRAYS OF BALLISTIC EPITAXIAL GRAPHENE NANORIBBONS

Approved by:

Dr. Walter de Heer, Advisor
School of Physics
Georgia Institute of Technology

Dr. Zhigang Jiang
School of Physics
Georgia Institute of Technology

Dr. Phillip First
School of Physics
Georgia Institute of Technology

Dr. Martin P. Mourigal
School of Physics
Georgia Institute of Technology

Dr. Azad Naeemi
School of Electrical and Computer Engineering
Georgia Institute of Technology

Date Approved: March 15, 2018

The real voyage of discovery consists not in seeking new landscapes, but in having new eyes.

Marcel Proust

to My Parents

ACKNOWLEDGEMENTS

Thanks to the following people for their support during my studies.

My advisors: Walt de Heer and Claire Berger.

The thesis committee: Zhigang Jiang, Phillip First, Martin Mourigal and Azad Naeemi.

My lab mates and the people I worked with: Yue Hu, Jean-Philippe Turmaud, Yiran Hu, Jamey Gigliotti, John Hankinson, Pierre Poujaud, James Palmer, Yuxuan Jiang and Patrick Gartland.

Special people, friends I met in Atlanta and at Georgia Tech: Amy Luseni, Travis Tune, Karl Lundquist, Keshav Joshi, Stephen Spitz and Thanassis Stavropoulos.

My friends from Minnesota: Robert and Ani Flagler.

Lifelong friends who are always there: Emrah Ilbey, Arda Atakol and Yigit Tuncel.

And my family: Tulay and Bayram Deniz, Oguzhan Deniz, and the new member of our family Duru Deniz.

TABLE OF CONTENTS

LIST OF TABLES

LIST OF FIGURES

LIST OF SYMBOLS AND ABBREVIATIONS

0_+	The Long Ballistic Channel
0_-	The Short Ballistic Channel
Λ_i	Mean Free Path
E_F	Fermi Level
G_o	Quantum Conductance
R_c	Contact Resistance
$R_{interface}$	Interface Resistance
R_{lead}	Lead Resistance
R_o	Quantum Resistance
R_{sheet}	Sheet Resistance
V_F	Fermi Velocity
AC	Armchair Edge Ribbon
aC	Amorphous Carbon
AFM	Atomic Force Microscopy
ALD	Atomic Layer Deposition
CCS	Confinement Controlled Sublimation

CMP	Chemical and Mechanical Polishing
CNT	Carbon Nanotube
CVD	Chemical Vapor Deposition
DOS	Density of States
Epigraphene	Epitaxial Graphene on SiC
FET	Field Effect Transistor
GNR	Graphene Nanoribbon
h-BN	Hexagonal Boron Nitrite
LEED	Low-Energy Electron Diffraction
LFM	Lateral Force Microscopy
MAN	ma-N Negative Tone Photoresist
MMA	Methyl Methacrylate
PMMA	Polymethyl Methacrylate
PVD	Physical Vapor Deposition
RIE	Reactive Ion Etching
SEM	Scanning Electron Microscopy
STM	Scanning Tunneling Microcope
SWGNR	Sidewall Epitaxial Graphene Nanoribbon
TLM	Transmission Line Method
UHV	Ultra High Vacuum

ZZ Zig-Zag Edge Ribbon

SUMMARY

Epitaxial graphene nanoribbons have recently demonstrated exceptional one dimensional ballistic transport where charge carriers can travel without scattering up to $16\mu m$ at room temperature (STM probes in UHV). These transport properties are not yet fully understood, and they can only be exploited if nanoribbons can be produced at large scale with good properties in ambient conditions. Following up on these results, in this thesis I will summarize my work on arrays of epitaxial graphene nanoribbons grown on the sidewalls of trenches and steps of silicon carbide. I will discuss nanoribbon growth, nanofabrication, factors that affect nanoribbon transport and how mean free paths larger than one micron are consistently found at room temperature for thousands of nanoribbons.

CHAPTER 1
INTRODUCTION AND BACKGROUND

After Brillouin classified the symmetries of crystals in the early 19^{th} century, the discovery of the Hall effect and the discovery of electrons by Thomson indicated that a greater theory of charge carriers was needed to explain the electronic conduction in metals. This challenge was first taken on by Drude and an electronic theory of solids was introduced with the theoretical description of metals [1]. After the discovery of superconductivity in mercury in 1911 by H.K. Onnes [2], and the utilization of X-rays to understand the crystal structures by M von Laue [3] and W.H. and W.L. Bragg [4] has been established, new pieces were added to the puzzle of the theory of electrons in a solid. Later with the development of quantum mechanics, the quantum theory of an electron in a solid took its basic shape, resulting in the establishment of condensed matter/solid state physics.

Condensed matter physics [5, 6] solves the wave functions of charge carriers in a crystal by considering the quantum mechanical nature of the particles under the periodic potential of a crystal, which comes from the symmetry of its lattice. This solution leads to Bloch waves [7], from which the dispersion relation can be derived. The dispersion relation can tell us about the conduction properties of crystals. It can show us whether the material has available bands to transmit an electron or if the transmission is blocked at some point. Depending on this gap in the band structure, the crystal can be classified as a metal, semi-conductor, insulator or semi-metal.

In the early second half of the 19th century, developments such as phenomenological theory of superconductors [8] and the theory of superconductivity [9] garnered condensed matter extensive attention. Advancements in device fabrication and measurement techniques enabled the studies of lower dimensional electronic systems.

2D electron systems [10] at AlGaAs/GaAs interfaces have been studied in great detail

due to the fact that it enables observation of conductance quantization and Landau levels [11]. AlGaAs/GaAs mediums also enabled the study of correlated charge carrier motions in the form of fractional quantum Hall effect [12]. Fullerenes as quantum dots [13] and carbon nanotubes as quantum wires [14] were introduced as low dimensional electron systems on crystals. Following the conductance quantization experiments, the transport features of fast charge carriers in 1D strips of a 2D electron gas [15] were observed. Later these transport features have been observed on 1D crystals (carbon nanotubes [16]). This led to the realization that ultrafast ($V_F = 10^6 m/s$) electrons can be obtained on a crystal and this can be confirmed/tested by transport measurements and spectroscopy. Such a crystal was therefore claimed to be useful for the study of quantum field theory in laboratories.

Since the invention of transistors [17] and the development of integrated circuits, the feature size of electronic components in an integrated circuit has been following Moore's law. Intrinsic limitations due to the properties of Si and the shrinking size of transistors are expected to be reached in the near future [18]. Integration of materials with high electronic mobility [19] (up to $250000 cm^2 V^{-1} s^{-1}$ while preserving the high charge density $10^{12} cm^{-2}$) into the transistor fabrication can offer an alternative solution to the demand in faster electronics and can address long-term technology needs. In order to utilize such a technology, an understanding of the transport phenomena in these materials needs to be established.

1.1 Carbon Crystals

Due to its chemical properties carbon can form many allotropes (Figure 1.1). Diamond (Figure 1.1 (a)) is one of the best known due to its unique mechanical properties. It has sp-3 bonds between every carbon atom in the crystal. It is the hardest material and it is a good thermal conductor, yet it is a wide bandgap semiconductor in terms of electrical conduction and has a bandgap of nearly 5.5 eV. This makes a diamond an ideal heat sink for electronic applications. It is mostly mined from carbon rich areas, where it is assumed to

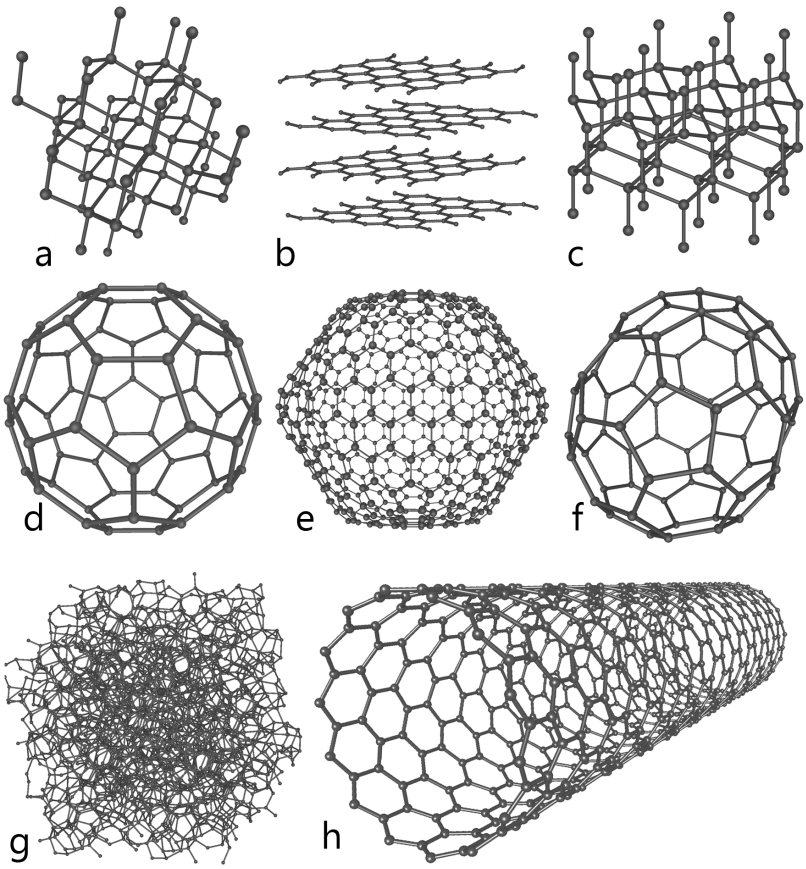

Figure 1.1: Allotropes of Carbon. a) Sp-3 bonded Diamond. The unit cell is a face centered cubic with two atom basis. b) Graphite: Sp-2bonded Graphene layers connected with sp-3 bonds. c) Lonsdaleite, d-e-f) various Fullerenes, g) Amorphous Carbon, h) Carbon Nanotube. Reprinted from [20], Copyright 2018 by Wikipedia, The Free Encyclopedia.

experience extremely high pressures and high temperatures at some point in the geological cycle. Synthetic diamonds are produced by mimicking those conditions in lab environments. Chemical vapor deposition (CVD) growth techniques can produce high quality diamond samples.

Another common allotrope of carbon is graphite (Figure 1.1 (b)). Graphite has stacked layers of graphene that has sp-2 bonds between its carbon atoms. Individual graphene layers are pinned to each other by sp-3 bonds throughout the graphite crystal. This stacking is called Bernal stacking [21] and it is what differs multilayer graphene from graphite [22]. Since the early 20^{th} century, graphite has been defined as a semiconductor with zero ac-

tivation energy (same as the semi-metal in the recent literature) (by Wallace, PR [23] and Slonczewski, JC [24]).

Fullerene is a graphene sheet that is folded over into the shape of a soccer ball (Figure 1.1 (d-e-f)) while a carbon nanotube (CNT) is rolled over into the shape of a tube. Single walled versions of these stable structures have been extensively studied as quantum dots [25, 26] for fullerenes and quantum wires in the case of CNTs [27, 28].

1.2 Graphene

Graphene is a 2D hexagonal lattice of carbon atoms that are connected in a honeycomb structure. The carbon to carbon bond length in graphene is 0.142nm. The high surface charge and unique electronic properties come from the fact that each carbon atom makes only three π bonds (sp-2) in plane. The p orbitals (σ - sp-3 bonds) that is above of every carbon atom give rise to the high mobility under the high charge density feature of graphene.

1.2.1 Theoretical Background

Tight binding calculations show that graphene has linear bands at K points and these linear bands form what is called Dirac cones. A simple tight binding calculation for two atoms A and B forming two basis atoms of a unit cell can be done by first considering the amplitudes of the wave functions at these points are $(\Psi_A, \Psi_B)^T$. Assuming electrons can hop between the nearest neighbor sites with a hopping strength a, the Hamiltonian can be written as:

$$H_0(\mathbf{k}) = \begin{pmatrix} 0 & h(\mathbf{k}) \\ h^\dagger(\mathbf{k}) & 0 \end{pmatrix}, \tag{1.1}$$

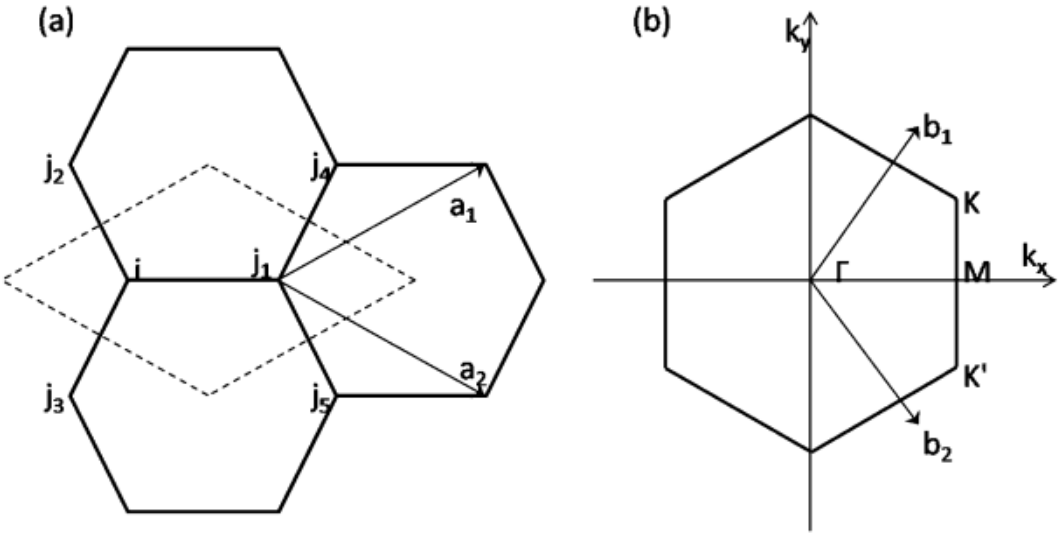

Figure 1.2: (a) Unit cell of graphene, vectors $\vec{a_1}$ and $\vec{a_2}$ show the vectors that surround the two atoms that form the basis for the lattice. (b) Reciprocal space vectors $\vec{b_1}$ and $\vec{b_2}$ showing the first Brillouin zone for graphene. Γ, K and M points show the trajectory where dispersion relation is generally calculated on. K and $K^{'}$ points are the locations for the Dirac points. Reprinted from [29], Copyright 2011 by Royal Society of Chemistry.

where $\mathbf{k} = (k_x, k_y)$ and $h(\mathbf{k})$ can be defined as:

$$h(\mathbf{k}) = a \sum_i \exp\left(i\,\mathbf{k}\cdot\mathbf{a}_i\right) . \tag{1.2}$$

where $\mathbf{a}_i$ are the vectors to the nearest neighbors in the real space. By introducing Pauli matrices σ, the Hamiltonian can be written as:

$$H_0(\mathbf{k}) = t_1 \sum_i \left[\sigma_x \cos(\mathbf{k}\cdot\mathbf{a}_i) - \sigma_y \sin(\mathbf{k}\cdot\mathbf{a}_i)\right] . \tag{1.3}$$

the resulting energy spectrum $E(\mathbf{k}) = \pm\,|h(\mathbf{k})|$ gives Dirac cones at K and $K^{'}$.

For any material the band structure (Energy vs Momentum) defines the group velocity of the charge carriers. The term effective mass ($m_{\text{eff}}^{-1} = \frac{1}{\hbar^2}\frac{\partial^2 E}{\partial k^2}$) is introduced in this sense to explain the mass, particles experience under the periodic potential of the crystal.

In the case of linear bands ($E = \hbar v_{\text{F}}|k|$) the Dirac equation [31] needs to be used to

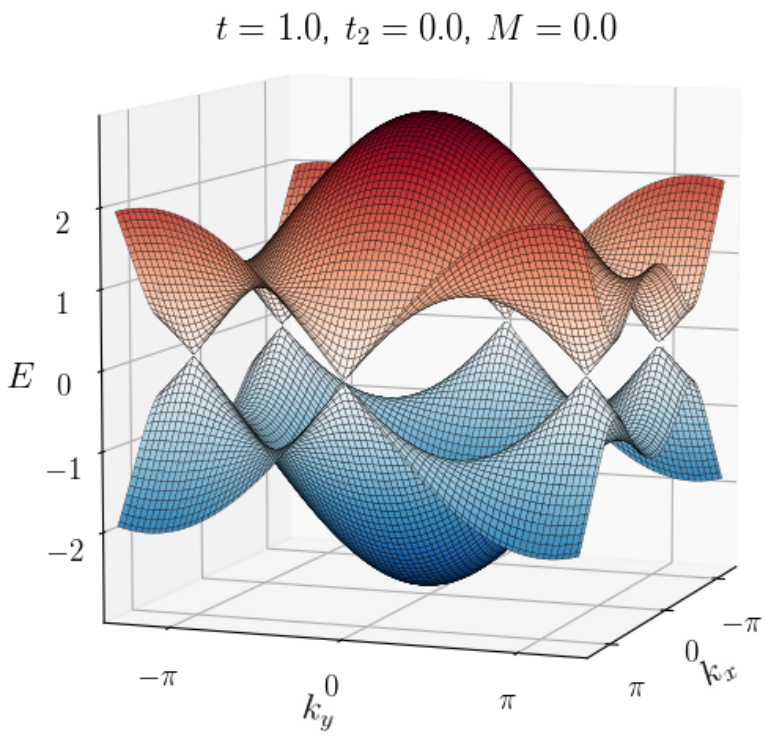

Figure 1.3: Energy spectrum calculated from the tight binding model that is summarized from equation 1.1 to 1.3. K and $K^{'}$ points are at locations $\mathbf{K} = (2\pi/3, 2\pi/3\sqrt{3})$ and $\mathbf{K}' = (2\pi/3, -2\pi/3\sqrt{3})$. Reprinted from [30], Copyright 2018 by TU Delft OpenCourseWare.

analyze the dynamics of charge carriers [32]. For the linear bands in a 2D graphene crystal, the effective mass is undefined close to special points in the reciprocal lattice. Dirac point in a crystal can manifest itself as a minimum conduction at the charge neutrality point in a Hall measurement and as half integer steps in a quantum Hall system. An observation of such an effect requires a setup where the charge density of the system can be varied from a minimum, while longitudinal and transverse resistance measurements can be taken. However, a thin graphite system can present the same features [33], therefore along with the transport measurement, crystallographic data of the system needs to be presented to make sure that the system is a 2D crystal.

Another approach that reveals unique transport features of the crystal is the analysis of symmetries with the group theory. Detailed studies that investigate the symmetries of fullerene and CNTs are explained in M. S. Dresselhaus' book [34]. The group wave vector **k** at reciprocal space points Γ, K and M are respectively D_{6h}, D_{3h} and D_{2h}. On the triangle that goes as Γ – K – M in the reciprocal space (Figure 1.2 (b)), the symmetry is C_{2v} [35]. From all the irreducible representations of these symmetry characters, the space group analysis of graphene that reveals the band structure from another angle [36], can be done.

1.2.2 Experimental Realization

Due to quantization of the cyclotron orbits, in any 2D electron system a perpendicular magnetic field creates discrete energy levels known as Landau levels. For the case of 2D systems that have a Dirac-like spectrum (linear-photon like bands), fluctuations with the applied magnetic field in the form of Shubnikov-de Haas oscillations are expected to be observed [37]. Measurements of Shubnikov-de Haas oscillations were presented from 2004 to 2006 [38, 39, 40] for graphene along with structural order and low-energy electron diffraction (LEED) measurements that prove the 2D nature of the crystal. At higher field half integer quantization in a quantum Hall system and a conduction minimum at the charge neutrality point has been experimentally shown and the results of the measurement

has been attributed to charge carriers of graphene in 2005 [41].

Graphene's charge carriers are also tunable through raising or lowering of the Fermi level in the vicinity of the charge neutrality point. This feature stems from the strong variation in the density of states (DOS) in the vicinity of the Dirac point. The DOS variation can be probed in band structure measurements with STM [42].

In order to open a bandgap or to study the exotic phases of transport, several graphene based devices are extensively being investigated. These devices consist of either stacked graphene layers that are generally protected or isolated by additional h-BN layers, or narrow graphene ribbons. Functionalized graphene with attached molecules on atoms is also used for this purpose.

Bi-layer graphene [43] has been considered a potential candidate for tunable bandgap [44] applications. Rotationally-stacked bilayer graphene [45] at some precise rotation angles (1.08° for instance) is predicted to open a bandgap [46]. Intrinsic unconventional superconductivity [47] and correlated insulator behaviour at half-filling [48] have been observed close to these bandgaps, outlining a very rich variety of transport behavior.

Another approach to open a bandgap in graphene is the anti-dot lattice method [49, 50]. The anti-dot lattice method requires a triangular array of holes that are carved in planar graphene. Holes can be fabricated either lithographically or by using focused ion beam. However, both methods suffer from contamination and doping problems. Nevertheless developments in nano-fabrication has enabled analysis of various hole sizes (few nanometers) and lattices.

Graphene nanoribbons (GNRs) are quasi one dimensional graphene with lateral quantum confinement [51, 52]. The confinement causes quantization of the transverse momentum, which leads to one dimensional sub-bands (Figure 1.4) and bandgap openings for certain edge directions and widths. Additional calculations have been performed using more sophisticated methods and they confirm the gap opening in nanoribbons [53]. Gap opening was also experimentally observed in narrow ribbons prepared from chemi-

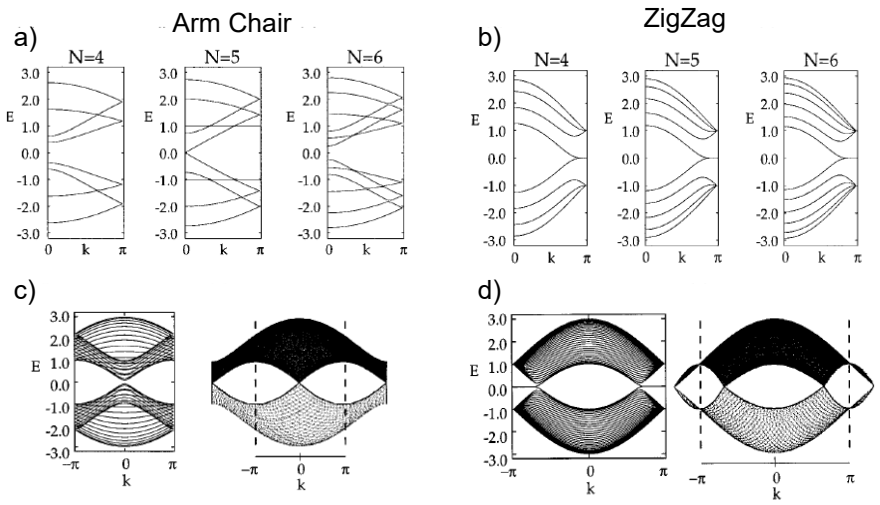

Figure 1.4: The band diagram in Zig-Zag and Armchair graphene nanoribbons resulted by quantum confinement. (a)-(b) Band diagrams as for different ribbon widths (N= number of atoms). Opening of a bandgap for Armchair and the flat band condition for Zig-Zag ribbons can be seen for certain widths. (c)-(d) Projected band diagram and the boundary of the Brillouin zones (Dashed lines). Reprinted from [51], Copyright 1996 by American Physical Society.

cal precursors [54]. Intervalley and intravalley scatterings [55] are possible between the sub-bands. In addition to the semi conducting features of narrow graphene ribbons, larger ribbon widths ($\approx 40nm$) exhibit ballistic transport which hadn't been theoretically predicted and still hasn't been fully understood. Detailed explanation of GNRs are summarized throughout the whole thesis starting from the following section.

1.3 Graphene Nanoribbons

GNRs are strips of planar graphene with a specific edge chirality. Tight binding calculations show a bandgap opening [51, 52, 31, 53] in GNRs and the effect of the certain edge terminations on electronic transport properties. Theoretically Zig-Zag (ZZ) (Figure 1.5 (a)) ribbons are found to always be metallic and Armchair (AC) ribbons (Figure 1.5 (b)) can sustain a bandgap up to a certain width [51](Figure 1.4, $< 0.5eV$). Numerical studies made on the edge morphology show the effects of substrate-induced edge disorder and hydrogen

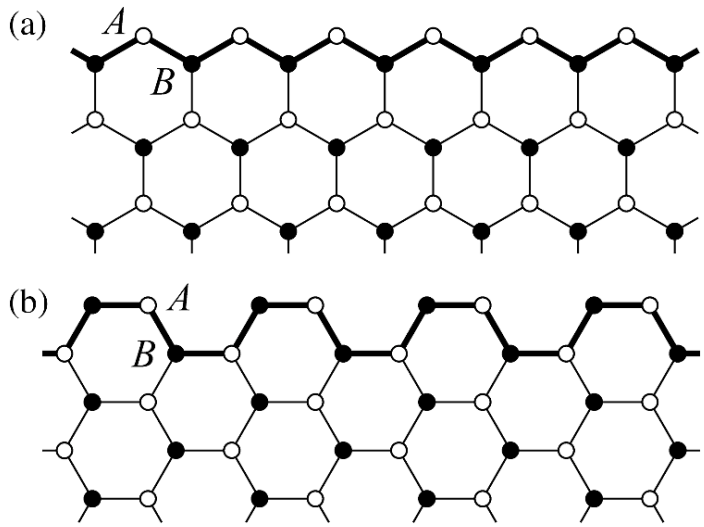

Figure 1.5: Two types of edge terminations in GNRs (a) Zig-Zag and (b) Armchair. Reprinted from [64], Copyright 2012 by International Society for Optics and Photonics.

termination of the ribbon edges on the transport properties [56]. Similar studies made on CNTs show the effects of vacancies or divacancies introduced by ion etching [57] and the effects of impurities introduced by doping [58].

GNRs can be obtained in various methods, they can be lithographically obtained from planar graphene by using a mask and etching the excess graphene. Resist masks [59] and ZnO rod masks have been used in this purpose [60]. Even though thin strips of graphene can be achieved using these methods, both edge roughness and fabrication residues pose problems for transport studies [61]. Furthermore, exposing the edges to chemicals and/or dry etching can cause unwanted doping of the material which also affects the transport features [62, 63]. Once exposed or doped, the system needs to be high temperature compatible to be annealed (for undoping purposes).

Precursor polymers are also used to produce GNRs [54] with atomically precise edge termination. Even though the edge termination was highly precise, and uniform widths (nine atom and ten atom AC ribbons) can be obtained, scalability and directionality problems emerge from the synthesis approach just like it did for CNTs. Getting single walled CNTs with a defined chirality from thousands of CNTs synthesized by a CVD type of

method requires an efficient separation method. Therefore, CNTs produced by CVD is not considered at this day as a scalable method of production for CNT based individual transistors. Similarly, isolating synthesized ribbons from many others in its surroundings suffers from the same problem [65, 66].

Sidewall epitaxial graphene nanoribbons (SWGNRs) [67, 68] on SiC propose a scalable GNR production method that does not need transfer of the ribbon to an insulating substrate. Narrow strips of graphene can be produced on SiC by etching mesas onto the surface prior to the epitaxial graphene (Epigraphene) growth. The sidewalls of the etched structures host GNRs on their sidewalls. Few examples [69] other than SWGNRs offer GNRs grown on a not conducting substrate.

Initial studies on GNRs had focused on engineering a bandgap either by shaping/narrowing the ribbon, by functionalizing the graphene or by using the SiC/SiO_2 as the transport medium [70] (with the goals towards showing a graphene example of energy-efficient and tunnel field-effect transistors [71, 72]). Tunneling transistors made with metal nanoparticles [73] exhibit Coulomb blockade and the Kondo effect. Graphene analogs of such transistors contain a tiny gap between two graphene leads, for example a gap that can be obtained by using an electromigrated gold nano-constriction [74] as a mask [75]. In the next step, the continuous graphene underneath can be etched to form an opening and the constriction then can be chemically removed.

The tunneling gap approach also enables creating graphene nano-particles that might act as quantum dots (In the example of [76], a $2nm$ wide and $20nm$ long dot has a bandgap of $0.38eV$).

Realization of GNR transistors require high trans-conductance (conductivity of the device at the *on* state), high on/off ratios (the ratio of the resistances of *on* and *off* states) with a complete off state. Fabricating epigraphene-based transistors needs a change of paradigm. One of the ideas is to tunnel through a semi-conductor grown epitaxially in a physical gap managed between two ballistic ribbons. For this we first need to be able to

grow epigraphene nanoribbons consistently and then grow them at large scale. Once the growth conditions and electronic properties of the resulting GNRs can be correlated the conditions for ballistic transport can be determined.

The ballistic transport feature of graphene has only been observed on SWGNRs on SiC, probably due to its clean production methods that does not require further processing of the material. These features make it easier to keep graphene clean and unexposed. Graphene on other platforms, like on SiO_2, introduces puddle surface potential variations (charged impurity centers causing isolated puddles of charge carriers acting as quantum dots with 50 to 80 meV) [77].

The performance of ribbons can be analyzed with field effect transistors (FETs) made of GNRs. FETs made of lithographically patterned ribbons on exfoliated graphene show carrier localization effects [78, 77] similar to disordered narrow-bandgap semiconductors [79]. FETs made of narrow SWGNRs on SiC are shown to be similar to (well-behaved) narrow-bandgap semiconductors [80], although it is not clear whether it is a transport gap or a bandgap. High temperature capability of the SiC platform in principle enables edge smoothing capability either by high temperature annealing or through SWGNR growth optimization.

In order to understand and model the physics of the ballistic transport phenomena in SWGNRs, further measurements are needed. This brings in the fabrication challenge of putting reliable contacts on GNRs, which will be addressed throughout this thesis. The performance projections of ballistic graphene field effect transistors was made by Liang, G. et al. [81] and any realization of such devices requires scalable and reproducible production methods.

Prior measurements by Ruan, M. et al [82, 83, 84] show characteristics of a quasi one dimensional–single channel transport that is ballistic. The current model and the ballistic transport phenomena will be summarized after an introduction to the ballistic transport phenomena.

1.4 The Landauer Equation

The equivalence of conduction and the transmission coefficient through a channel was first introduced by Landauer [85] and it forms the basis of the mesoscopic transport theory. The Landauer equation gives the conductance as:

$$G = \frac{e^2}{h} \sum_{i}^{n} \gamma_i T_i, \tag{1.4}$$

where the sum is over the n conduction channels (modes), γ_i is the degeneracy of each channel, T_i is their transmission coefficient and $\frac{e^2}{h}$ is the quantum of conduction. In the case there is scattering in the channel of length L, with Λ_i the mean free path,

$$T_i = \frac{\Lambda_i}{\Lambda_i + L}. \tag{1.5}$$

Since all the channels conduct in parallel, the resistance of a system can be written as the inverse of sum of the conduction channels as:

$$R = \frac{h}{e^2} (\sum_{i}^{n} \gamma_i \frac{\Lambda_i}{\Lambda_i + L})^{-1}, \tag{1.6}$$

which turns into:

$$R = \frac{h}{e^2} \frac{1}{\sum_i^n \gamma_i \frac{\Lambda_i}{\Lambda_i + L}} = \frac{h}{e^2} \frac{1}{\sum_i^n \gamma_i (1 + \frac{L}{\Lambda_i})^{-1}}. \tag{1.7}$$

For a single channel, degeneracy $\gamma = 1$, this sum turns into:

$$R = \frac{h}{e^2} (1 + \frac{L}{\Lambda_o}), \tag{1.8}$$

where (as defined in Datta's book [86]) $\frac{h}{e^2}$ is the *contact resistance* and the $\frac{h}{e^2} \frac{L}{\Lambda_o}$ part is the *actual resistance* of a channel.

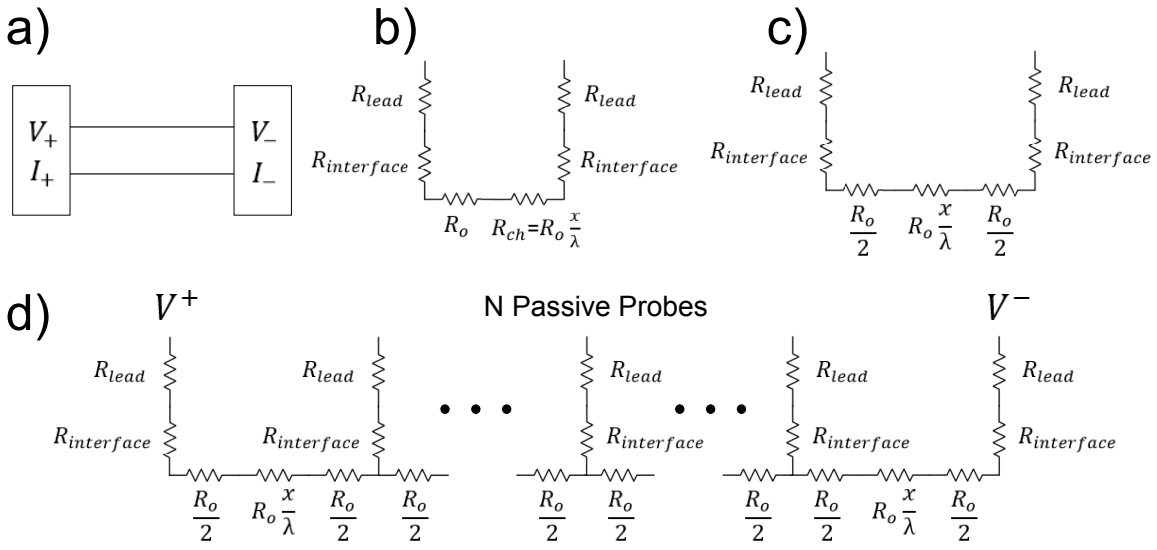

Figure 1.6: a) A two point measurement setup. b) A circuit diagram showing the resistances involved. The additional interface resistance corresponds to GNR contact interface, since this point contact resistance can have a high value. c) The equivalent circuit when the resistance R_o is split and associated with each contact. d) When N passive probes are added to the channel, from each contact the resistance R_o adds up to the system. This is shown on the left and right sides of a contact as $R_o/2$.

The resistance of a single channel system that is contacted with N passive probes can be represented by the circuit diagrams of Figure 1.6. Figure 1.6 (a)-(c) show a two probe system where the contact resistances and R_o are indicated on equivalent circuits. Upon adding multiple invasive passive probes (N) (Figure 1.6 (d)), the resistance between the far left and the far right contact takes the form of $R_N = NR_o + R(L) + 2R_{interface} + 2R_{lead}$, where $R_{interface}$ measures the transparency of the contact.

Figure 1.7 shows the circuit diagram of N parallel channels each with a mean free path Λ_i. If one of these channels has a relatively longer mean free path Λ_o compared to the others, then in the long length regime, the transport is dominated by this channel. To illustrate this effect, in Figure 1.7 (b) 50 channels with mean free paths of $5nm$ are assumed to be parallel to one with mean free path $20\mu m$. The resulting resistance vs length profile shows that the effect of the diffusive channels only shows up at short length. At long length scales, the slope of the resistance vs length plot (of 51 parallel channels) is very close to the slope of a single channel nanoribbon that only contains the ballistic channel (by ballistic

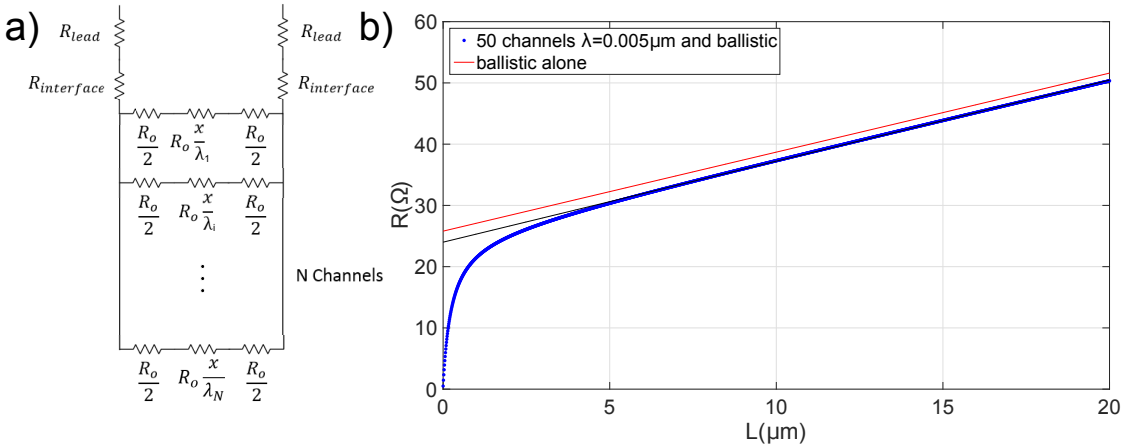

Figure 1.7: a) When N parallel transport channels are added to the channel with each channel having mean free path Λ_i. b) If a ballistic channel exist in parallel with many other diffusive channels, then the ballistic channel dominates in the long channel limit. Red: a single channel system with a $20\mu m$ mean free path. Blue: when 50 channel with $5nm$ mean free paths are added parallel to the ballistic channel. Here $R_{interface} = 0$ and $R_{lead} = 0$.

we mean here $\Lambda_o \gtrsim L$). For N parallel channels, the length dependence of resistance in the long regime can be approximated as:

$$R(L) \approx \frac{h}{e^2}\frac{L}{\Lambda_{max}}. \tag{1.9}$$

From resistance vs length measurement data, the mean free path can be extracted using:

$$\Lambda_o = \frac{R_o}{\frac{dR(L)}{dL}}. \tag{1.10}$$

An interpolation of the resistance vs length data in the form of $R(L) = aL + b$ can be used to find the mean free path Λ_o. Inserting the slope of the linear fit into the equation 1.10 gives R_o/a as the mean free path (a with units of $k\Omega/\mu m$). The constant b in the linear fit can be used to find the contact resistance, similar to the transmission line method (TLM) method (which is normally in the form of $R_{TLM}(L) = 2R_c + R_{Sheet}L/W$). The contact

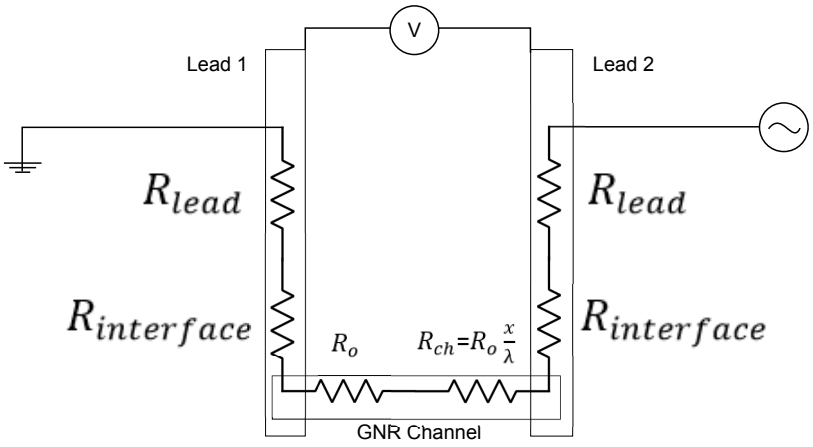

Figure 1.8: The two point measurement setup and the involved resistances. λ in this drawing represents the long channel length mean free path Λ_{max}.

resistance R_c in a two point measurement for a single channel is in the form of :

$$R_c = R_o + 2R_{lead} + 2R_{interface}, \tag{1.11}$$

where R_{lead} in the lead resistance of the pads. The schematic in Figure 1.8 shows these resistances on a contacted nanoribbon. As is clear from Figure 1.7, the contact resistance from the linear fit of R vs L at long length (blue line) is $\alpha R_o + 2R_{interface} + 2R_{lead}$ where α can be anywhere between 1 and $\frac{1}{N}$.

1.5 Ballistic Transport in Graphene Nanoribbons

Ballistic–scattering free–transport happens when the transport length is shorter than the mean free path of electrons in that medium (Figure 1.9). GNRs and CNTs can have mean free paths on the order of couple μm at room temperature, which makes an observation of the ballistic transport possible for these mediums [84, 16]. Couple μm long mean free path in room temperature is exceptional compared to the mean free paths of highly conductive metals at room temperature that can only reach a maximum of $50nm$ [88].

2014 study by Baringhaus, Ming, et al [84] demonstrate the ballistic transport in SWGNRs [67]. A surprising result is that transport has both length and temperature dependence. Today,

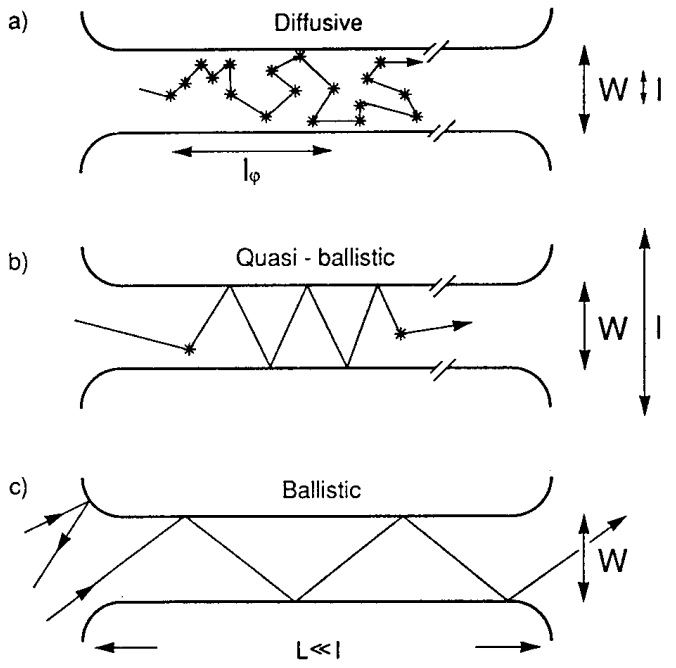

Figure 1.9: Comparison of the mean free paths (l) to width (W) for diffusive (a), quasi-ballistic (b) and ballistic mediums (c). The length L is much smaller than the mean free path for the ballistic picture. Reprinted from [87], Copyright 1988 by Springer Verlag.

further measurements and interpretations suggest a more detailed description to temperature and length dependence of the ballistic transport channels.

For a further insight of transport, additional measurements require arrays of contacted ballistic SWGNRs on a chip, so that these chips can be transferred to other measurement tools for further experiments. However, as it will be detailed in the next chapter, SWGNRs are very susceptible to external conditions. Exposure to air and organic resist residues from nanofabrication can affect the ribbon mean free paths. Therefore, experimental challenges mainly consist of growing better quality SWGNRs and handling samples the right way to minimize or avoid any type of contamination on the graphene surface.

The details of the current model are given in the next section, experimental techniques that are planned for the device fabrication and the following measurements are presented in the following chapters.

1.5.1 The Current Model

The first four probe measurements on charge neutral graphene ribbons at Georgia Tech Epitaxial Graphene Lab in 2012 revealed an exceptional ballistic behavior as reported in [83]. Later, detailed UHV four point probe measurements are made at Leibniz Universität Hannover in collaboration [89] with J. Baringhaus and C. Tegenkamp, extended these results and showed exceptionally long (up to $16\mu m$) ballistic transport range [84]. In charge neutral ribbons, tight binding calculations show that two electronic bands cross the Fermi level (E_F) (named 0_+ and 0_-). These first two bands, in the quantum confinement introduced sub-bands of GNRs (Figure 1.4), are attributed to the ballistic transport in SWGNRs.

Energy levels of a confined ribbon of width W and length L are approximately defined as [51, 90, 84]:

$$E_{n,m} = \pm\hbar c^* \sqrt{\left(\frac{n\pi}{W}\right)^2 + \left(\frac{m\pi}{L}\right)^2}. \tag{1.12}$$

Where the Fermi velocity $c^* = 10^6 m/s$. $E_{1,0}$ energy is proportional to $1/W$ and $E_{0,1}$ is proportional to $1/L$. Taking $W = 40nm$ and $L = 1\mu$m (like in our ribbons, as it will be presented later) gives the first two energy levels: $\frac{E_{1,0}}{k_B} = 600K$ and $\frac{E_{0,1}}{k_B} = 23K$. This shows that $E_{1,0}$ is active at room temperature while $E_{0,1}$ is not. For larger ribbons ($W = 200nm$) $E_{1,0}$ temperature goes down to $120K$. For lengths of $100nm$, $E_{0,1}$ is activate at room temperatures.

In the case of one dimensional ribbon, following the Landauer equation [91], the conductance can be written as $G = 4G_o \sum Tr_n$ [86] (where $G_o = e^2/h$ and the quantum conductance $\frac{2e^2}{h}$ is replaced with $\frac{e^2}{h}$ since the degeneracy is lifted for the ribbon samples [84], the underlying physical mechanism of this symmetry breaking is still unknown), where the transmission coefficient $Tr_n = 0$ for $|E_{n,0}| > |E_F|$ and transport is dominated by n edge states (for charge neutral ribbons) when $Tr_n < 1$ for $|E_F| < |E_{1,0}|$ (with $T < 600K$). On the order of one micron long ballistic conduction is expected for charge neutral, low-defect

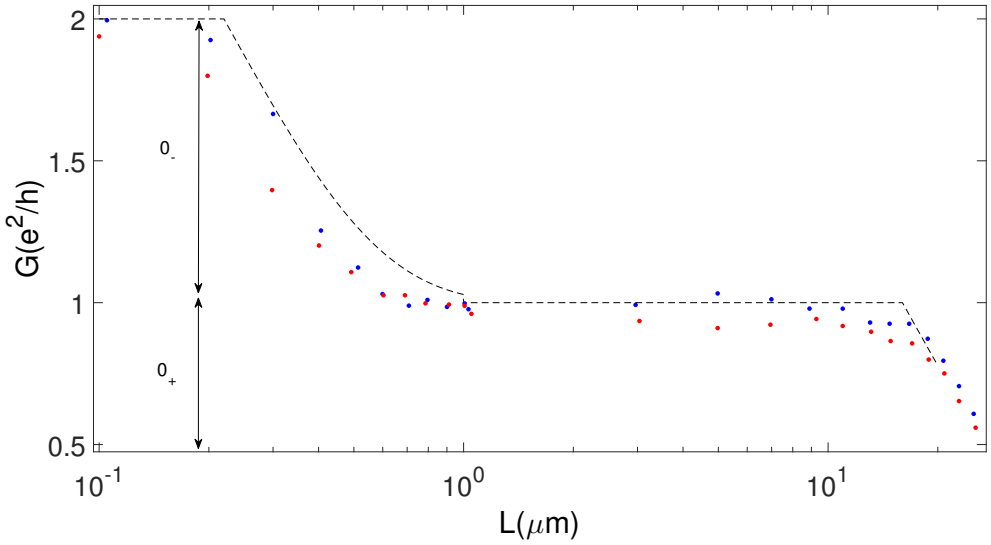

Figure 1.10: Equation 1.13 (dashed) and the digitized data of four ribbons from the ballistic transport paper [84] (measurement by J. Baringhaus and C. Tegenkamp).

SWGNRs [38].

Experimental results of the ballistic conduction measured in [84] are given in Figure 1.10. The corresponding conduction value, $1G_o$ is due to injection by a probe into a one channel conductor. This value being the only resistance $(1/G_o)$ in the system and preserving its value over some distance indicates scattering free transport of electrons in the given length scale ($\approx 1\mu m - 16\mu m$). At lower length scale ($L < 1\mu m$), the conduction $1G_o$ increases up to $2G_o$, which means that another conduction channel activates and adds $1G_o$ to the conduction. Even though the conduction is quantized on two plateaus, the transition between these plateaus is not discrete, but in the form of a decay. This indicates that one channel (0_-) is activated at low length scale ($L < 1\mu m$) and dies out as the length is increased, the following channel (0_+) can survive for a much longer distance $(1\mu m - 16\mu m)$.

The data in Figure 1.10 can be fit into a set of equations by specifying some critical lengths, where decays begin, $L^*_{0_-} = 220nm$ and $L^*_{0_+} = 16\mu m$. The conductance for the

given length scales follow the dependencies:

$$\mathrm{G} = \begin{cases} 2G_o & , L \leq 0.22\mu m, \\ G_o + G_o exp(1 - L/L^*_{0\_}) & , 0.22\mu m \leq L \leq 1\mu m, \\ G_o & , 1\mu m \leq L \leq 16\mu m, \\ G_o exp(1 - L/L^*_{0_+}) & , L \geq 16\mu m. \end{cases} \tag{1.13}$$

In the same paper [84], a $1.6\mu m$ ribbon is gated at different temperatures and the shift of Dirac's point is used to model the temperature dependence of conduction channels. Obtained data is shown to be fitting to the equation:

$$G(T) = \alpha \frac{e^2}{h} \left[1 + 0.5 exp \left\{ - \left(\frac{T^*}{T_{el} - T_0} \right)^{1/2} \right\} \right] \tag{1.14}$$

where $\alpha = 0.922$, $T^* = 21.5K$, $T_0 = 2.2K$ and T_{el} is the electron temperature. T^* is defined in terms of length as:

$$T^* = \frac{1.4\pi\hbar c^*}{k_B L} \tag{1.15}$$

which is $20.9K$ for $L = 1.6\mu m$. The $1/2$ factor in the exponent in equation 1.14 comes from variable range hopping [92]. The coefficient 1.4 in equation 1.15 is due to graphene to graphene contact used in the specific experiment [83]. Later it is found out that with metal contacts the conductance follows a simple exponential and the 1.4 factor becomes 1.

Since $k_B T^* = E_{n,m} = \pm\hbar c^* k$ and the wave vector k can be approximated as $\frac{m\pi}{L}$, the temperature can be written as $k_B T^* = \pm\hbar c^* \frac{m\pi}{L}$.

A slight bias voltage dependence (V_b) of conductance is attributed to electronic heating of carriers. This heating process is defined in the equation as T_{el}. Once this T_{el} is obtained from the conduction data by using Equation 1.14, this experimental T_{el} data fits into

equation:

$$T_{el} = \sqrt{T^2 + (T_{Vb}/v)^2}, \tag{1.16}$$

where $T_{Vb} = eV_b/k_B$ and, $v = 5$ for $T_{el} < 15K$ and $v = 12$ for $T_{el} > 15K$.

Another observation, which is not highlighted in the paper but can be found in the supplementary information, is about magneto-conductance of ballistic ribbons. A 5% positive linear magneto-conductance up to $B = 2T$ was observed.

Additionally the equivalence of two and four point probe measurements and resistance doubling due to passive probes are presented as evidences of SWGNRs being single channel conductors [93, 86]. A similar experiment is carried out in [15] where four-terminal resistance of a ballistic quantum wire was measured.

Combining all these observations in [84], we can conclude that SWGNRs are quasi one dimensional, single channel conductors with ballistic transport features. The ballistic transport observed in epigraphene nanoribbons is currently not fully understood. The two transport channels 0_+ and 0_- and the length scales that these channels are activated remain a mystery. Also it is not yet clear where the dominant transport happens on a GNR, the edge or the bulk of the system can have significant (or non significant) roles in the transport. The substrate GNRs lay on might have a factor in their transport properties.

Further measurements require an SWGNR platform that allows access to the ballistic transport features to perform full scale measurements. This demands placement of contacts on SWGNRs. In this thesis I will investigate the factors that ballistic transport relies on and then I will introduce nanofabrication techniques that doesn't disturb the intrinsic ballistic properties of SWGNRs.

1.6 Thesis Outline

This study can be categorized into three main parts: Graphene growth, nanofabrication and the transport measurements. In order to be able to use the nomenclature and mention the techniques comfortably in the later chapters, characterization and measurement methods are presented first in the next chapter (Chapter 2). Problems that can occur during processing are discussed and the experimental planning to overcome such problems is shown. The third chapter consists of dynamics of graphene growth and the methods developed to control them. The following chapter consists of transport measurements done on contacted GNRs. First, mean free paths of SWGNRs are analyzed to see if they fall into the ballistic range, then factors that affect the mean free paths are analyzed. Temperature dependent resistance measurements and contact resistances are also presented in the same chapter.

CHAPTER 2
EXPERIMENTAL METHODS

Building micro (or nano) devices to study electronic, magnetic, mechanical and photonic properties of graphene requires an extensive consideration of surface physics and engineering challenges. Graphene's single atomic layer geometry makes it susceptible to crystal imperfections, fabrication residues and air contamination. It is also challenging to contact graphene and preserve the electronic conduction or the interface resistance after the contact is established.

Conventional fabrication challenges of graphene are elevated for the case of SWGNRs, since quasi one dimensional SWGNRs can be 10 to 100 nm wide while being 200 nm to 50 μm long. The nanofabrication process flow needs to yield contacted nanoribbons performing consistently for the given geometry. The chance of failure or the chance of obtaining obscured data quickly rises in case of a miscalculated step in the fabrication that might result in residues, bad crystal growth, interface problems or contamination. Therefore, all steps in the process flow, from single crystal SiC wafers to contacted epigraphene nanoribbons, need to be strategically optimized for the most consistent outcome.

Fabricating a contacted GNR, from cleaning the SiC chips to the final measurement of the ribbon, can take up to ten steps. The process flow of the nanofabrication will be presented after the main characterization techniques are introduced in this chapter.

2.1 Characterization

Characterization of planar graphene can be made through various techniques. Ellipsometry can tell how many layers of graphene are present on the surface, while Raman spectroscopy [94, 95] can give some rough information about the number of layers, but also the quality of the graphene and the strain and doping graphene experiences [96]. Such changes

are reflected as position shifts in the Raman peaks of graphene, which relates to the electronic and phonon band structure. Also detection of the buffer layer (Figure 3.4) can be made by simply observing the existence of the corresponding peaks in the spectrum.

LEED can be used to obtain diffraction peaks that indicate the underlying crystallographic structures. Graphene on SiC has a distinguishable pattern that makes it easy to determine if it is a buffer or monolayer on the Si face. Auger electron spectroscopy, scanning tunneling spectroscopy and X-ray photo-electron spectroscopy are other techniques that can be used to identify graphene and the underlying structures.

2.1.1 Atomic Force Microscopy

Narrow nature of SWGNRs makes it harder to characterize the ribbon compared to planar graphene samples [65]. Therefore, microscopy plays an important role in identifying the surface coverage of graphene. Even though it is slow compared to low voltage scanning electron microscope (SEM) imaging, AFM scans give clear contrasts between graphene regions and non-graphene SiC areas. Also SEM scans leave marks on scanned graphene areas, due to the exposure of the surface to high levels of electron beam (which is assumed to be depositing carbon based materials on the surface). This effect can be observed once a previously scanned section on the sample is revisited. The damaging effect of E-beam irradiation has also been reported [97].

Different AFM methods have been used to observe graphene on SiC. Among these electrostatic force microscopy and lateral force microscopy (LFM) are the ones that give the clearest contrasts. In terms of imaging consistency and high resolution LFM has been the main method used to identify the morphology of SWGNRs. Details of the LFM technique are given in appendix.

2.1.2 Conductive Probe Spectroscopy

Combining LFM -contact mode scanning- with the surface potentiometry requires a conducting contact mode tip. Commercially available metal coated contact mode tips can be utilized into an LFM system to probe the surface electrical potential. Applying a bias through a SWGNR and mapping the potential difference between the AFM tip and the ground contact can tell us about the voltage profiles of individual ribbons.

Potentiometry results are given in the Experimental Measurements chapter and details of the setup is explained in appendix. Collecting surface potentiometry data along with LFM and surface topography helps with one to one matching and comparison of the potential distribution and the surface morphology. Contribution of individual nanoribbons and graphene sidearms (to be explained in the next chapter) to the conduction can be revealed using this method. The method can also be used to identify which nanoribbons makes good contacts with the pads that the bias voltage is applied through. Switching the bias voltage can show the difference between the ribbons that look like an equipotential vs current carrying nanoribbons (Figure 4.6, Figure 4.7 and Figure 4.8). A sketch of the setup is given in Figure 4.5 and additional details about the method are given in appendix.

2.2 Nano-Fabrication

Conventionally any nano-fabrication consists of two main steps. Lithography and the follow up deposition or etching process. In between the fabrication steps some cleaning methods need to be deployed. On the industrial scale, chemical mechanical polishing is applied between consecutive steps. Unprocessed wafers can also go through other planarization steps like H-etching or high temperature annealing.

Working with graphene requires an uttermost consideration of the contamination and exposure effects. Leaving graphene exposed to air shows that the resistance increases up to a saturation point after which it fluctuates slightly. Reduced graphene oxide is proposed as

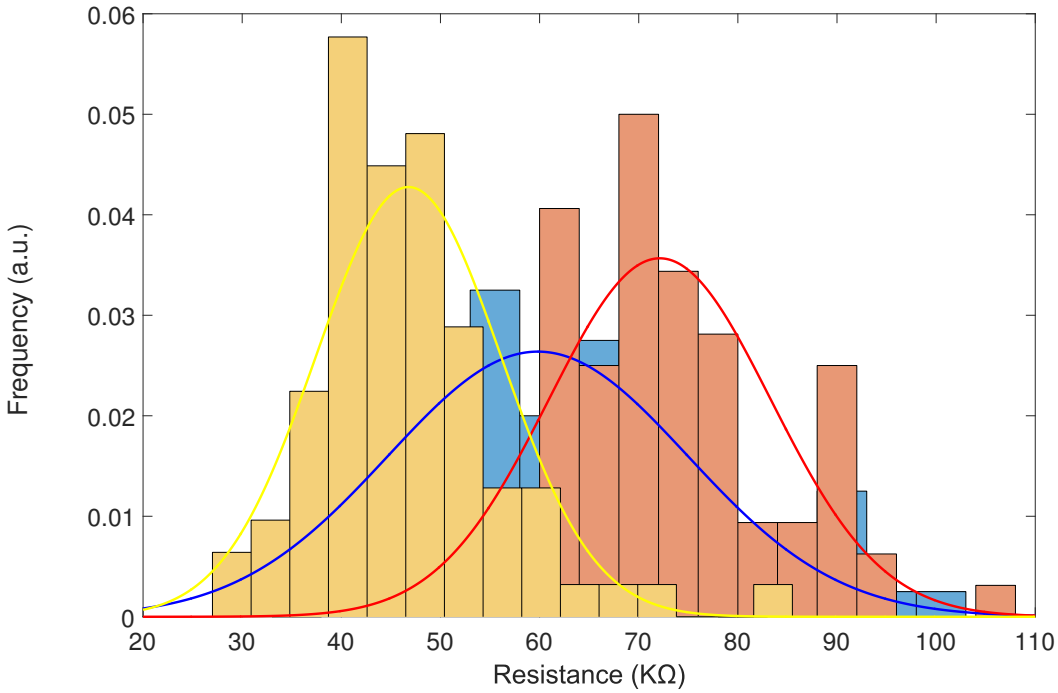

Figure 2.1: Resistance histograms of 80 same length ($5\mu m$) ribbons measured at different times and conditions. Measurements done in vacuum probe station after an annealing done in the same environment, gives the smallest uncertainty in the measurement. Blue: Measurements done right after growth, in air. Red: Measurements done one day after growth, in air. Yellow: Measurements done in vacuum probe station after annealing ($400\ ^{\circ}C$) and cooling back to room temperature.

room temperature gas sensors in this sense [98].

Figure 2.1 shows the resistance measurements made over 80 SWGNRs. $5\mu m$ long SWGNRs are measured in three different conditions to show that air exposure can drastically affect a resistance measurement. Right after the epitaxial growth, SWGNRs show the blue distribution with a high standard deviation. The red distribution shows that after air exposure for one day, overall resistance values increase and the resistance deviation decreases due to a collective saturation. Once these samples are put in vacuum ($10^{-6}mbar$), annealed at $400\ ^{\circ}C$ and measured in vacuum without exposing the samples to atmospheric conditions, the yellow profile, which has the lowest resistance mean and the lowest deviation, can be obtained.

The measurement in Figure 2.1 only shows the effects of air exposure to SWGNRs.

Upon using organic resists for lithography purposes, resist residues accumulate on graphene surfaces and these residues can alter the material by doping it and creating scattering centers [99, 100, 101]. In order to avoid such effects, conventional wet cleaning methods can be used to remove organic contaminants. Using resist remover or acetone can clean residues up to a point, but the process can still cause doping. Especially using organic resists as masks for Reactive Ion Etching (RIE) can result in polymerized resist residues that are relatively harder to remove (Figure 2.10).

The first step in the conventional SWGNR production is the RIE etching of mesas. Since there is no graphene on the surface prior to this step sonication can be used to remove hardened resist residues. However, sonication can not be used once graphene is on the surface because it damages contact pads and the graphene itself.

2.2.1 Etching

RIE etching can be used to etch shapes on the SiC surface. Lithographically produced soft resist masks can be used to etch up to 60 nm deep mesas. Deeper structures might need hard masks (metal masks like Ni) that later need to be removed with acids.

For the case of SWGNRs a lithography step comes before the RIE etching, but since the mesa structure is generally simple –long rectangles with desired densities– the lithography process will only be explained for the fabrication of the contact pads, not the mesa structure.

1:4 mixture of SF_6 and O_2 gas flow (0.8 SCCM to 3.2 SCCM) at $100W$ RF power is used for 14 to 20 seconds to etch 20 nm deep mesas structures. The non uniform resist profile can create artificial facets on the sidewalls. Depending on the resist edge sharpness, $20\,^\circ$ to $80\,^\circ$ steep mesas can be obtained. Neglecting this variable can cause an unknown starting point (the initial mesa sidewall angle) for the SWGNR growth and as it can be seen from Figure 3.9 that the initial conditions can create the difference between overgrown and undergrown graphene ribbons.

Dry etching is also used to isolate ribbons. 16W RF power and 4 SCCM O_2 gas flow

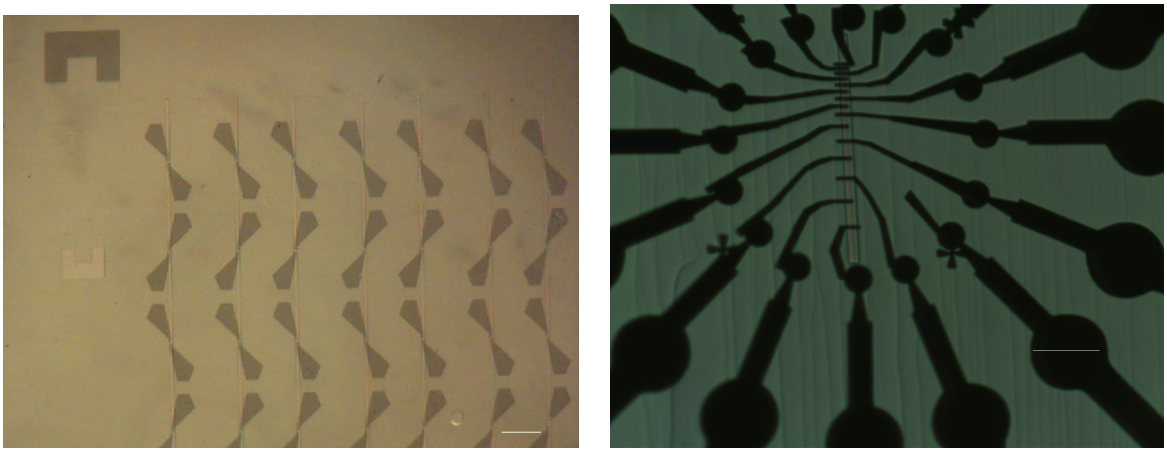

Figure 2.2: Etching patterns of two contact natural step ribbons (left) and four contact SWGNRs (right). The dry etch process removes the other graphene ribbons and prevents short circuiting. The scale bar on the left image is $50\mu m$ and the right bar is $15\mu m$ long.

is used for this purpose, a few seconds of etching time is enough to remove graphene from the surface, however the formation of the plasma can take longer than that, therefore twenty seconds of etching time is used. Figure 2.2 shows the isolation mask patterns for nanoribbons.

Shaping of Hall bars can be done with a dry etching procedure as well (Figure 2.10(a)). Patterned Hall bars on monolayer graphene on SiC can be etched into the shape and then a heat treatment can be applied for smoothing the rough edges.

2.2.2 Lithography

Ideally keeping the lithography and other processing steps before the graphene growth is the preferred strategy for the fabrication on SWGNRs (Figure 2.3). However, for the use of metal contacts, high growth temperatures ($1500\ ^{\circ}C$) can easily cause melting. Therefore, metal contacts are deposited after SWGNR growth. The alternative path is the use of amorphous carbon contacts which can survive the graphene growth temperatures and can be placed on the surface before the high temperature growth process. The trade off is metal contacts can be selected to have low contact resistance [102] and lead resistance; while carbon contacts have high lead resistance and they are not good at merging with narrow

stripes of graphene (especially for the case of natural step ribbons where the width is not well controlled).

The patterning recipes for the used lithography techniques and organic resists (like methyl methacrylate (MMA) and Poly(methyl methacrylate) (PMMA) (both from Micro Chem)) are given in detail in appendix.

2.2.3 Contacts and Liftoff

After the patterning of contact areas, Pd(20 nm)/Au(40 nm) layers are deposited on graphene with a home built e-beam evaporator. As it can be seen from the work function differences between metals and graphene [102] (Figure 2.4) Ti can also be added to this layer by layer structure to achieve better contact to graphene. After the deposition in low pressure ($10^{-6} mbar$), the samples are put in a warm acetone bath ($60\ ^{\circ}C$) for 2 hours. Acetone baths longer two hours don't show any recognizable difference in terms of the liftoff success.

A short IPA dipping and drying with Nitrogen are the last steps of liftoff. If the liftoff (of the resist along with the metal layer on top) hasn't happened during the bath, it usually happens during an additional acetone spaying. If it fails again, it generally is an indication of a problem with another parameter (organic resist, e beam dosage, spin coat recipe, baking temperature).

The use of bilayer resist profiles helps with the liftoff step. MMA layer develops faster than the PMMA layer on top and this creates an undercut region. This feature is mainly used for shadow evaporation techniques where metal deposition is done at multiple steps in different angles to create junctions that are smaller than the design. This way the patterning capability of the lithography system can be overcome by a simple geometry. The undercut feature is also useful when the deposition is unidirectional, which means not only the top or the bottom of the resist gets coated but the sidewalls get coated as well. This inhibits the penetration of removers (acetone) to these areas and the liftoff step might fail if the walls are fully covered. Increasing the sidewall area increases the chances of a successful liftoff.

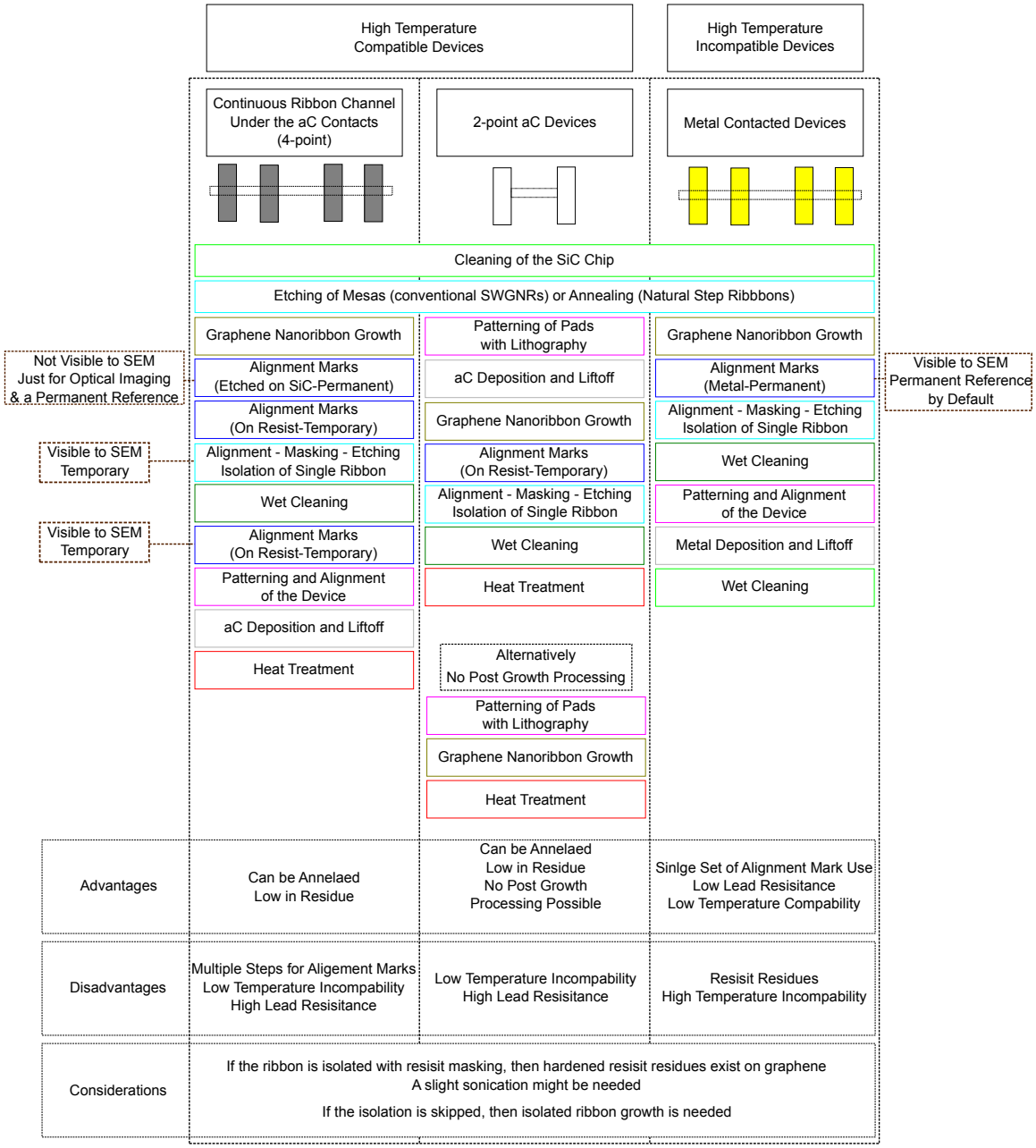

Figure 2.3: The process flow chart for various fabrication methods.

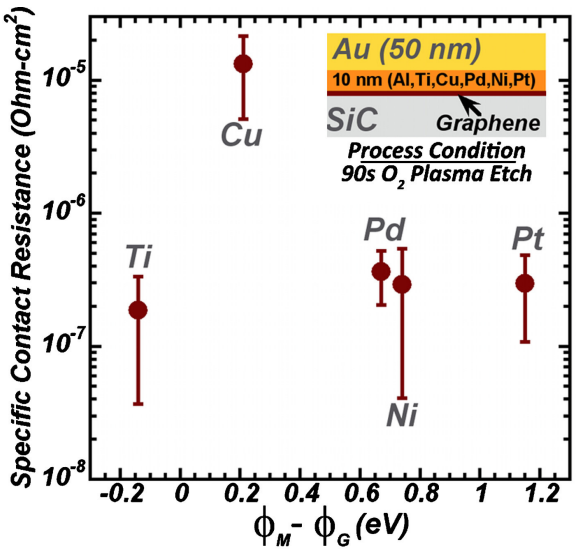

Figure 2.4: Contact resistances of different metals with epigraphene on SiC vs the work function difference between the metal layer and graphene measured by R., Joshua et al. [102]. Ti gives the lowest contact resistance, but Pd is mostly commonly used due to convenience. Even though there is a variation in the work function differences, the variance in contact resistances is small. Reprinted from [102], Copyright 2012 by American Institute of Physics

However, for very unidirectional systems, like atomic layer deposition of aluminum oxide, even the use of bilayer resists don't succeed enable the liftoff of thin oxide layers.

From the gating experiments (explained towards the end of this chapter) of graphene, it can be concluded that putting anything on graphene –other than the lattice matching insulating layers like hexagonal boron nitride (h-BN)– creates charge traps. Therefore, in order to avoid altering the nature of the electronic transport on graphene while measuring it, the development of the contact fabrication technology that minimizes the interaction is required. An understanding of the contact interference with the charge carriers can reveal the puzzling and hard to repeat results of graphene based devices.

When we want to isolate the SWGNR that contact pads are aligned to, from many other SWGNRs, additional alignment - lithography and etching steps are needed (Figure 2.3). A rectangular protective area over the ribbon needs to be defined and the rest needs to be etched so that the SWGNR can be isolated and the shorts can be removed from the system (Figure 2.2). This process introduces hardened resist residues (Figure 2.10(b) and

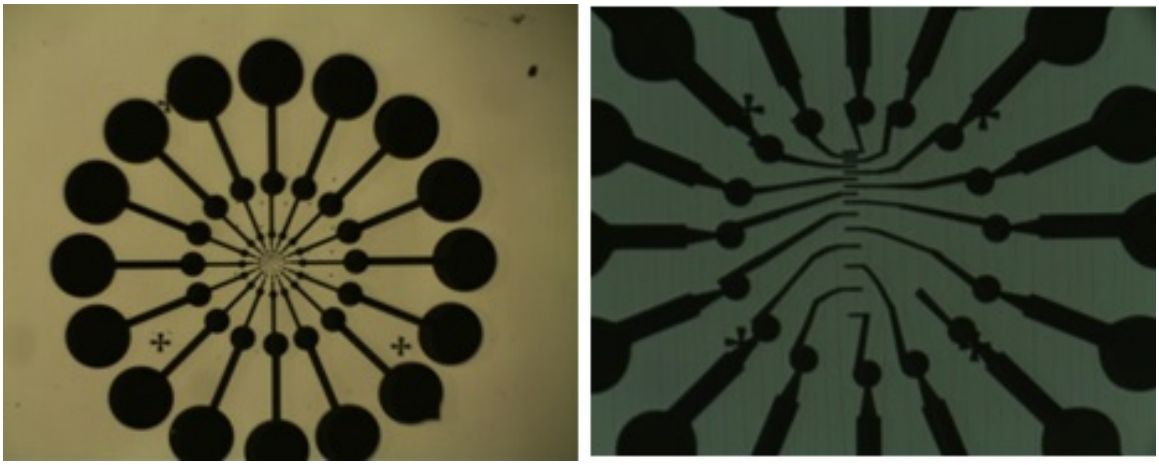

Figure 2.5: Pd/Au contacted SWGNRs produced with SEM lithography. Left: A zoomed in image of a contacted SWGNR where the large circular contacts are $50\ \mu m$ in diameter. Right: A Zoomed in picture where the large circular regions, visible on the corners are $15\ \mu m$ in diameter. This structure also shows how NPGS software works. Different magnification windows are used for different scales of lithography. This area is exposed to e-beam in three different windows. The circular regions are added to the design to compensate for the shifts while the SEM and the NPGS program switch between different magnifications. The shortest ribbon length is 200 nm. The lead that looks like it is missing a leg in the picture on the right (in the bottom right quarter of the picture) is designed that way so that it can be used as a gate lead if needed.

(c)) to the system after the RIE etching of excess graphene (4 SCCM O_2 gas flow at 16W RF power for 20 seconds). Removal of hardened resist residues requires a sonication step and the sonication can damage the gentle contacts that touch the 2D material. Therefore to avoid isolation, hardened resist residues and sonication a whole different approach has been developed.

First contacts can be put on graphene before the growth, so that the graphene won't be exposed to organic resists and resulting residues. Next the isolation step can be skipped by obtaining SWGNRs that are by default confined to the areas of interest and do not need etching of additional graphene regions. Once these two methods are accomplished, no processing is needed after graphene growth. We call this method "no post growth processing" approach (Figure 2.3), which means there is no processing once the graphene growth is completed. High temperature compatible amorphous carbon (aC) contacts can be used for this purpose.

2.2.4 Amorphous Carbon Contacts and the New Process Flow

This section presents where aC contacts and its fabrication are included in the process flow (Figure 2.3). The advantages of using aC contacts are also discussed.

aC can be deposited on the etched mesa sidewalls before any graphene growth. Once the graphene ribbon grows on the sidewall, it connects to the aC two pads that surround the step. However, this creates a system where 4 point probe measurement is not possible (Figure 2.6(a), since the nanoribbon underneath is not continuous). In order to enable the 4 point measurement, where contact resistances can be identified, a continuous SWGNR is needed under the contacts. If aC contacts can be placed on graphene with a patterning step, since aC contacts are high temperature compatible and they already need high temperature exposure to have low lead resistances, the whole system can be annealed above $1000\,^{\circ}C$ (Figure 2.6(b)). The resulting structure can host a SWGNR under the aC contacts, enabling a 4 point setup. The heat treatment step can significantly lower the residues by degassing

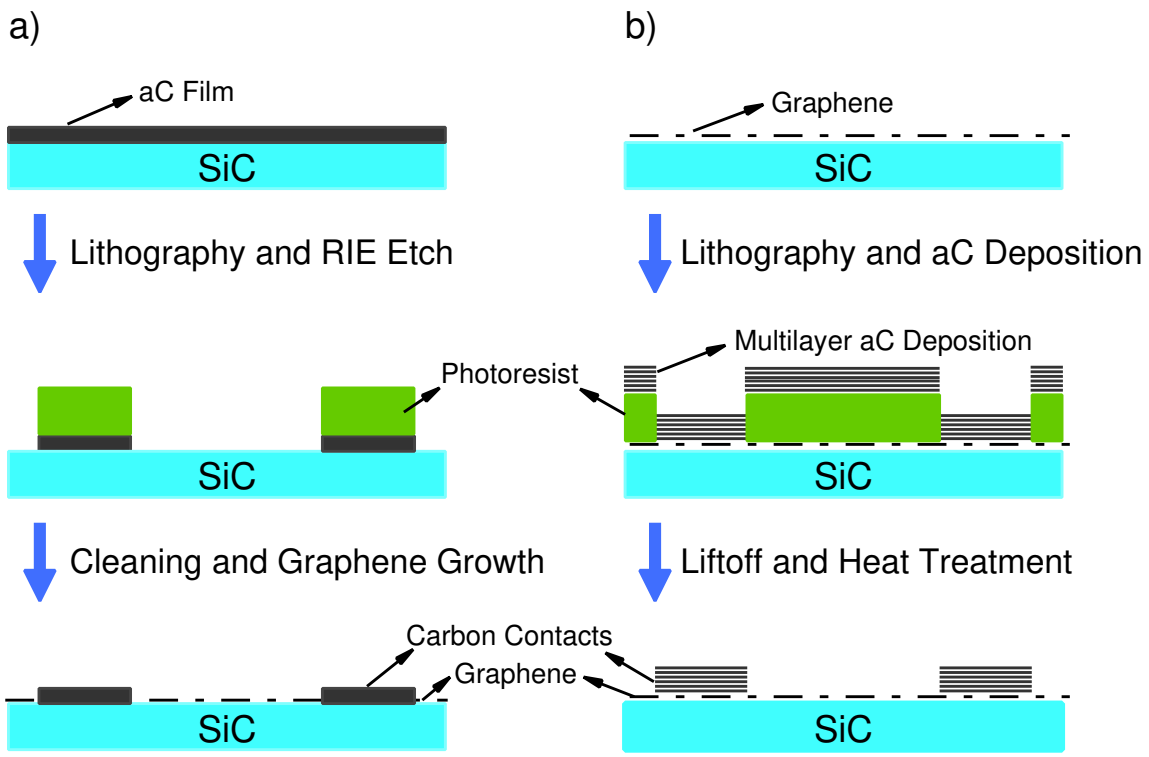

Figure 2.6: Amorphous carbon contact fabrication methods. a) The first method of amorphous carbon contact fabrication consists of depositing the film and then RIE etching the patterned shapes into contact pads. The final structure is high temperature compatible and it can survive through the epigraphene growth process. b) The liftoff process consists of depositing amorphous carbon films onto previously defined contacts areas. Liftoff is usually unsuccessful for a single pulse deposition of amorphous carbon, therefore multiple deposition of thin layers of aC are needed.

them. Islands of carbon clusters are expected after this process, but the impact of such particles is a lot less than the effect of resist residues that remain on the graphene surface after the acetone based wet cleaning/removal of organic resists.

Lifting off aC contacts from a previously patterned area is problematic due to aC failing to stick to the SiC surface. aC contacts don't liftoff like metal contacts. It doesn't stick to the surface unless it is deposited in a certain way. The aC deposition system 108CarbonA from Cressington Scientific Instruments uses two graphite rods (Figure 2.7). One with a sharpened pointing end and one with a flat end. The two rods are pushed onto each other with a spring mechanism. As the deposition goes on the spring pushes the rods together to

keep them in contact. Running 120 Amps current through this system causes carbon atom to sputter from the contact point and this can be deposited on a sample placed below the setup. For the case of SiC, when this deposition is done in a few cycles, aC does not stick to the surface (neither to SiC or graphene). Patterned resists hold the deposited carbon, but once the excess areas are cleaned with acetone, the developed regions don't have any aC remaining on them.

The liftoff problem blocked the realization of the setup shown in Figure 2.6 (b). Development of the aC liftoff method enabled having a continuous ribbon underneath the contacts and so a four point measurement. Experimenting with the deposition cycles showed us that using short and repetitive pulses of aC depositions over long periods creates aC layers that can survive the liftoff. The layered structure in Figure 2.6(b) refers to many layers of aC deposited on top of each other. For example a deposition that is 15-20 seconds long can give 20 nm thick aC. The same thickness can be achieved by depositing aC in shorter, 3 seconds long pulses. Getting the same thickness requires 20 to 30 pulses of depositions and in order to get the same sputtering rate for each pulse, 5 minute long waiting times are needed after a few cycles to let the rods cool down. After following this recipe till the desired thickness is reached, aC can be lifted off from the SiC surface. In the pulse method, when the rod doesn't cool down (not long enough breaks between pulses), deposited aC might burn the resist and not only fail the liftoff later, but it might also generate patches of irremovable aC and burnt resist areas.

Repeating the design used in Figure 2.5 for the aC case (Figure 2.8) it is seen that the same details for small ribbon lengths can be obtained for aC deposited contacts as well.

Many natural steps are visible in Figure 2.8 (Vertical lines). In fact there will be a third set of alignment mark that will be used for the the last isolation step (Figure 2.3). The reason why we have so many sets of alignment marks is that only metal alignment marks are visible under SEM and once we stop using metal on the surface, we need to have a combination of temporary and permanent marks to know where the ribbon is as shown

Figure 2.7: Left: The aC deposition system 108CarbonA from Cressington Scientific Instruments with its two graphite stick graphite stick setup. Rods are pushed towards each other with a spring mechanism. Right: The chamber with the power supply that can run more than 150 Amps through the graphite rods.

in the process flow chart in Figure 2.3. Unlike photolithography, a spin coated, exposed and developed sample can be used again in SEM lithography, enabling features developed on PMMA/MMA to be visible under SEM. Therefore, an alignment mark pattern can be developed first and then optical images can be taken. Once we know where these temporary alignment marks are with respect to the permanent ones, an alignment can be made to the ribbon.

SEM lithography enables the user to find the alignment marks in a given region. The size of alignment marks we use are on the order of $5\mu m$ and the window that we try to align at least two alignment marks is $50x50\mu m^2$. The smallest feature size is 200 nm and the maximum allowance for misalignment is on the order of a micron. The new alignment technique requires high magnification optical imaging and careful measurements.

The first set of alignment marks are etched (20 nm) into SiC to have a permanent reference. Then the natural sidewall ribbons (to be explained later) on the surface are checked with LFM and the locations of the good ones (20 nm tall and uninterrupted) are recorded. After coating with PMMA/MMA, another set of alignment marks are developed (on the resist - temporary) on the chip. The optical images are taken and the position of the ribbon with respect to the new alignment marks is recorded. When it comes to aligning the pattern with SEM lithography to the old geometry, this new location info is used. By adopting a

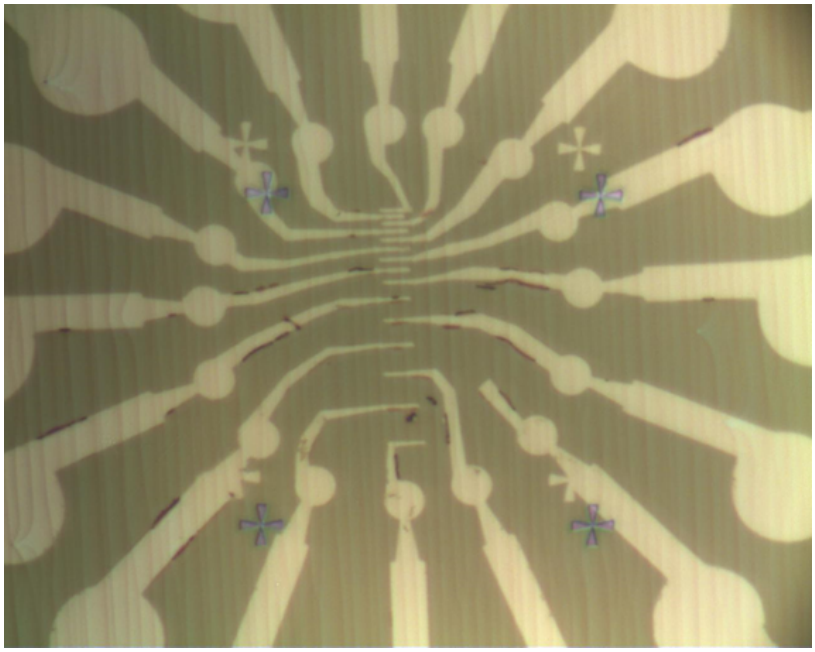

Figure 2.8: The same pad design as Figure 2.5, this time it is done with aC liftoff. Underlying natural steps contain SWGNRs along the step directions.

longer process flow, like the one shown in the first column of Figure 2.3, the use of metal alignment marks can be avoided.

aC sheet resistance increases upon cooling and can go up to $2.8k\Omega/\square$ at 4K from $1.8k\Omega/\square$ at room temperature as shown in Figure 2.9. This causes an increase in the total resistance of aC contacted nanoribbons at low temperatures (It will be presented later in the temperature dependent transport measurement section of the transport measurements section).

2.2.5 Cleaning and Annealing

Contacts built on graphene cause residues that come from the lithography steps and residues dope graphene. Conventional cleaning methods include acetone bath or 1165 (an oil based post etch resist remover by Micro Chem) bath. These wet cleaning methods [99, 101, 100] can clean the surface up to a point, but following AFM measurements show that some form of residues still exists on the surface.

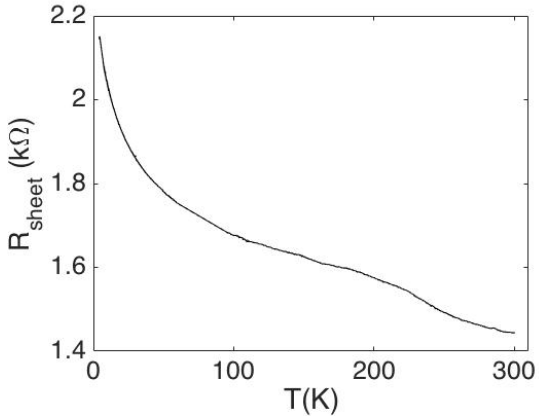

Figure 2.9: The sheet resistance of amorphous carbon annealed at $1500°C$ vs temperature from [103]. The sheet resistance increases upon cooling from $1.8k\Omega/\square$ at room temperature to $2.8k\Omega/\square$ at 4K.

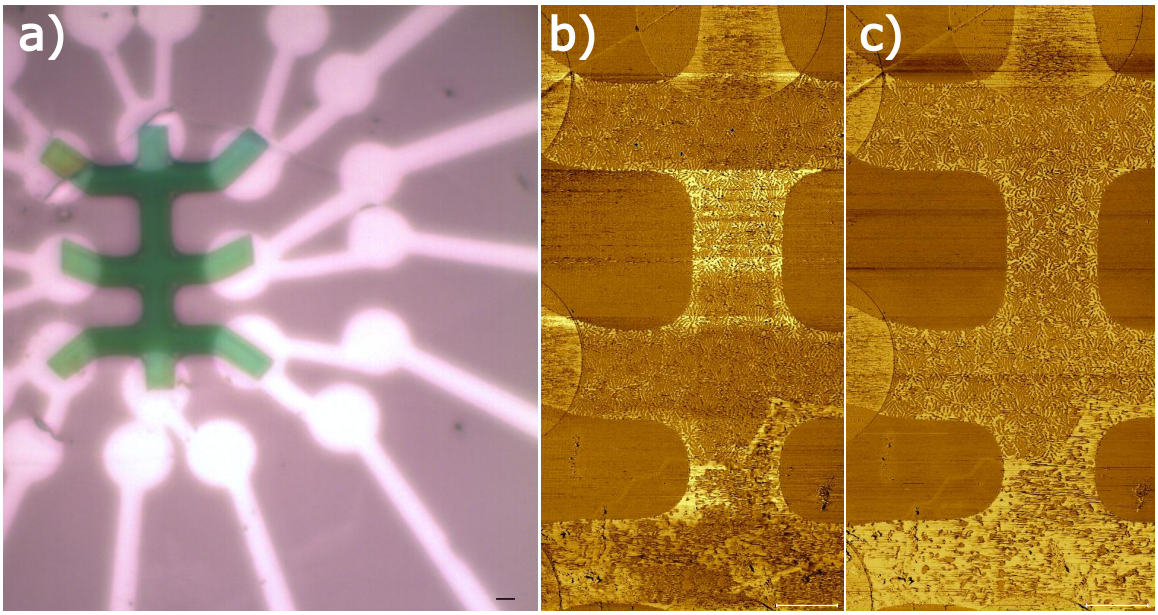

Figure 2.10: A graphene Hall bar with amorphous carbon contacts and the resist residues coming from fabrication steps. (a) An optical image showing the negative resist used for patterning. (b) LFM images of hardened-polymerized resist residues. After the dry etch and following wet cleaning, some parts of the polymerized resist do not wash away from the graphene surface. This leaves hardened residues on the surface (top half). The soft resist residue on the lower bottom half of the graphene Hall bar can be cleaned up to a point with a heat treatment as shown in (c). (c) The bar after the heat treatment ($1000°C$ for 20 minutes). The soft residue centers are shrunk but the hard residue patterns are still on the surface. The scale bars are $5\mu m$ long in all figures.

Electron mobility of monolayer graphene on Si face of SiC is on the order of $500cm^2/Vs$, giving mean free paths on the order of 100 nm to 500 nm [39] for a charge density on the order of $10^{12}cm^{-2}$. Cleaning (with the heat treatment) the patterned graphene can raise the mobility value up to $600cm^2/Vs$, an overall 20% increase for graphene samples with polymerized resist residues (Figure 2.10).

Other cleaning methods in the literature include UV ozone treatment [104], acetic acid bath [105], thermal annealing [106] under Ar atmosphere and vacuum annealing [107]. Comparing all these methods through measurements of Raman spectroscopy before and after the treatment, along with resistivity measurements and mobility and charge density measurements for Hall bar shaped planar graphene setups, we obtained an order in terms of what cleaning method works the best. A different order can be made from literature, which might be due to some of the literature experiments being done on exfoliated graphene, which is by default not a clean environment. In our investigation, the heat treatment method (heating of aC contacted graphene up to $1000^{\circ}C$ in a closed crucible) worked best for epigraphene on SiC.

Etching graphene especially with MAN (ma-N negative tone photoresist by Micro Resists Technology) based resists causes hard to remove resist residues. A heat treatment can clean soft residues on such samples, but polymerized residues can still remain in the shape they obtained after dry etching. Figure 2.10 shows a Hall bar made with aC contacts. aC contacts are deposited on a monolayer sample first and then the Hall bar pattern is etched with MAN resist (Figure 2.10 (a)). Figure 2.10 (b) shows the region right after the etching. There are two types of residues, the soft (bottom half) and the hard-polymerized residue (the top half). Part (c) of the same figure shows what happens after the heat treatment ($1000^{\circ}C$ for 20 minutes). The soft residue can be cleaned to a point but the hard parts survive through the treatment. Unless sonicated (before the ehat treatment) such residues exist on graphene after dry etching. Therefore, either dry etching on graphene should be avoided, or methods that allow sonication need to be developed.

Overall, samples with "no post growth processing" (Figure 2.3) approach give the cleanest graphene surfaces. Etching with organic resists should be avoided. The exposure to air can still cause an increase in the overall resistance (Figure 2.1) even for samples that are produced with clean processing methods (Figure 2.6 (b)) and that have gone through heat treatments. Therefore, another heat treatment right before a transport measurement is necessary. A vacuum probe station is built for this purpose which is explained in the next section.

2.3 Handling and the Measurement Techniques

Since samples give much higher resistance profiles (about twice the resistance) in air (Figure 2.1) or after they are exposed to air, a degassing phase is needed before a transport measurement. A vacuum annealing probe station system is built for this purpose (Figure 2.11).

The vacuum chamber can be pumped down to $10^{-6}mbar$. This helps sample to degas and helps lowering the resistance. The copper piece that the sample sits on contains a heater underneath that can heat the piece up to $400°C$ and micro-manipulators can reach over the samples with 50 nm lateral motion precision and the attached probes can be lowered onto the contacts for transport measurements.

This enables us to make measurements while graphene is clean. Further measurements done in this chamber are given in the Experimental Measurements chapter. Details of the setup and the details of the software used to control the micro-manipulators are given in appendix.

2.3.1 Gating

A gate oxide layer and a gate metal on top of the oxide can only be considered for graphene if the graphene is already covered with a lattice matching insulating layer (h-BN). Otherwise the roughness that comes from the oxide layer creates charge traps. These traps show

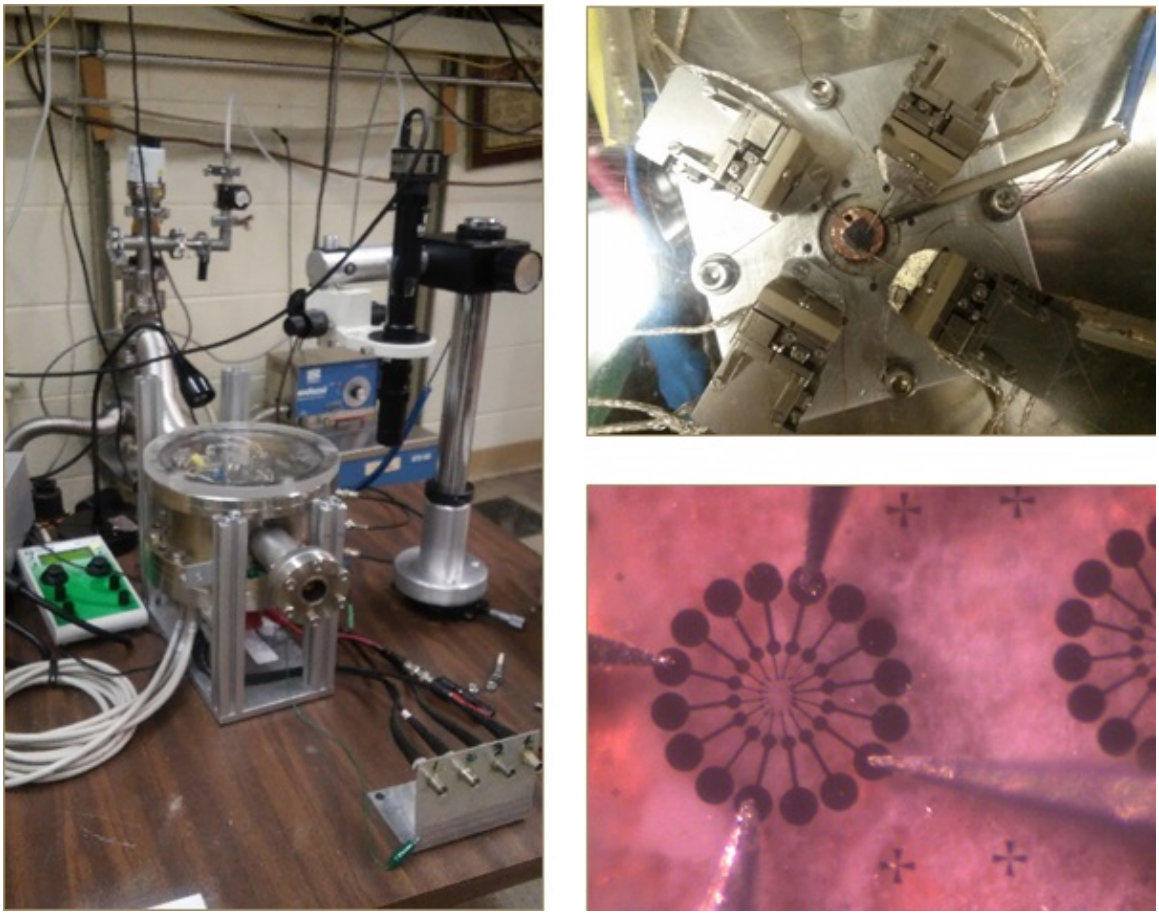

Figure 2.11: Vacuum probe station setup. Left: The chamber with four bnc connections to four probes and the camera to observe the micro-manipulators. The chamber has a plexiglass lid that enables the camera to focus on the chip underneath. Right: The top figure shows the configuration of the micro-manipulators. Each manipulator has a tip attached on them which can be used as probes. Bottom figure shows the measurements done with four probes. The largest circle on the contact design is $50\mu m$ in diameter.

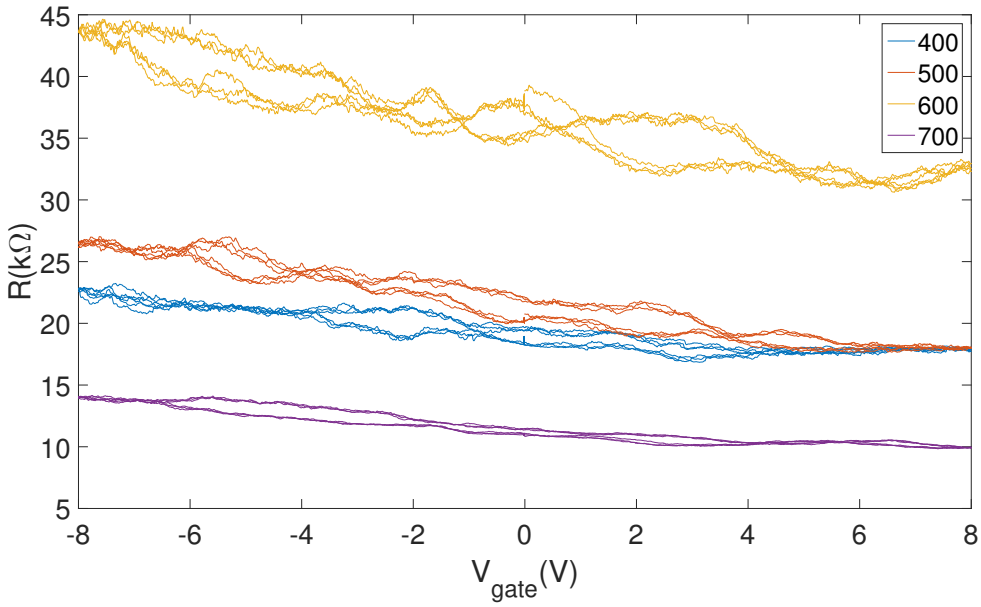

Figure 2.12: Gate voltage vs resistance measurements of a SWGNR with lengths ranging from 400 nm to 700 nm. The hysteresis loops indicate charge traps under the gate oxide. Also there is no visible charge neutrality center which normally shows up as a resistance peak.

up as hysteresis loops (most of the time, not always) over resistance vs applied gate voltage measurements. Also it is challenging to gate the nanoribbon to the charge neutrality point if the graphene is heavily doped by the oxide layer.

The hysteresis loops of a gated ribbon that has multiple lengths (from 400 nm to 700 nm) are given in Figure 2.12. 100 nA constant current is applied through all ribbons while voltage measurements are taken in a four point setup.

The geometry of a gated nanoribbon can be seen in Figure 2.13. The gate oxide is obtained by first depositing a seed layer Al on the whole chip surface with Physical Vapor Deposition (PVD) technique (2 nm, which is enough to fully self oxidize). This step is necessary because Atomic Layer Deposited (ALD) oxide doesn't wet the graphene surface. After the seed layer 20-25 nm of Al_2O_3 is deposited by an ALD system. While the oxide covers the whole surface, gate metal is deposited on top (30 nm Au) after the pattering is done lithographically.

2.3.2 Cooling

A CryoIndustry cryocooler has been used for low temperature measurements. The setup has the ability to go from 420 K to 4.2 K and it can sweep magnetic fields up to 9T.

The normal minimum cryocooler temperature 4.2 K, can further be brought down with a continuous He flowing technique through the space that surrounds the sample region. The condensed He that is supplied to the surround space through micro tubes can be pumped out of at a slow rate, while the flow rate through the micro tubes are adjusted accordingly. The two parameters that can stabilize this system are the He flow and the pumping rate. These two variables can be varied till a stable low temperature value is obtained. Stable temperatures below 1.6 K can be achieved with this method. Targeting a certain value for the lowest temperature is not always possible since the minimum of the system varies.

2.3.3 Packaging-Coating of Graphene with h-BN

As mentioned, graphene is susceptible to any exposure and any deposition. The ideal graphene fabrication would consists of covering graphene with an insulating layer, that doesn't interact with the surface, right after the growth. h-BN is a good candidate for this purpose. It is an insulating material and it has a matching lattice with graphene. This feature minimizes the interaction and helps graphene preserve its electrical properties.

Hetero-structures [108] –that contain h-BN coated graphene– have led to the observation of unique electronic features like Hofstadter's Butterfly [109]. Observations of this kind restates the importance of preserving the graphene crystal pristine and preventing the exposure to residues and contamination before, during and after the fabrication.

Lateral growth of h-BN on epigraphene on SiC has recently been established [110] and the extension of this new technology to SWGNRs can improve the next generation transport measurements.

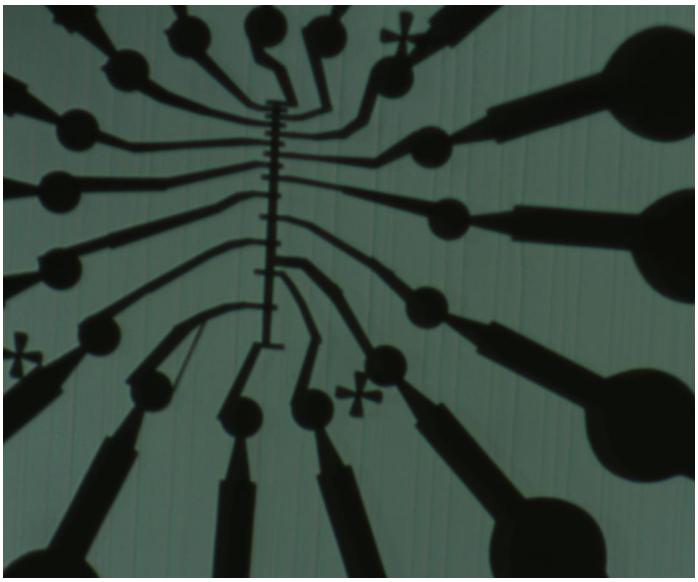

Figure 2.13: The final SWGNR device with the gate over an isolated natural step nanoribbon. The gate connection is the thick lead on the right. The same lead can be seen unconnected in a previous geometry given in Figure 2.2.

CHAPTER 3
EPITAXIAL GRAPHENE GROWTH

Nanofabrication can be split into two sections for the case of graphene: the first is crystal growth and the second is fabrication. In a reverse order, the fabrication steps are given in the previous chapter since the epigraphene growth needs a longer discussion.

For the case of SWGNRs some pre-growth steps are needed to satisfy the selective growth conditions that makes SWGNRs confined to certain areas. Therefore, SWGNR growth will be explained by first starting with the epigraphene growth itself, then the parameters that affect the growth process will be listed and the methods developed to overcome resulting problems will be introduced.

The approach of varying each parameter during a process not only costs time, but also not always possible since the change in some parameters are undetectable during the process or over time as the setups are used. Therefore, during the course of this study, the main approach has been to lower the number of variables by developing methods where we can avoid inconsistencies. Epigraphene nanoribbon growth techniques are investigated in this sense and the growth methods are summarized in the following sections of this chapter.

3.1 Graphene Growth

Graphene is a 2D crystal. It is not a polymer, therefore *growth* rather than *syntheses* is the terminology of choice. In a similar manner to any other crystal that needs to be integrated into a device, either to study the electronic transport properties or for industrial fabrication purposes, the crystal needs to be grown on the measurement substrate. Transfer of graphene to another substrate, conventionally, is not an industrially scalable method due to the high probability of interface defects, lattice mismatching, non-reproducibility, crystal defects and imperfections. In literature there are mainly three graphene production

methods: exfoliation, chemical vapor deposition (CVD) and epitaxial growth.

Exfoliation simply consists in peeling a layer of graphite by using tape. Even though it offers a quick way to obtain graphene layers, compared to other methods, it lacks the standards in terms of scalability.

Chemical vapor deposition (CVD) is the method where graphene is grown on Cu (or other metal substrates) at elevated temperatures. Large graphene flakes up to $1mm^2$ can be obtained using this method, therefore it is highly scalable. However, utilizing this graphene requires transferring the material from Cu to an insulating surface, unless it is to be used on Cu.

Epigraphene on SiC is the method where graphene is obtained by thermal decomposition of SiC. Once the Si is sublimated from SiC surface, the leftover C forms the graphene on an insulating substrate and it doesn't need transfer.

Among the existing production methods, epigraphene on SiC is the only scalable one that doesn't need to be transferred to an insulating substrate. Epigraphene also enables the scalable production of SWGNRs [67] which show ballistic transport [84].

3.2 Epitaxial Graphene Growth Mechanism

Production of epigraphene on SiC starts with the selection of commercially available SiC wafers that are cut from single crystal boules. SiC has many crystal structures, with different polytypes as shown in Figure 3.1. During this study wafers cut from 4H and 6H SiC crystals are used.

In past years the quality of surface polishing of commercially available SiC wafers was not high enough to perform epigraphene growth and an additional hydrogen etching step was necessary for surface planarization. Today, chemical and mechanical polishing (CMP) of SiC wafers give low enough roughness such that hydrogen etching can be avoided. It is also shown that hydrogen etching can cause an increase in the overall resistance of graphene layers [111].

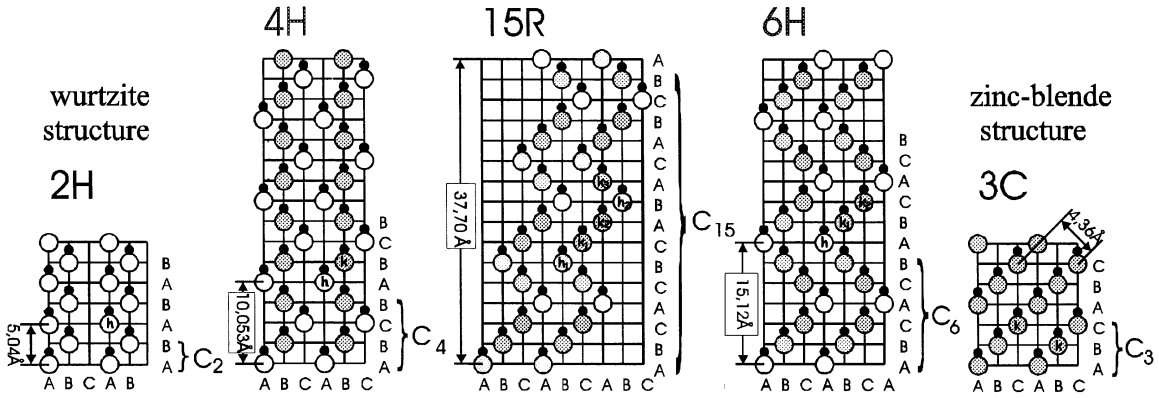

Figure 3.1: Different stackings of SiC crystals. Only 4H and 6H SiC are used for epigraphene growth. Reprinted from [113], Copyright 2002 by IEEE.

CMP polished wafers have flat surfaces. However, even wafers cut on-axis have small miscut angles. Once the sample is exposed to epigraphene growth temperatures, that is on the order of $1500°C$, these natural steps start moving on the surface and bunch into each other [112]. These steps prevent the morphological confinement of the ribbon, which will be explained in detail later in this chapter (Figure 3.12). In order to prevent the step bunching from happening during the graphene growth, an additional annealing step can be used.

The first step in epigraphene growth is the selection of the chip dimensions. For all the samples in this thesis SiC wafers are cut to 3x4mm^2 SiC chips. Then small chips are sonicated in IPA and acetone respectively for 20 minutes to remove any residues. For planar graphene, no further processing is needed on SiC before the epitaxial growth process.

Graphene can be obtained on SiC with a controlled thermal decomposition mechanism. By utilizing a confinement with a leak hole, controlled sublimation of silicon carbide has been established in the confinement controlled sublimation (CCS) method [114]. The details of the setup are given in Figure 3.3.

In the CCS process a graphite crucible with a leak hole is heated by induction while the SiC chip sits inside. As the temperature rises, Si starts sublimating from the SiC surface and from previously Si saturated inner walls of the crucible. Having the crucible in high vacuum

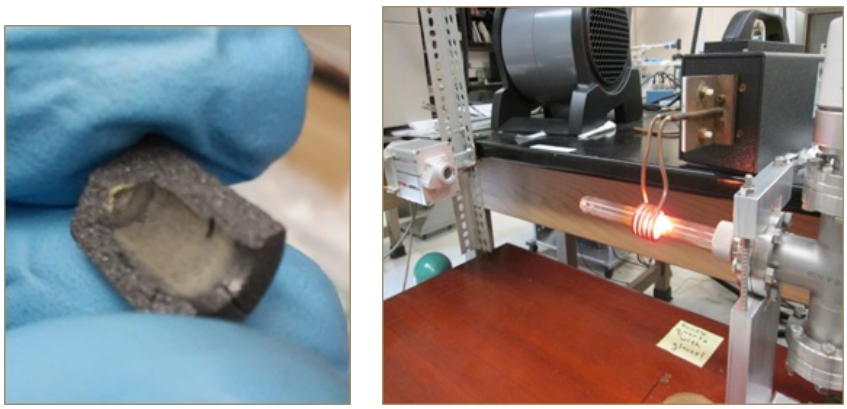

Figure 3.2: Left: A broken graphite crucible showing Si saturated inner walls. Si accumulated on the inner walls of the crucible can be the dominating factor that inhibits graphene growth during the CCS process. Right: Induction furnace is heating up a crucible. The temperature of the crucible is recorded by an optical pyrometer on the left. This laser pyrometer can read through the quartz glass tube. this reading is then used by a feedback program to set the RF power of the induction heater.

($\approx 10^{-6} mbar$) during the heating results in escaping of Si vapor through the leak hole. This partial pressure difference can be finely tuned to the point where the Si sublimation is small enough to remove Si only from the first few layers of the SiC. The left over carbon on the SiC surface forms graphene with high structural quality. Si face(0001) of SiC can host few layers of graphene while C face$(000\bar{1})$ can host many layers. This happens due to different Si sublimation rates from these surfaces. The crucible geometry (inner volume, leak hole size, inner surface area), Si saturation of the crucible, the selected SiC wafer, pressure outside the crucible and the growth recipe (temperature steps and the duration) are all factors that can be optimized to obtain few layers of graphene on the surface.

Even though the CCS process looks like a conventional gas flow through a constriction type of fluid dynamics problem, temperatures as high as $1500°C$ and high pressure differences between inner and outer parts of the crucible and short growth times prevent us coming up with a simple model for the process.

Figure 3.3 shows the CCS setup. Once a certain temperature is reached (depends on the external pressure, but $1400°C$ can be considered for our setup), Si starts evaporating from the inner crucible walls. If we consider that there is not a leak hole and no SiC chip inside;

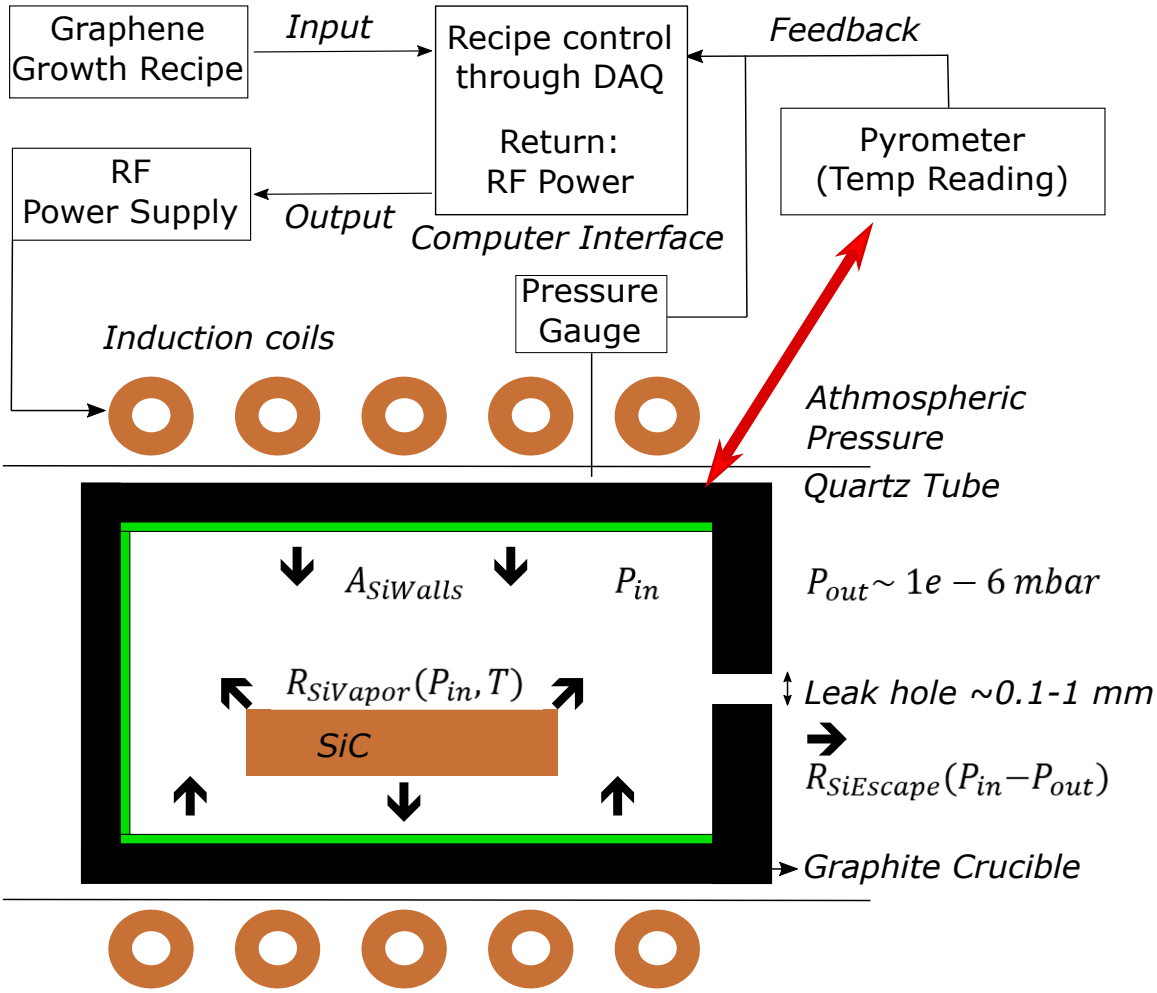

Figure 3.3: A schematic of the Confinement Controlled Sublimation of SiC method. This figure elaborates the setup shown in Figure 3.2. The feedback mechanism reads the temperature and the pressure, then it adjusts the RF power with respect to the temperature reading. The pressure reading is just to make sure that the starting pressure is reached. $A_{SiWalls}$ is the Si pressure coming from the crucible walls. P_{in} and P_{out} are the inner and outer pressures. The rate variables represent the Si sublimation rate from the SiC surface and the Si leak through the hole. The variables are explained in detail in appendix.

the Si pressure degassing from the walls is expected to reach a temperature dependent constant value and unless the temperature is changed, it should remain constant ($A_{SiWalls}$).

For the case of a leak hole and having a SiC chip in the crucible, Si pressure from the walls is still assumed to be constant. However, it is observed that a crucible stops growing graphene if it is used a few times in a row without being unsaturated (Heated empty so that the excess Si can escape the crucible). This means that the Si on the inner walls of the crucible builds up over time, indicating that the Si sublimating from the chip is in fact, more than the escaping Si. This effect shows up over long periods of time, therefore for the simplicity of modeling a single growth event, the Si build up on the walls is ignored. The Si escape rate ($R_{SiEscape}$) and the Si sublimation rate ($R_{SiVapor}$) are assumed to be the equal.

The amount of Si sublimated from the SiC surfaces during a monolayer growth on Si-face (0001) (Figure 3.4) can be estimated. By knowing the mass leaving the system over a certain time period, the average flow rate can be calculated. Details of the variables involved in the CCS process along with a simple model to obtain the flow rate are given in appendix.

Modelling the growth and pinpointing a recipe for monolayer graphene with uniform coverage is also challenging due to the initial conditions of the SiC chip playing a substantial role in the final graphene amount on the surface. For monolayer samples, SiC crystal imperfections and surface roughness can lead to defected graphene. Upon choosing an incomplete characterization scheme, these low quality features of graphene might go unnoticed. For example, Raman spectroscopy can be used to analyze the number of layers of graphene grown on the C-face $(000\bar{1})$ (Figure 3.4). The D peak (1350) can tell about the structural quality of the crystal and comparison of the 2D (2700) peak to the G (1550) peak can indicate the number of layers. Two similar Raman profiles can be obtained for monolayer looking like samples but a following surface spectroscopy might reveal significant differences between surface morphologies. Therefore, it is important to pick the right

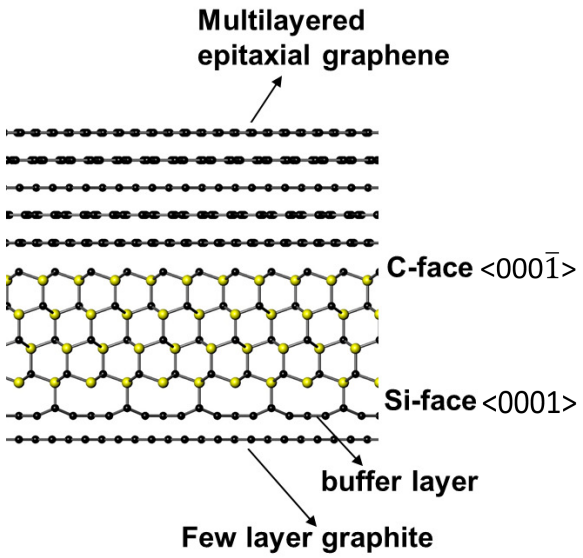

Figure 3.4: The C-face $(000\bar{1})$ and the Si-face (0001) of SiC and the graphene growth dynamics on them. Few layers of graphene grows on the Si-face while many grows on the C-face. The first graphene layer on the Si-face, that is is pinned to the SiC, is called the buffer layer.

characterization method for the experimental purpose.

3.2.1 Epitaxial Sidewall Graphene Nanoribbons

Si sublimation is not uniform across the SiC surface. As the SiC is heated up, the sublimation starts earlier on certain facets. Upon pre-templating the surface, such facets can be introduced into the SiC before the graphene growth. Once the graphene growth recipe is finely tuned and the growth process is stopped before the graphene extends to other facets, graphene formations confined to the templated facets can be obtained. Conventionally [67] 20 nm mesas or trenches can be etched on SiC surface using RIE to fabricate SWGNRs (conventional SWGNRs). Once these structures are heated, sublimation occurs on the sidewalls before it does on the (0001) (Si-face) planar face of 4H SiC. This feature can be used to obtain selectively grown graphene ribbons along the sidewalls of predefined steps. SWGNRs with specific orientations (Figure 3.5) at various lengths can be fabricated this way.

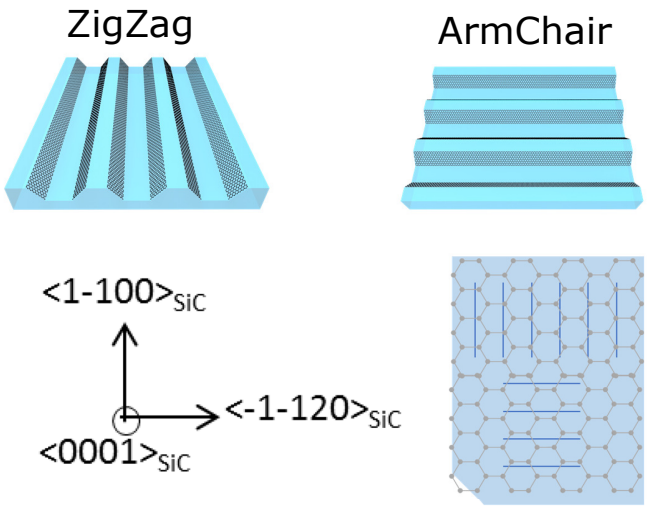

Figure 3.5: Zig-Zag and Armchair epigraphene nanoribbon structures on SiC. ZZ and AC graphene edge terminations of can be obtained by pre-etching the SiC crystal in $(1\bar{1}00)$ and $(\bar{1}\bar{1}20)$ directions.

With epigraphene, the stacking of few graphene layers varies depending on the face (Figure 3.4) [115, 116, 117]. On Si face (0001) of SiC, multilayer graphene has Bernal stacking [21]. SWGNRs on the other hand can made to be monolayer [118] as it can be seen from cross sectional TEM images in Figure 3.6.

TEM images in Figure 3.6 show that a monolayer graphene freely stands on the sidewall which has nearly a 27° angle. Towards the top and bottom of the sidewall, mini step formations start and the SWGNR merges into the buffer layer that sits on the plateaus. Buffer layer is pinned to the SiC crystal (Figure 3.4) and compared to graphene, it has very high electrical resistance. Therefore, the conduction is dominated by the SWGNR part if any current was to be sent along the ribbon.

The amount of graphene that can be obtained on SiC after the growth process heavily depends on the initial conditions. Initial conditions of the experimental setup only consists of the crucible condition. As the crucible is used repeatedly, we have observed that the amount of graphene grown reduces. This was related to a Si saturation of the crucible that prevents additional Si sublimation from the SiC surface. In order to prevent that, the crucible can be baked without a SiC chip inside before any growth attempt. Baking the

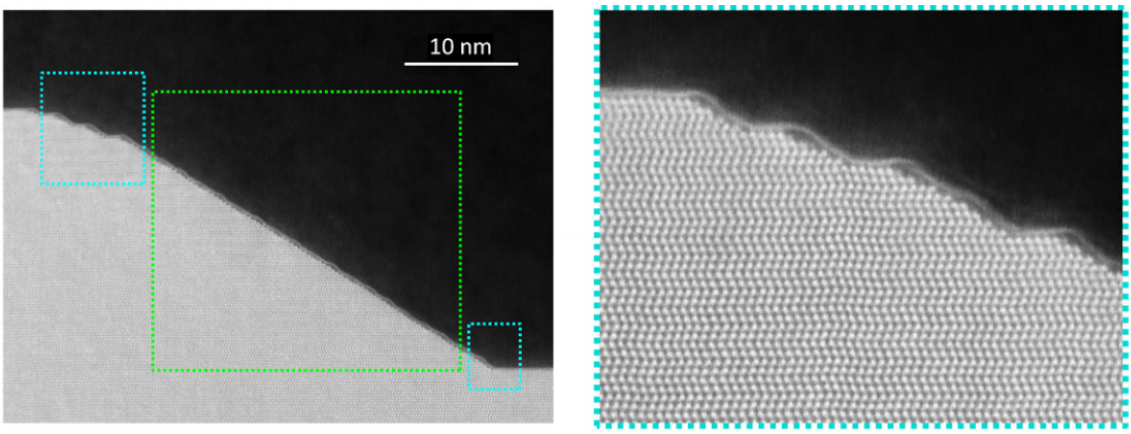

Figure 3.6: A TEM image of a SWGNR[119]. SiC atoms can be seen with atomic precision while monolayer graphene on top stands freely. Graphene is pinned to the SiC crystal over the plateau. This pinned section of graphene is called the buffer layer. Reprinted from [119], Copyright 2016 by IOP Publishing.

crucible above the regular graphene growth temperatures for a long time (if the graphene growth recipe is $1450°C$ for 10 minutes, then the empty bake recipe can be chosen as $1500°C$ for 2 hours) results in Si unsaturated crucible walls. The next chip that is grown with a regular recipe inside that crucible ends up growing a greater amount of graphene on it, since the crucible walls were unsaturated and Si sublimation from SiC became easy. Samples with such extra graphene coverage are called overgrown samples. Only after a sacrificial sample is grown with a regular recipe, the crucible walls have the right amount of Si saturation and an actual SWGNR growth can take place. The second growth after the empty baking of the crucible gives the best chance to obtain a consistent growth environment for SWGNRs. Si pressure inside the crucible is not high or low to create undergrown or overgrown samples.

A second parameter is the initial conditions of the SiC crystal surface. Miscut angles changes locally on a wafer and causes random different densities of natural steps on the surface. These natural steps can become the nucleation centers of unwanted graphene growth around the patterned, targeted graphene areas (SWGNRs).

Graphene growth on SiC has been modelled in various ways [120, 121, 122] and models have been proposed SWGNR growth on non-planar facets [123]. Graphene growth is hard

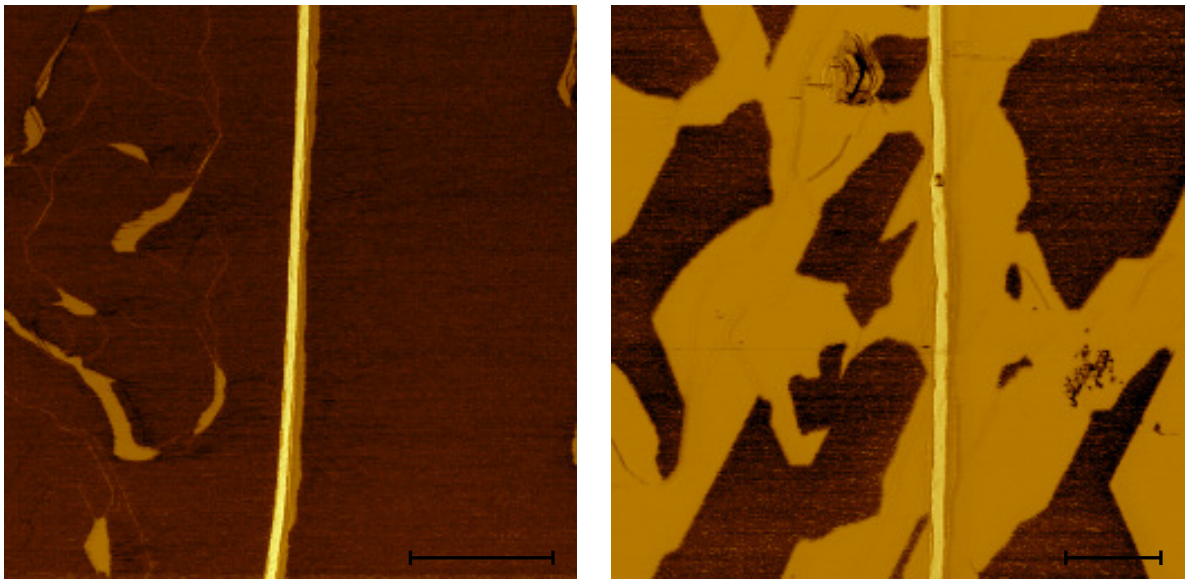

Figure 3.7: Lateral force images of grown ribbons, The stripe in the middle is a 20 nm step on which we aim to confine the SWGNR growth. Lighter areas correspond to low friction graphene regions. Left: Lateral force image of a slightly overgrown ribbon. Right: A heavily overgrown ribbon. The right sample is grown right after an empty bake of a crucible, the result is an overgrown sample. The sample on the left is grown with the same recipe right after the sample on the right. Since the crucible is saturated during the first growth, the overall Si sublimation is lower in the second growth due to elevated inner Si vapor pressure. The final graphene coverage is significantly less than the first growth attempt. The scale bar is 500 nm long in both pictures.

to model because two factors that trigger each other are activated simultaneously during the growth. The first one is the Si sublimation and the second one is the step flow [112]. Especially the change in volume calculation is complicated in a modelling of the growth of SWGNRs. Since the 20 nm tall steps are likely to move at graphene growth temperatures, one needs to consider the change in volume in terms of the distance steps move and the angle change sidewalls are experiencing. In order to simplify the problem and analyze the growth through the change in the volume of SiC, let us consider only steepening. As it will be shown later, it is possible to reduce step flow through addition of an annealing step that stabilize the step before the epigraphene growth.

In order to obtain monolayer graphene one needs to sublimate Si from the top three layers of SiC [124]. Therefore, for the case of sidewalls, if one knows the initial angle, the step height, the final angle, then the volume change in SiC can be calculated. This volume can then be assumed to be a slab of SiC with the final width and length of the SWGNR. If monolayer graphene is desired then the corresponding change in volume can be calculated. If the step remains at the same position and only faceting is considered then the change in volume can be written as:

$$V = L\frac{h^2(Cot(\Theta) - Cot(27^\circ))}{2}, \tag{3.1}$$

where 27° is the angle of the stable SiC facets ($(1\bar{1}0n)$ with n=7 for AC and $(\bar{1}\bar{1}2n)$ for ZZ with n=12) which is defined crystallographically [125, 126].

For a slab of SiC that has dimensions of X (height), L (length) and h/(Cos(Θ)) (width, taken same as the ribbon width), the volume is:

$$V = X \times L \times h/(Sin(27^\circ)), \tag{3.2}$$

the condition that gives the monolayer graphene requires exactly three layer of SiC to be thermally decomposed. This gives a height of 0.75 nm. Using this value instead of X and

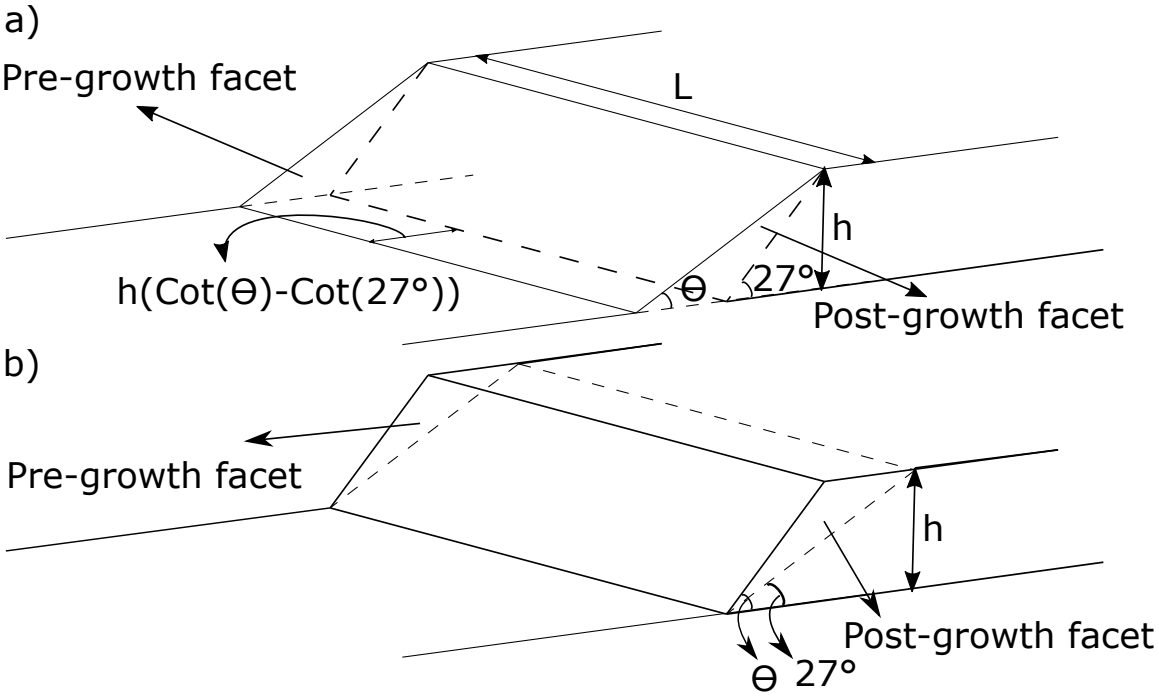

Figure 3.8: A simple growth model that ignores all step flow parameters. Just by looking at the change in the angle of the facet, one can identify how much SiC needs to be thermally decompose for monolayer graphene. a) The change in the facet angle if the initial facet is shallower than 27°, b) steeper than 27°. The fixed reference point is considered to be at the top for a) and at the bottom for b).

combining two equations give:

$$\frac{X}{(Sin(27^\circ))} = \frac{h(Cot(\Theta) - Cot(27^\circ))}{2}, \tag{3.3}$$

$$15 = h(Cot(\Theta)Sin(27^\circ) - Cot(27^\circ)Sin(27^\circ)), \tag{3.4}$$

$$15 = h(Cot(\Theta)Sin(27^\circ) - Cos(27^\circ)). \tag{3.5}$$

Parametrizing such an equation to the step height and to the initial step angle, and assuming that the final facet angle is 27° and the steps height remains the same, two resulting equations can be obtained. The first one is for the initial step angles that are less than 27°

and the second equation is for the ones that are steeper than 27°.

$$15 + hCos[(27\Pi)/180] = hCot[\theta\Pi/180]Sin[(27\Pi)/180], \tag{3.6}$$

$$15 - hCos[(27\Pi)/180] = -hCot[\theta\Pi/180]Sin[(27\Pi)/180], \tag{3.7}$$

where h is the initial height and θ is the initial step angle.

This calculation shows that in order to have a 27° facet, which is experimentally observed to be the stable facet for SWGNRs, One needs to start with the initial sidewall angles of either 16° or 37°. Anything in between these angles will not give the needed amount of carbon to form a monolayer graphene on the sidewall. Anything outside this angle interval will give too much carbon and will result in overgrown SWGNRs. A method to control the initial angle will be introduced later in this chapter (Figure 3.18).

The graphene on overgrown SWGNRs first start expanding on the top edge of the step. This becomes more complicated when we also consider the buffer layer that is necessary to obtain monolayer graphene on the Si face of SiC. This means twice the carbon material is needed to form a free standing monolayer graphene on the Si face. Models explaining the non-planar graphene (SWGNR) growth by retraction of a step assumes the carbon material that emerges at a spot is static and doesn't move on the sidewall or on the surface [123]. The carbon is assumed to form graphene on the spot that it is first freed from Si. However, by simply looking at the amount of carbon that comes from faceting after epigraphene growth it can be concluded that a mobile carbon approach is necessary to model the growth. But also the nucleation point of graphene growth on plateaus has always been a topographical indentation or a bump [127], then layer by layer growth has been observed from these nucleation points. Therefore, it can be said that a combined approach that considers the step motion triggered growth along with mobile carbon atoms needs to be put into the same equation to model the graphene growth.

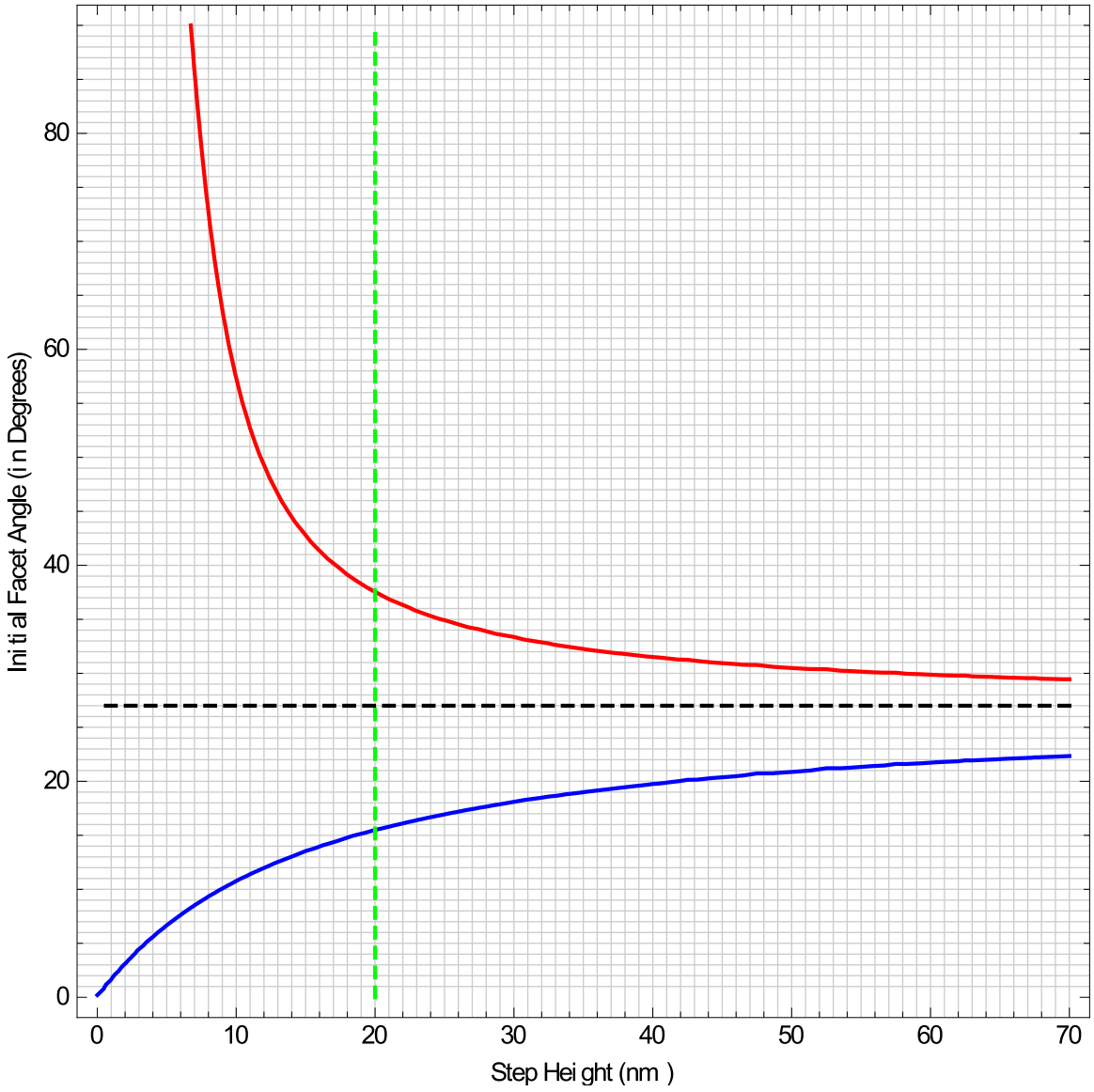

Figure 3.9: Required initial boundary conditions to obtain monolayer graphene on a sidewall. Black and green dashed lines indicate the common final conditions (20 nm tall facets with 27°). Red and blue lines are equation 3.4 and equation 3.5 respectively. By moving the black and green lines, one can find the required initial conditions to obtain monolayer graphene the on the 27° facet. Current lines show that an initially 20 nm tall step should be angled at either 16° or 37° (from equations 3.4 and 3.5) in order to turn into a 27° facet with monolayer graphene on it.

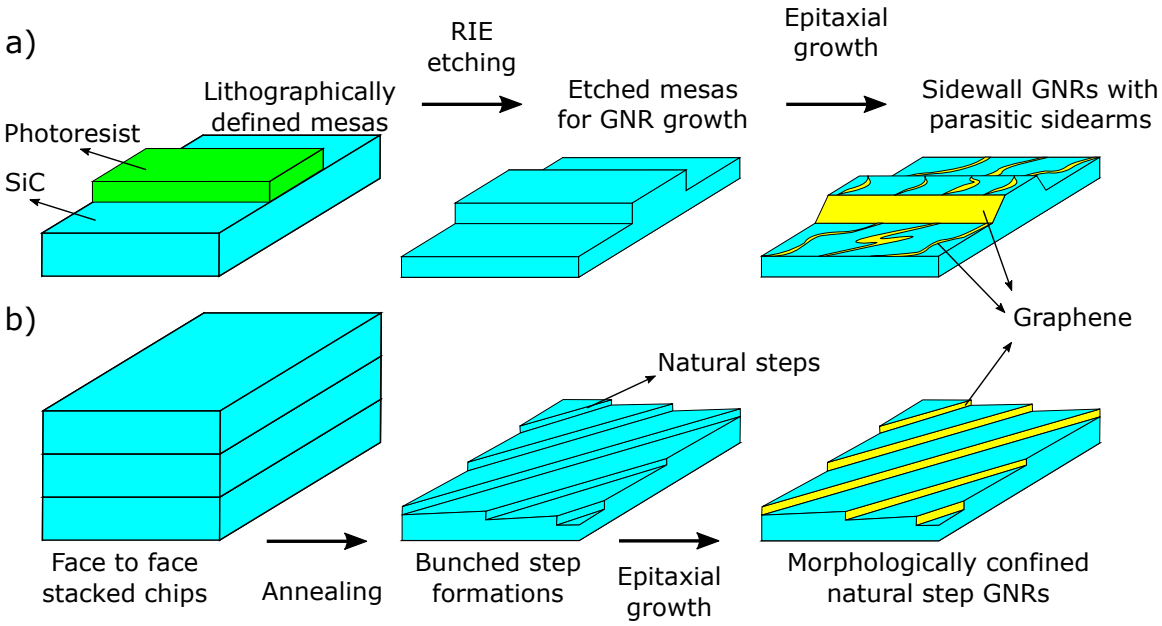

Figure 3.10: a) A conventional SWGNR production scheme which results in parasitic sidearm graphene attachments. b) The Natural step GNR fabrication method. First, chips are annealed face to face to elevate step bunching, then these samples are used for GNR growth. Confined GNRs on natural steps of the SiC can be obtained using this method.

3.2.2 Step Flow and Step Bunching on SiC

Each SiC wafer is cut from a single crystal boule, however even wafers cut on axis, can have a certain miscut angle. The final surface morphology can be tuned by selecting the correct growth regime for the sample. For example similar quality graphene can be obtained by applying a short exposure to high temperatures or a longer exposure to lower temperatures. The trade off between these growth recipes is the step flow of SiC that increases as the graphene growth temperatures are increased.

Small SiC steps that are not visible during an atomic force microscopy (AFM) scan, can bunch into each other during graphene growth and form taller structures. If the natural steps align parallel, or close to the parallel to the etched step, then they can merge to the main step, forming sidearms (Figure 3.10(a)). If the natural steps are perpendicular to the SWGNR, the step flow can even disconnect the sidewall (Figure 3.11). A LFM image of sidearms can be seen in Figure 3.12. The density of these sidearms depends on the miscut

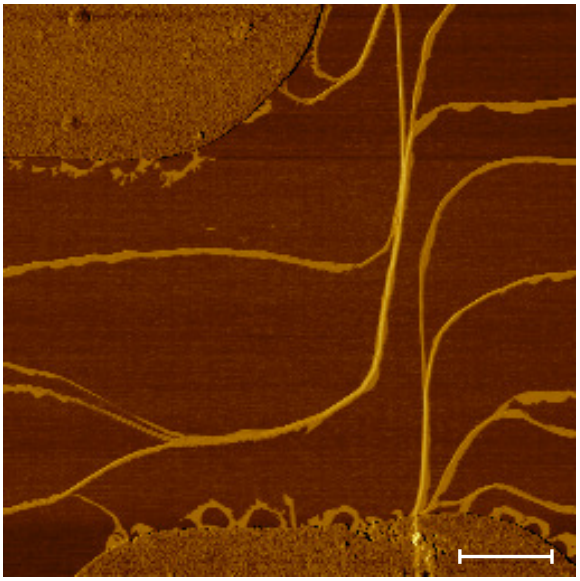

Figure 3.11: LFM image of a discontinuous SWGNR. When natural steps of a crystal are aligned vertical to the mesa direction, a long growth recipe that enables the step flow can cause a split in the 20 nm tall mesa. In this example the natural steps of the crystal is in the ZZ direction, while the mesa is in the AC. An opposite picture can be obtained for a chip with natural steps in ZZ direction and mesas in AC. Therefore, no dependence of this phenomena on any of the main directions (AC or ZZ) can be generalized. The scale bar is $1\mu m$ long.

angle which varies on a wafer due to the miscut being a localized parameter, which means that the miscut angle can change at different locations on a wafer.

The sidearm formations in Figure 3.12 that have the 30° angle to the main SWGNR shouldn't be attributed to the 30° angle between ZZ and AC ribbons. During the growth tests of hundreds of SWGNR samples in various directions, no link was found between the special ZZ and AC directions and the graphene growth.

Conventional SWGNR (Figure 3.10 (a)) fabrication process starts with the spin coating the chip with an organic resist. Then lithography techniques (exposure to UV with a mask in case of photo-lithography or exposure to electron beam in case of the E-beam lithography) are used to define the mesa areas. Once these areas are developed and a resist mask in the shape of mesas is established on the SiC surface then the structure etched with RIE etching technique by using 1:4 mixture of SF_6 and O_2 gas flows (0.8 SCCM to 3.2 SCCM)

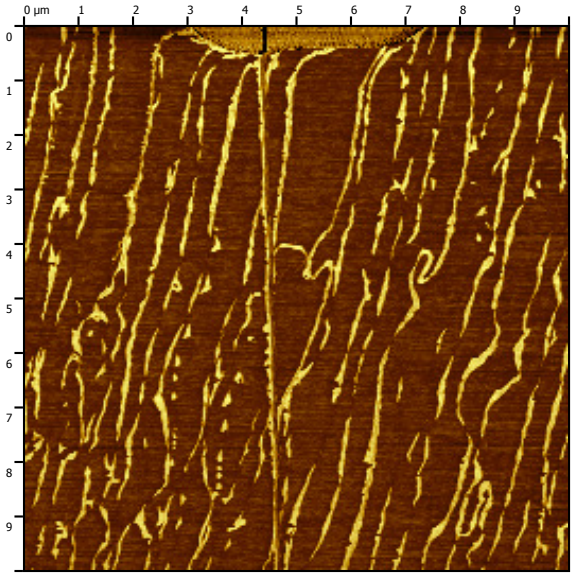

Figure 3.12: LFM scan of a conventional SWGNR. The straight bright line in the middle which is connected to the contact on top of the figure shows the actual SWGNR. Every other bright line that roughly makes 30° to the SWGNR in the middle is a sidearm formation.

at 100W RF power. Applying this recipe for nearly 14 seconds give 20 nm deep steps on the SiC surface. Sidewalls of these steps later can be used to grow SWGNRs.

The conventional SWGNR method causes sidearms that emerge as ribbon lengths increase and it needs to be solved for more consistent measurements. For certain samples complicated ribbon geometries can lead to unusual transport measurements (additional uncategorized measurements are given in appendix). Consistently for such samples, it is found that the main source of uncertainty in transport and magneto-transport measurements had been the overgrown graphene amount that randomly shorts ribbons. Sidearms make the geometry of a SWGNR more complicated than the geometry of a confined epigraphene ribbon (Figure 3.12).

Sidearms are shown to be a factor that lower the mean free paths of SWGNRs [128]. In order to avoid and suppress the sidearm formation an alternative approach in the growth process has been developed. Small steps of the SiC crystal form slightly taller structures (2nm to 5 nm) when the chip is exposed to high temperatures (in the range of $1500^\circ C$). There are two types of step flow, the first one is the flow of the step due to crystal dynamics,

and the second is the retraction of the steps due to the thermal decomposition during the graphene growth.

In order to avoid sidearms, two paths can be followed: first is to choose on-axis wafers and second is to utilize the natural steps into GNR growth. The miscut is a local effect, therefore it would be unlikely to obtain uniform miscut angles on on-axis wafers. Also the wafer cutting technology needs to give atomically flat surfaces on lengths that are comparable to the size of the chip or to the diameter of the wafer. The second path is to utilize the natural steps into SWGNR fabrication (Figure 3.10 (b)). If the natural steps with heights that are comparable to the conventional SWGNR mesas (20 nm) can be obtained, then the etching of mesas and the possible oxygenation effects [129] that come from RIE etching can be avoided. The steps can be utilized as processing free natural structures that can host GNRs on their sidewalls. A pre-growth annealing (pre-annealing) method needs to be introduced to obtain stable natural steps. Such structures can resist the step flow and graphene grown on them can be confined to the sidewalls.

3.2.3 Annealing of SiC

Utilizing the natural steps of a SiC chip for SWGNR growth requires two conditions: high temperature exposure to promote the step bunching and suppression of graphene growth during the process. Since epigraphene growth happens due to the thermal decomposition of SiC, preventing Si sublimation from the surface can be used as a method. This can be achieved by using a closed crucible in a pressured chamber. A closed crucible can contain the sublimated Si vapor and the higher external pressure ($2atm$ Ar) further reduces escaping of the Si. Moreover additional Si vapor pressure can be introduced to the inner volume by using a crucible that has Si saturated walls.

Figure 3.13 shows the annealing furnace setup. This setup enables heating of the crucible while flowing gas through the system above atmospheric pressure. The step bunching process is as follows: first the closed crucible is saturated in Si by melting Si chips at

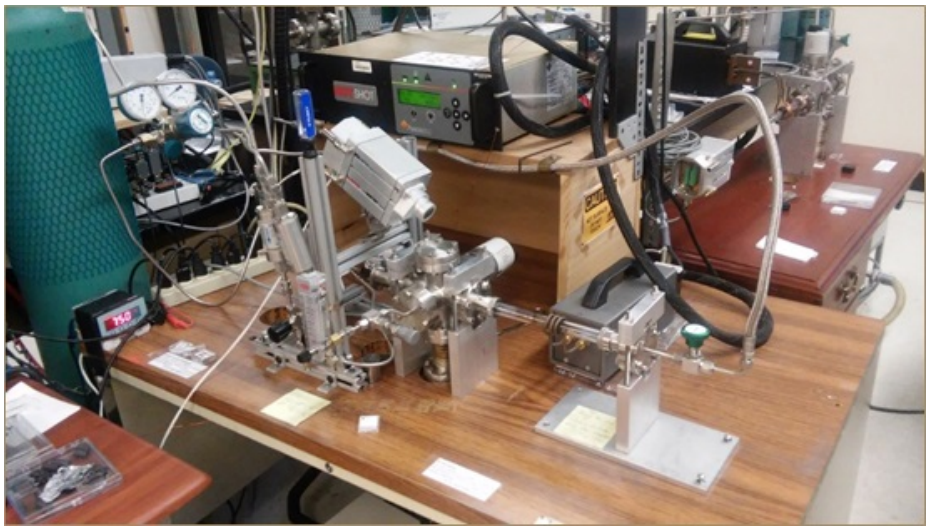

Figure 3.13: The annealing furnace is similar to the growth furnace except that it is designed to allow gas flow along the tube during the heating. Heating the crucible in Ar atmosphere helps suppressing the internal Si vapor and having high Si pressure in the crucible prevents any graphene growth. Inner pressure of the chamber can be set by the regulator of the canister while the flow through the system can be set by the mass flow meter at the end of the chamber. Typically 16 psi Ar pressure above the atmospheric pressure is chosen with 4 SCCM flow rate.

$1500°C$ for an hour, then six to eight chips are stacked face to face [130, 131] (polished faces) into this crucible (Figure 3.10 (b)). Having chips stacked upon each other creates additional confinement and can be considered as an additional preventative measure for Si sublimation, so for any possible epigraphene growth. Heating the crucible under 16 psi Ar pressure above the atmospheric pressure with 4 SCCM flow rate up to $1700°C$ for two hours results in bunched large natural steps.

After the annealing, natural steps as large as 20 nm can be obtained (Figure 3.14). Taller steps are followed by larger plateaus indicating that all the steps in that region have bunched into a single structure. Smaller steps are followed by narrower plateaus indicate that the step flow hasn't been completed (Figure 3.14).

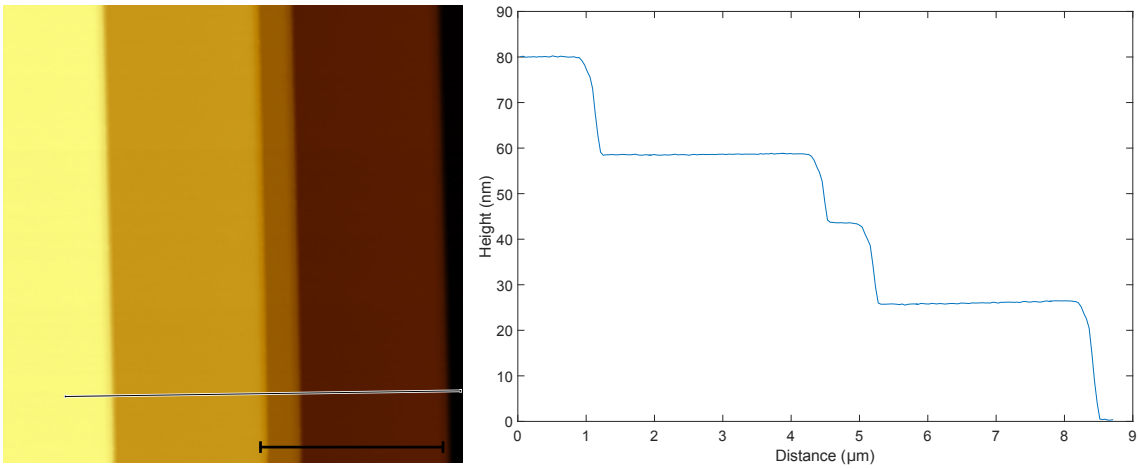

Figure 3.14: Left: Six face to face stacked SiC chips are annealed in a closed crucible in Ar atmosphere at $1700°C$ for 2 hours. After the annealing, steps as tall as 20 nm can be obtained. Right: The line profile taken on the section that is marked on the topography scan on the left. The scale bar on the left is $4\mu m$ long.

3.2.4 Natural Step Ribbons

Another feature of natural steps is their step flow dynamics during the epitaxial growth. Since the steps are stabilized at high temperatures prior to the CCS step, they don't tend to flow during the graphene growth. This enables faceting during graphene formation (i.e. slope change as described in Figure 3.8). Si sublimation at sidewalls still occurs on natural steps but since the steps are stable, they don't tend to retract but rather they change their angles to compensate for the volume change. This results in graphene to be formed on the $27°$ facet. Natural steps that can reach up to 20 nm heights after the annealing can form stable structures that can resist the step flow during the growth. Smaller natural steps tend to release a sub-step that flows over the plateau during the graphene growth and these mini steps form meandering sidearms formations. Even though meandering steps (Figure 3.15) are still sidearms, their density is much less that the sidearm density of a conventional SWGNR production (Figure 3.12).

Different growth regimes can be chosen for different step formations and the amount of meandering steps can be lowered by choosing the right one. A slow growth process means

having a lower temperature for longer duration. Choosing a smaller leak hole crucible for the same temperature but longer time periods can give the same slow growth conditions. The total Si vapor escaping from the SiC surface corresponds to the total graphene amount on the SiC surface, however the total amount is estimated for systems with a constant leak rate, for systems that are in equilibrium. Fluctuations in the Si leak rate can change during the growth process and can put the system into a non-equilibrium state. As the graphene growth starts and in case a nucleation center is introduced (a small step escaping from a larger structure), then the graphene growth can start on the plateaus. But the overgrowth on the plateaus requires the sidewall to be covered with graphene first. Figure 3.7 first shows SWGNR formation, the overgrowth that starts on the right side of the ribbon can be seen in the scan given on the left. In the same figure the LFM scan on the right shows what happens when that overgrowth covers the plateaus. Therefore, if the overgrowth (a monolayer graphene formation from a step to a meandering step) is not present then it can be concluded that the step flow happens before the graphene growth on the sidewall starts. Therefore, if graphene can be grown before the step flow starts for such a system, then more confined SWGNRs can be obtained. This shouldn't be a common strategy to grow graphene for all natural steps but only for those that give meandering ribbons detached from the main ribbons. The right graphene growth regime can be chosen by observing the step flow dynamics of the wafer and the selection can help confining the morphology of SWGNRs.

For example a meandering step, which initiates from an unsaturated natural step formation, can start flowing on the surface at high temperatures. If the temperature is high enough it can grow graphene on the plateau, if not it can flow till the growth starts and the form a meandering ribbon formation, rather than a monolayer on the plateau. This means a better morphology can be obtained by keeping the growth regime short, so that meandering steps don't start traveling on the flat surfaces.

Figure 3.16 shows contacted narrow natural SWGNRs. The improvement from Fig-

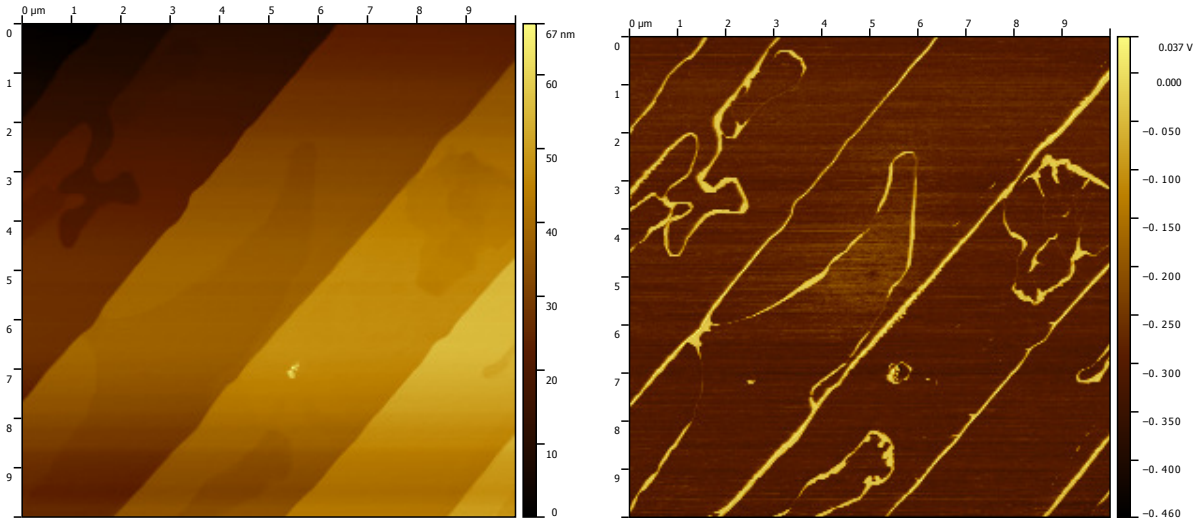

Figure 3.15: Topography and LFM of natural step SWGNRs after growth. The area is same as the sample in Figure 3.12, yet the density of sidearms is much less. Also the height of natural steps are enough to pin the steps after growth, which gives straight ribbons. Meandering steps that emerge after the growth can be avoided by optimizing the growth recipe.

ure 3.15 comes from the selection of a faster growth regime that worked better for the step flow dynamics of this wafer.

3.2.5 Comparison of Nanoribbon Growth Techniques

The effect of step flow on the graphene confinement of a natural step system, which utilizes annealed SiC steps, can be optimized by choosing the convenient growth regime. However, natural step system removes the scalability feature of SWGNRs, since the natural step directions are straight, but the density of the ribbons are random (on a chip). But combining all the observations done on the SWGNR growth, it can be concluded that if the step flow can be controlled and if the initial conditions of the crystal (step heights and facet angles) can be controlled, then confined SWGNRs can be grown at desired locations. The observations that show how steps flow and faceting happens for etched mesas and natural steps (Figure 3.21 and 3.24) are presented in the Experimental Measurements chapter. Before and after graphene growth images of anchored SiC steps that show how facets and

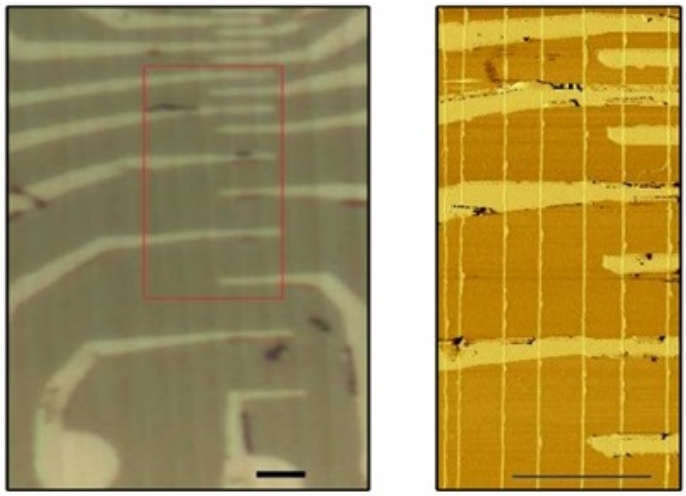

Figure 3.16: Natural step SWGNRs that has amorphous carbon contacts. The image on the left shows the optical image and the right image shows the LFM scan of the area that is marked on the left. Sidearm and meandering ribbon free graphene ribbons are obtained by choosing a faster growth regime that worked for the step flow dynamics of this wafer. The scale bars are $5\mu m$ in both cases.

morphology changes, are used as the experimental proofs of the statements made in this section.

If the step can be stabilized prior to the graphene growth and if the initial facet can be brought to a certain angle, then the SWGNR growth can follow the trend in Figure 3.9. However, if the steps retract and no faceting occurs then a controlled and scalable SWGNR growth can't be obtained. In this sense, the annealing method is combined with the etched mesa technique to see if the initial conditions can be tailored. Once the required facet angles are obtained in a step stabilized system, then growth recipe can be optimized to give confined SWGNRs on stable facets.

Figure 3.18 shows the topography and error obtained from AFM scans of an annealed mesa structure. By first etching mesas on SiC with patterning and RIE and then applying the annealing procedure to these chips, initial facet angles of mesas can be controlled (still not consistently). This requires finding the annealing recipe that gives the desired facet angle. If such a facet can be obtained through an annealing recipe then a growth recipe can optimized for such a system. Figure 3.19 shows after growth facets of a confined

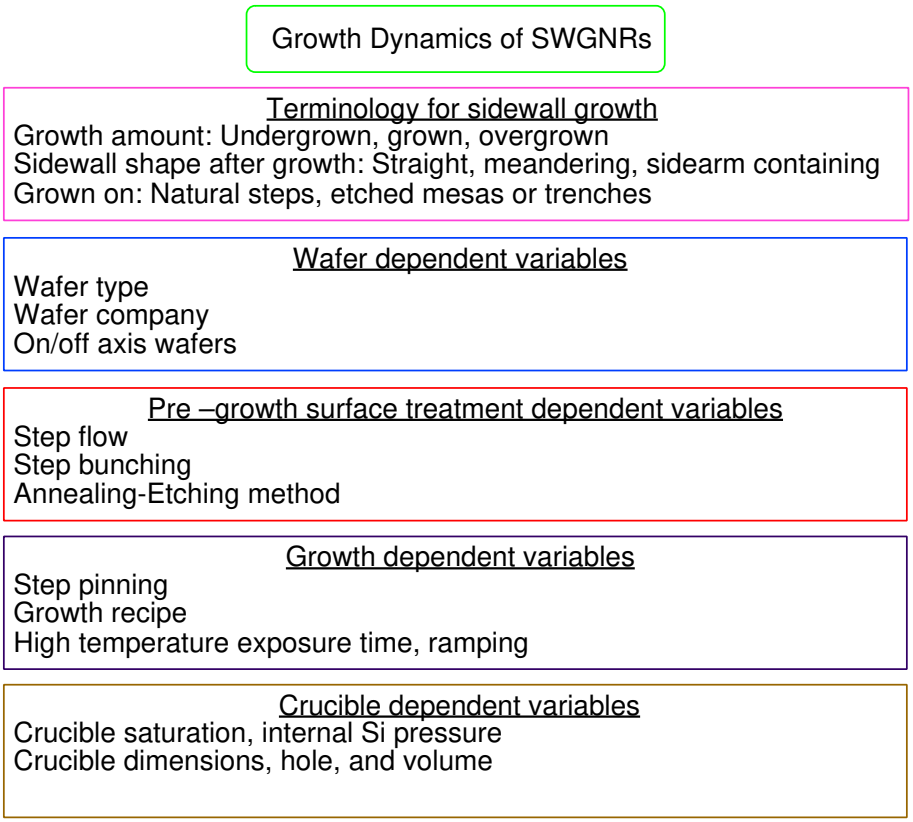

Figure 3.17: The terminology list used to to explain the morphology and the growth of SWGNRs.

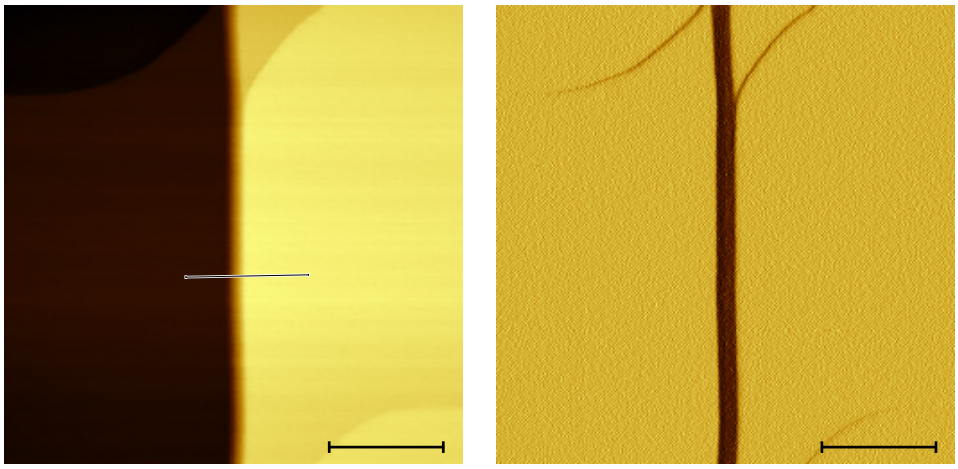

Figure 3.18: Topography and error signal of a 20 nm tall annealed step. At this stage it has no graphene, but since the chip is annealed step flow is saturated. Therefore, only faceting due to graphene growth is expected. the line profile across the step shows 16° facet angle, which is very close to the desired initial angle needed for monolayer growth on a 20 nm tall step(Figure 3.9). Left: topography of the step, right: error signal of the same scan that shows surface morphology. The scale bar is 500 nm long.

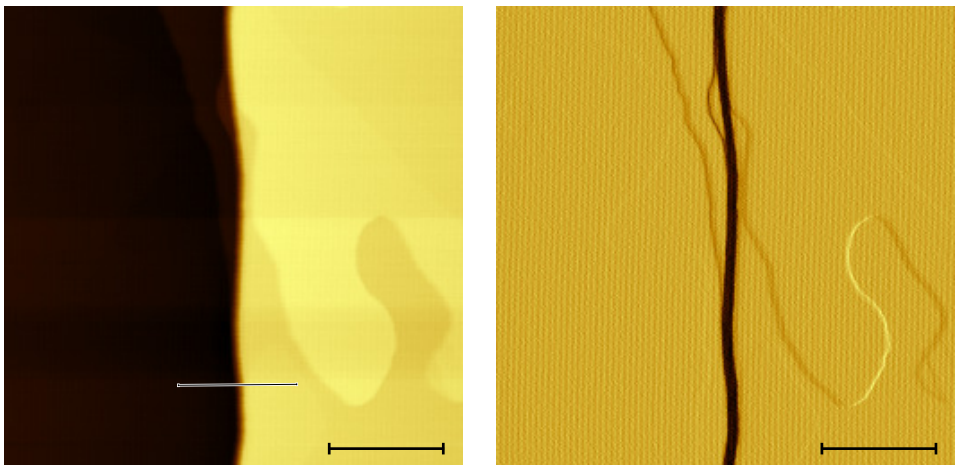

Figure 3.19: Topography and error signal of a 20 nm tall step after growth. The annealed facet in the previous figure turns into 27° facet. Left: topography of the step, right: error signal of the same scan that shows surface morphology. The scale bar is 500 nm long.

SWGNR. The line profiles taken from both figures (Figure 3.20) show a transition from 16° facet angle to 27° facet angle. This corresponds the initial angle condition needed for a monolayer growth on the sidewall of a 20 nm tall step, given in Figure 3.9.

3.3 Observation of the Step Flow and Faceting During Graphene Growth

In order to understand the role of step flow and the faceting (the change in the sidewall angle) in the final SWGNR morphology, before and after growth comparisons can be done on a system. However, in order to understand the effects of the two variables separately, two systems that can isolate at least one variable are needed.

For the case of pre-annealed chips, natural steps on the surface are flow saturated structures. Since the natural steps are already annealed at $1700^\circ C$, graphene growth temperatures on the order of $1500^\circ C$ are not expected to cause any additional step flow. However, if the step is not a flow saturated stable structure (small step) then it may start flowing before graphene starts growing on the surface.

The surface of a pre-annealed SiC chip before and after graphene growth can be seen in Figure 3.21. aC strips are placed as reference points to pin the steps at certain loca-

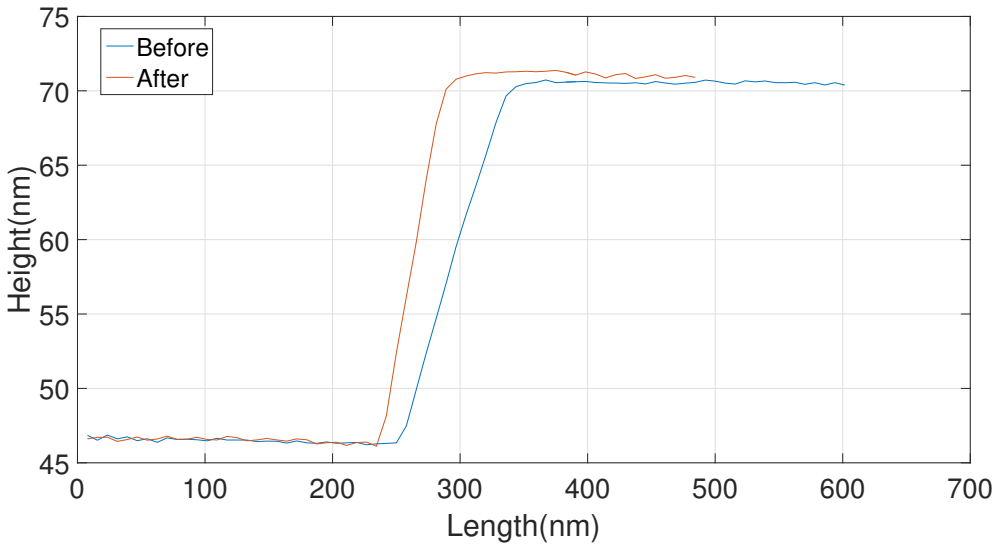

Figure 3.20: Line profiles from the previous two figures. The facet turns into 27° from 16°.

tions [132]. this way, that an observation of a shift in steps can be done with reference to these pinning centers.

Different lengths are chosen to study the effect of different initial conditions (ribbon length) on graphene growth. AFM error signal is chosen for this comparison since it is proportional to the derivative of the topography signal and gives a single contrast for all steps simultaneously, rather than staircase contrast that would be obtained with the topography data. The change in positions of the steps (or the total step flow) can be seen by the comparison of the cross sections indicated by the dashed lines. These cross section are given in part c) of the same figure.

Steps, unless small, remain almost at the same location, unlike the step retraction model that was proposed to explain the step flow dynamics during epigraphene nanoribbon growth [123].

The inset in Figure 3.21 c) shows the change in the tallest step (70 nm), but the tip radius is too high to precisely determine the steepening angle of the step during the growth. The inset show a 14° change in the facet angle, from 12° to 26°. The change in volume

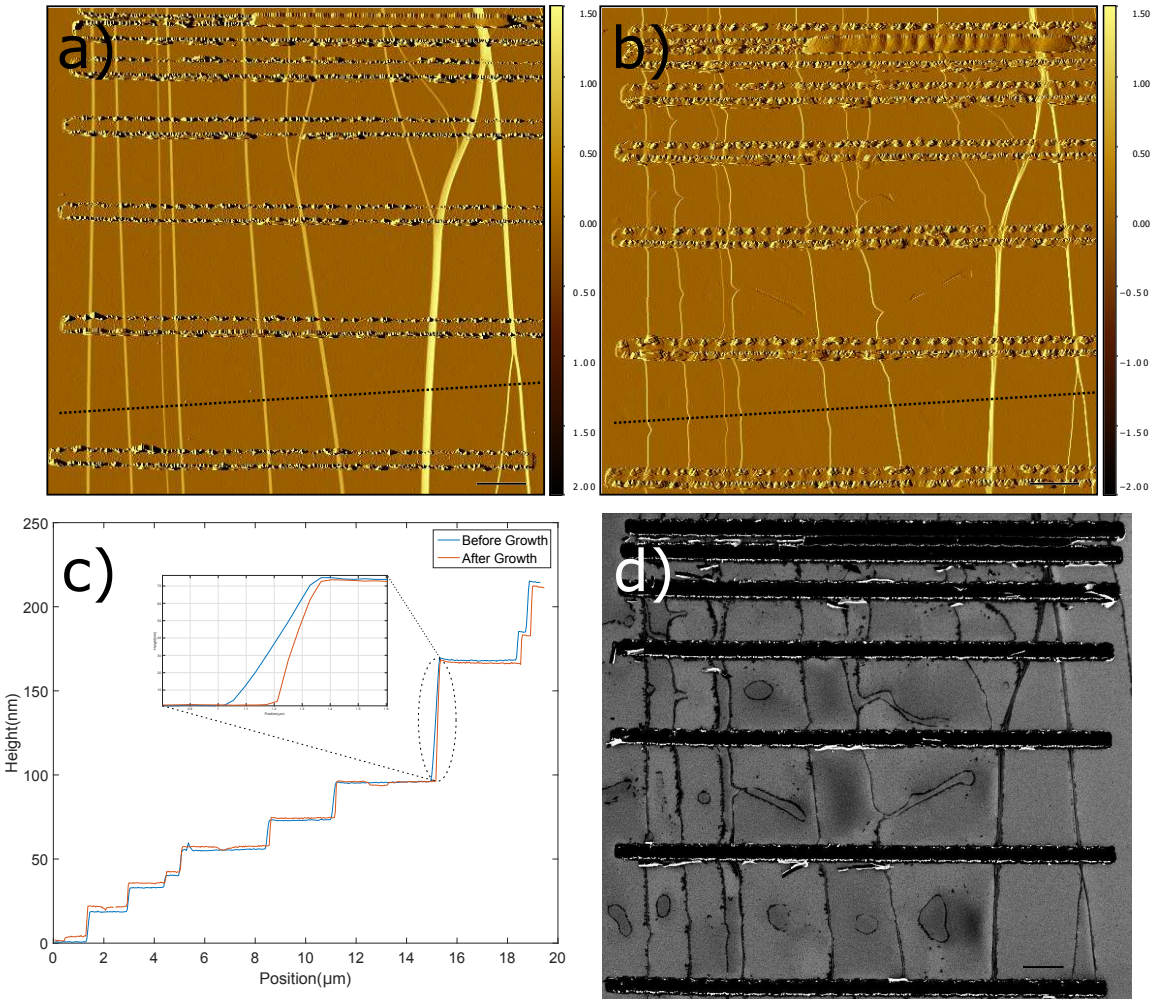

Figure 3.21: Before after graphene growth imaging of pre-annealed SiC steps. a) The error signal of a large AFM scan taken after SiC annealing in Ar. b) The same scan after the epigraphene growth. The scale bars in parts a and b are $2\mu m$ long. c) The line profiles marked in parts a) and b) are plotted on top of each other. The inset shows the steepening of the tallest step. This change is also visible in parts a) and b), the widths of the tallest step are significantly different. d) SEM image of the same region shows graphene covered areas. darker color corresponds to graphene. The scale bar is $2\mu m$ long.

can be calculated and since the thickness of SiC that needs to thermally decompose to give a monolayer graphene is known, the number of layers of graphene on this sidewall can be determined (provided that graphene stays on the sidewall). However, unless the angle is measured very precisely this calculation can be deceiving. Figure 3.21 d) is the SEM image of the same area. Darker regions are where the graphene is on the surface. SEM is preferred over LFM since the area is large and SEM can give better contrast for this scale.

It can be seen from Figure 3.21 that flow saturated steps can supply the volume change for graphene growth by steepening their sidewall facets (if the step is stable (large steps)). Smaller steps don't survive the graphene growth temperatures and they start flowing on the surface.

Normally, for the case of overgrown ribbons, monolayer graphene grows over the plateau above the sidewall. Since this is not the case for the pre-annealed samples, it can be claimed that for the small steps, the step flow starts before the graphene growth. Therefore, the possibility of step flow being initiated by ribbon growth is excluded.

Epigraphene on SiC can also be obtained in Ar atmosphere. The required confinement by the pressure can be obtained by supplying an external constant noble gas pressure, which is generally Ar. Graphene obtained using this method generally gives finger like structures (arrows) that are similar to the sidearms of our experiments. An analysis [133] of the Ar based growth system reveals that the graphene growth is strongly dependent on the initial surface morphology. The study also shows that arrow features are formed and limited by diffusion of carbon atoms (analogous to the study [134] that shows how gallium droplets flow on the gallium arsenide surface as arsenic evaporates from the crystal upon heating). When there is a lack of the carbon nucleation centers (graphene ribbons acting as carbon sinks), the carbon on the surface starts building up. Then, due to the excessive carbon amount, Si sublimation slows down and the step flow stops.

The self limiting nature of the arrow features [133] can be the underlying mechanism of the few small steps forming sidearms on the plateaus of the pre-annealed SiC chips

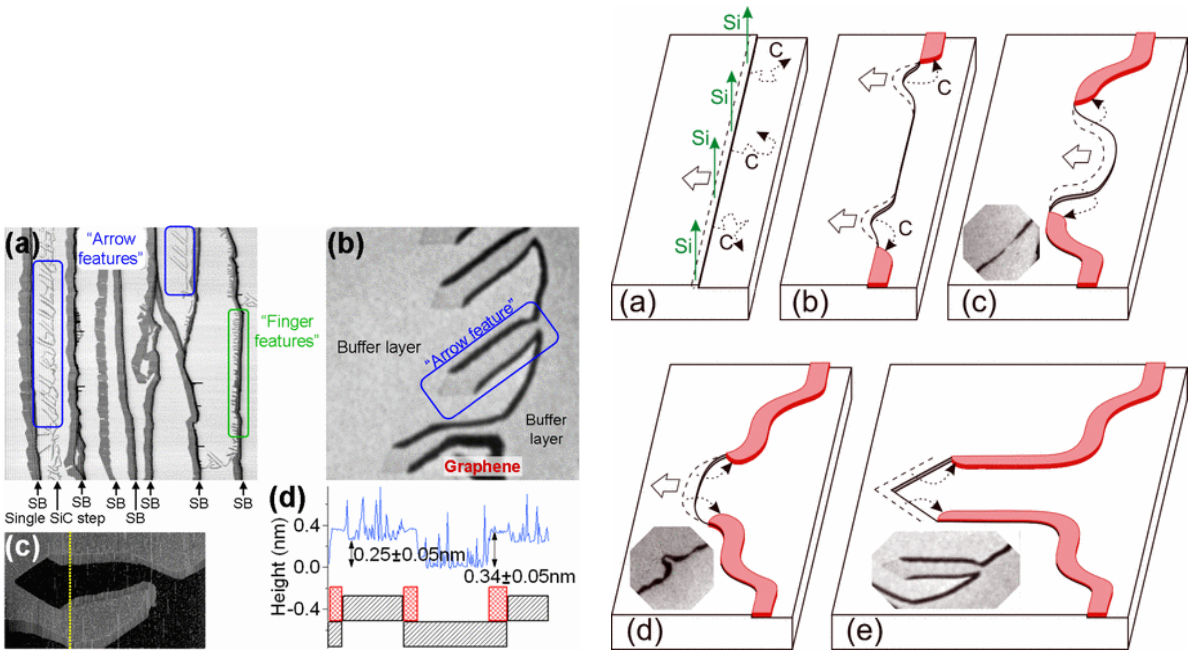

Figure 3.22: The morphology of the arrow features (Left) from an Ar growth system. The cross section (d) of buffer layer (black boxes) and monolayer graphene on top (red boxes) give the expected heights. A schematic of the formation of the arrow features (Right) shows that as Si sublimates from the surface, the leftover carbon atoms nucleate graphene ribbons along the step edges. This process continues till an arrow-like feature is formed. Reprinted figure with permission from [133]. Copyright 2010 by the American Physical Society.

(Figure 3.21 (d)).

The step flow due to graphene growth happens in different ways for different structures and different ribbon lengths. In Figure 3.21 a) and b) the second step from left bends in the middle of the ribbon and releases the step flow with a pointy bending. This disappears when the ribbon length goes down to $1\mu m$ and this pointy feature gets replaced with an arc. This can indicate two things. First, these dimensions (step length and height) may be related to the stress the crystal experiences during graphene growth and the final morphology may be the result of a low energy orientation. Second, as the ribbon length decreases and the aC strips get closer to each other, they act as carbon sinks. This means that the step flow due to graphene growth can be increased, since the carbon sinks allow more carbon diffusion on the surface. These arguments can be tested by observing the graphene growth on aC contacted short ribbons.

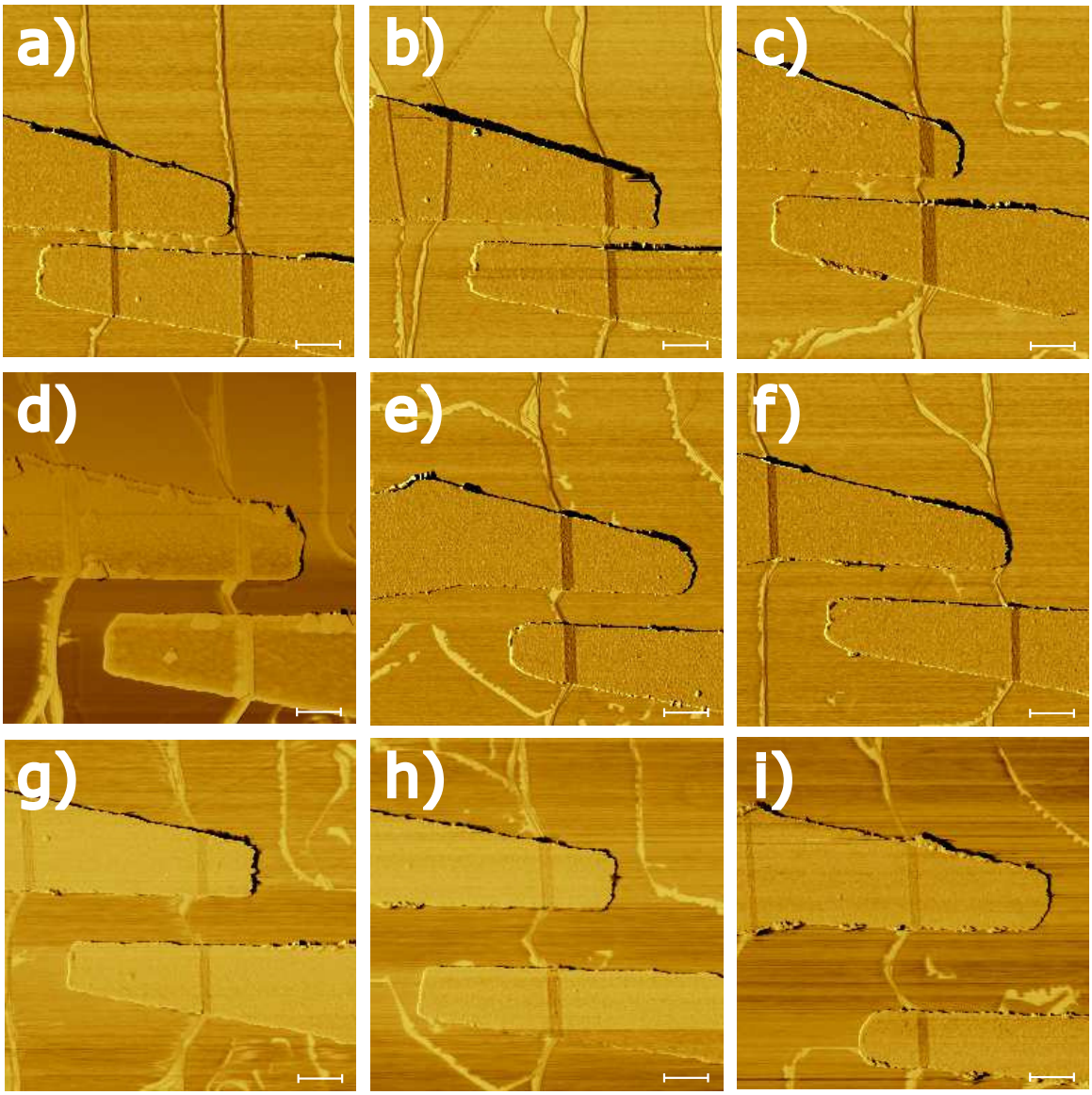

Figure 3.23: aC contacted short ribbons for the observation of arrow-like GNR formations. Ribbon lengths are 150 nm, 250 nm, 300 nm, 400 nm, 450 nm, 500 nm, 550 nm, 750 nm from (a) to (i) respectively. As the ribbon length increases the arrow features, which might be the low energy orientation of the crystal, turns into an arc shaped graphene ribbon. The left sides of the images are the taller regions of the step wise structure.. The scale bars are 500 nm long.

Depositing aC pads close to each other and then growing ribbons in between, give arrow-like graphene formations. The first thing to look at Figure 3.23 is the initial locations of the steps under the contact areas. The steps are pinned under the aC contacts and they remain unchanged upon graphitization. It can be seen that the steps were initially wider and upon graphitization, in between the aC stripes they start flowing towards the left side. Also, due to the anchoring effect of the aC strips, they tend to bend around the contacts. Figure 3.23(f) shows that a step (the left most step), which hosts a straight GNR, bends near the contact. However, as it can be seen from Figure 3.21, given the long ribbon length, a step can be kept at the same location after graphene growth. Therefore, the bending effect in Figure 3.23 should be attributed to aC contacts being too close to the GNRs from both sides and interfering with the growth dynamics of the ribbon.

The main difference between the arrow-like features of the Ar grown samples (Figure 3.22) and the natural step samples (Figure 3.23) is that arrow like features contain no graphene at the arrow part of the step and natural steps have graphene on them. Therefore, the arrow-like features for the natural step ribbons are in fact a result of the additional growth which is enabled by aC contacts acting as carbon sinks. On contrary, the arrow shapes of the Ar growth are the result of a self limited suppressed growth.

The analysis of graphene grown on pre-annealed steps and the reasoning behind the dynamics of the finger like morphology of the graphene grown on small steps are given in the first half of this subsection with Figure 3.21 and Figure 3.23. To complete the initial goal, which was to understand the effect of step flow in the ribbon morphology, another set of samples are prepared and observed in a similar manner to the one in Figure 3.21, except this time etched mesas are used to obtain SWGNRs.

SWGNR production starts with dry etching of mesas into the SiC. These artificial structures are likely to be affected from the internal crystal dynamics at elevated temperatures and some step flow on and around the mesas is expected. The AFM and SEM measurements presented in Figure 3.24, which show the morphology before and after the graphene

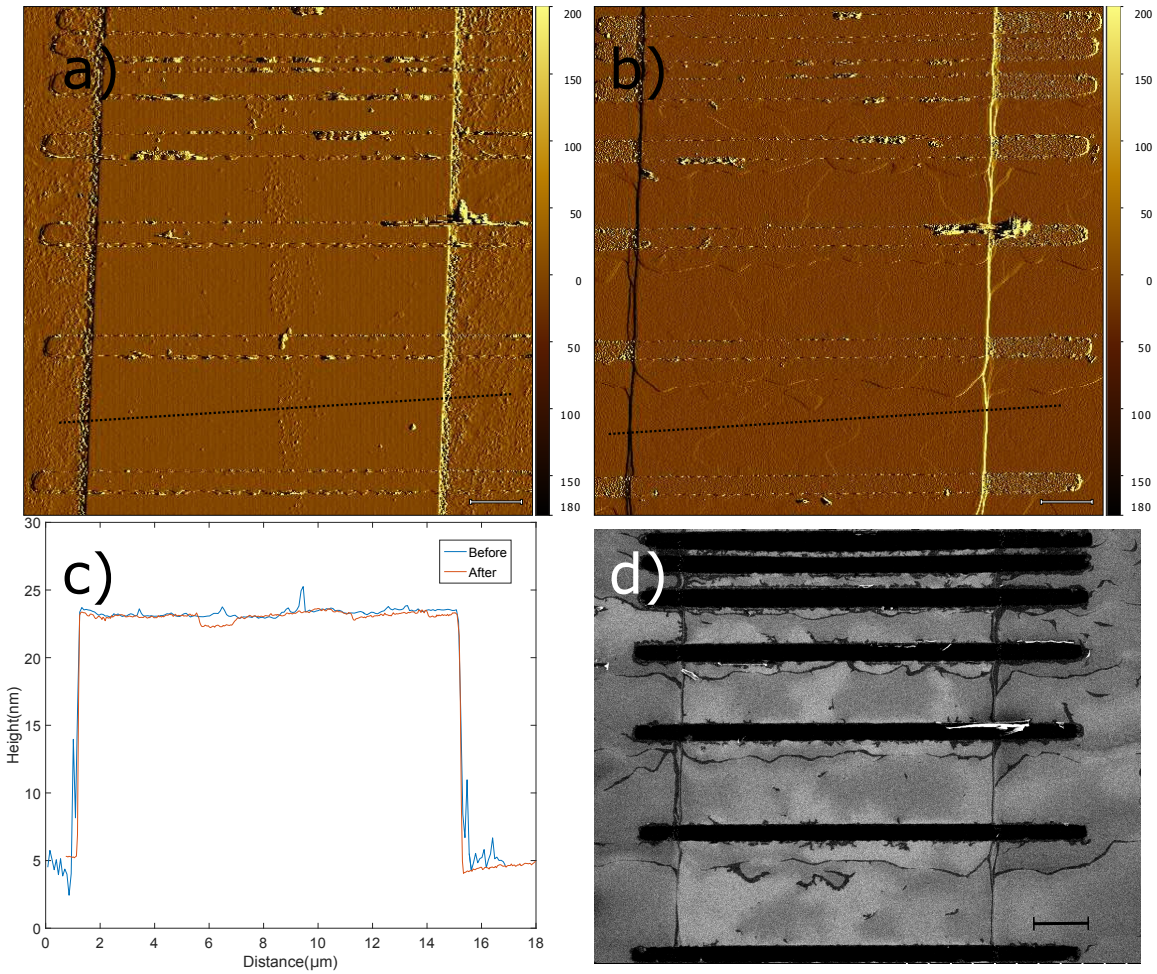

Figure 3.24: Before and after graphene growth imaging of etched mesas in a conventional SWGNR system. a) The error signal of a large AFM scan taken after RIE etching and aC contact placement. b) The same scan after the epigraphene growth. The scale bars in parts a and b are $2\mu m$ long. c) The line profiles marked in parts a) and b) are plotted on top of each other. There is not a steepening, but maybe a small retraction in step positions. d) SEM image of the whole area shows graphene covered areas. darker color corresponds to graphene. The scale bars are $2\mu m$ long.

growth.

The growth regime of the SWGNRs in Figure 3.24 is optimized for minimum sidewall growth and maximum confinement. Therefore, the sidearm ratio is lowered as much as possible (compared to Figure 3.12). The sidearm density of this region is also interrupted due to having aC strips in the vicinity of the steps and stopping the steps from forming more regular structures. Therefore, the density of the sidewalls are neglected for this system, and only the faceting and the step motion of the etched steps are observed. By looking at the line profiles before and after the growth –for the most optimized growth conditions– etched steps don't change angle, but they retract a very small amount which is enough to form monolayer graphene on the sidewall. The corresponding displacement is too small to be measured accurately with AFM. However, the facet angle stays almost the same, which can be observed through the comparison given in the inset.

By looking at Figure 3.21 and Figure 3.24 it can be said that SWGNRs grown on step flow saturated structures (pre-annealed natural steps, Figures 3.21) go through faceting during the graphitization. This means steps remain in the same location, but they change their sidewall angles during graphene growth. The volume difference in the new and the old structures corresponds to the SiC amount that needs to be thermally decomposed to form monolayer graphene on the sidewall. The reason behind faceting happening instead of a step flow may be the suppression of the step flow through annealing method. The argument is also supported when we compare this morphology to the one of artificial mesa structures (etched mesas, Figures 3.24), where faceting doesn't happen for similar graphene growth conditions.

Faceting is a more controlled way of growing since the initial and final angles can be measured and the corresponding change can be estimated (Figure 3.9). Therefore, annealing can be implemented to first find the desired initial facet angles for a step. Then the growth recipe can be optimized for the final facet angle, the resulting ribbon morphology can give confined SWGNR formations on the surface.

CHAPTER 4
TRANSPORT MEASUREMENTS

In this chapter I will present the transport features of SWGNRs and our measurements that indicate mean free paths that range from $1\mu m$ to $10\mu m$ at room temperature.

A brief introduction to the mesoscopic transport theory and the Landauer equation were given in the first Chapter. Following that discussion, an analysis of nanoribbon mean free paths will be made over transport measurements. I will discuss the effect of sample contamination, graphene morphology (edge length) and measurement techniques on mean free paths of ballistic SWGNRs.

4.1 Mean Free Path Measurements

4.1.1 Conventional Graphene Nanoribbons

The resistance vs length measurement presented in Figure 4.1 has 48 contacted conventional SWGNRs with various lengths. Each point in Figure 4.1 corresponds to a single nanoribbon with two aC pads. Two point resistance measurements are taken with a lock-in amplifier by applying 100 nA current amplitude (modulated at 17 Hz) while measuring the voltage through two contact pads with the same lock-in. The measurements are taken both in air and inside the vacuum probe station (in $10^{-6}mbar$ after an annealing at $260^{\circ}C$) to see the change in the mean free path. The first set of measurements done in air gives the linear fit $R(L) \approx 13.0L + 13.1$ with uncertainties in coefficients (from the linear fit in the form of $R(L) = aL + b$) $a = 13.0 \pm 0.6k\Omega/\mu m$ and $b = 13.1 \pm 10.4k\Omega$. Following mean free path calculation gives:

$$\Lambda_{air} = R_o/a = 25.8k\Omega/(13.1k\Omega/\mu m) \approx 2\mu m, \tag{4.1}$$

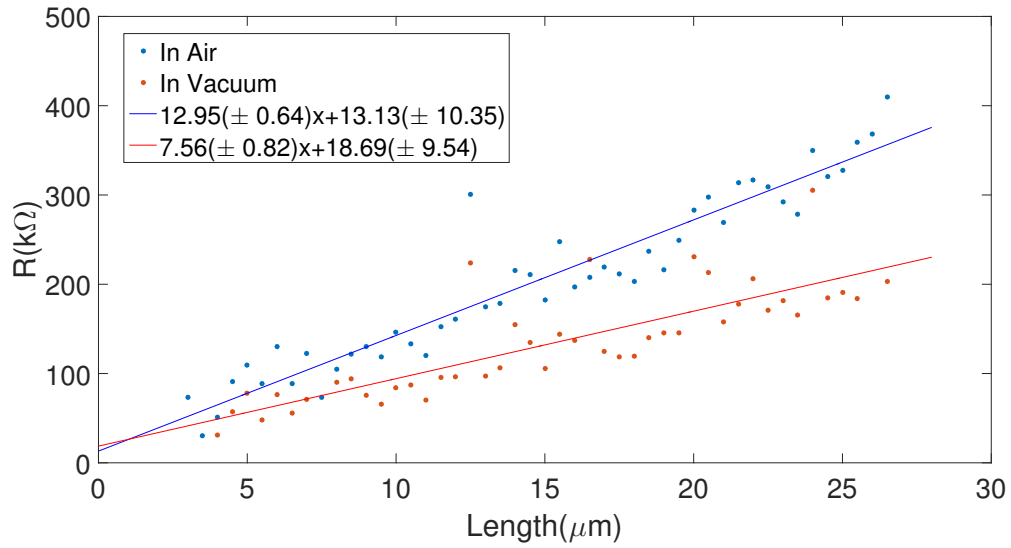

Figure 4.1: Resistance vs length measurements of conventional SWGNRs with channel lengths ranging from $3\mu m$ to $26.5\mu m$. The same measurement is taken both in atmospheric conditions at room temperature and in vacuum probe station after annealing the sample at $260°C$. The slopes of the resistance profiles decrease upon annealing.

adding the lower and upper bounds of the a coefficient ($a = 13.0 \pm 0.6k\Omega/\mu m$) gives the interval $\Lambda_{air_{min}} = 1.9\mu m$ and $\Lambda_{air_{max}} = 2.1\mu m$. This calculation is carried in the long limit which is shown in Figure 1.7 (b) ($L > 3\mu m$).

After annealing the same sample, the slope of the resistance vs length profile decreases giving the new coefficients $a = 7.6 \pm 0.8k\Omega/\mu m$ and $b = 18.7 \pm 9.5k\Omega$. Carrying out the same mean free path calculation for the new data gives:

$$\Lambda_{vac} = R_o/a = 25.8k\Omega/(7.6k\Omega/\mu m) \approx 3.4\mu m, \tag{4.2}$$

adding the lower and upper bounds of the a coefficient ($a = 7.6 \pm 0.8k\Omega/\mu m$) gives the interval $\Lambda_{vac_{min}} = 3.1\mu m$ and $\Lambda_{vac_{max}} = 3.8\mu m$. Annealing the chip in vacuum and performing the measurement without exposing the sample to air increases mean free path from $2\mu m$ to $3.8\mu m$.

The contact resistance can also be found from the linear interpolation given in Fig-

ure 4.1. For the long length regime the interpolation should reach the value $\alpha R_o + 2R_{lead} + 2R_{interface}$ (where α is anything between 1 and $\frac{1}{N}$ as mentioned in Chapter 1). We don't know what the $R_{interface}$ resistance is, but we can estimate $R_{lead} = 1 - 5k\Omega$, from the resistance of annealed carbon pad and their geometrical factor. For the first data set, the interpolation goes to $b = 13.1 \pm 10.4k\Omega$. This value is close to that of the annealed sample ($b = 18.7 \pm 9.5k\Omega$) and lower than $R_o = 25.8k\Omega$, this result is compatible with a ballistic channel that dominates at long length (as shown in Figure 1.7 (b)). Another estimation of the number of channels will be made once the contact resistances are identified with conductive probe spectroscopy later in this chapter.

Higher contamination levels mean increased scattering events (decreased mean free path). Cleaning the sample can also be lowering the doping and Fermi level while decreasing the impurity scattering (increasing the mean free path), as clearly seen in Figure 4.1 between the data in air and in vacuum.

The mean free paths calculated in our nanoribbons and previously measured in SWGNRs [84] are momentum relaxation mean free paths that needs to be distinguished from phase relaxation mean free paths [135, 93] of phase coherent systems, where phase randomization doesn't occur (absence of inelastic scattering) over large length scales. Phase coherence requires low temperatures and our mean free path measurements are performed at room temperature.

4.1.2 Improved Graphene Nanoribbons

The data given in Figure 4.2 is obtained from natural step SWGNRs fabricated with the no post growth processing approach (Figure 2.3). The mask pattern shown in Figure 2.2(a) is used to build contacts on ribbons that have lengths ranging from $3\mu m$ to $26.5\mu m$. aC pads are lifted off from the pre-annealed chip and the SWGNRs are grown on natural steps. No ribbon isolation step (etching and exposure to resist residues after graphene growth) was needed since the ribbons are far away from each other by design, owing to improved

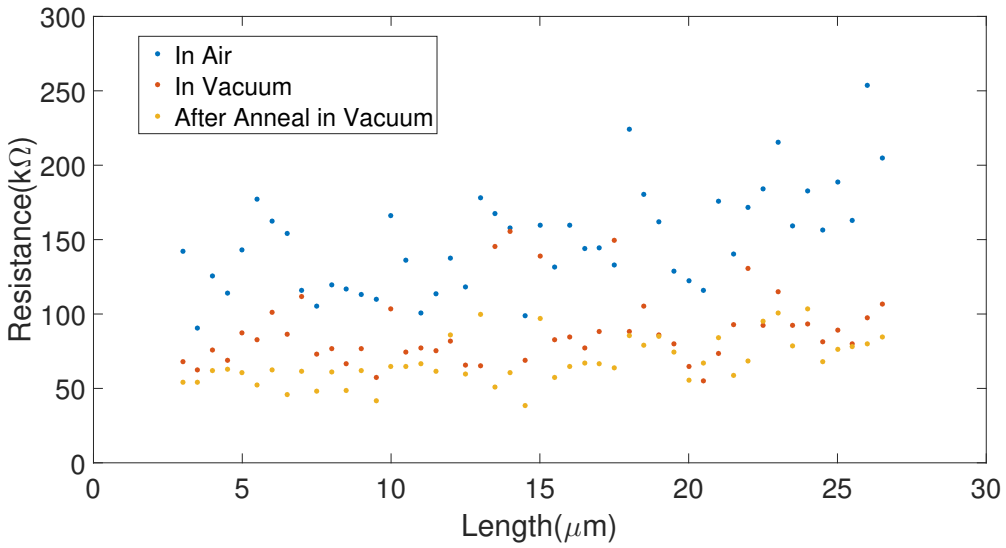

Figure 4.2: Resistance vs length measurements of 48 highly confined (morphologically) contacted SWGNRs with lengths ranging from $3\mu m$ to $26.5\mu m$. The same measurement is taken three time in different conditions. Every point is a single measurement made on an individual nanoribbon.

growth techniques.

The measurements (same lock-in based measurements as the previous section, $100nA$ modulated at $17Hz$) are first taken in air, then the sample is moved to the vacuum probe station and the chamber is pumped down to $10^{-6}mbar$. At this pressure another set of measurements is recorded. Lastly, the sample is annealed up to $260°C$ in vacuum and cooled back down to room temperature and a third set of measurement is taken (Figure 4.2). The overall resistance decreases as the measurement is repeated after each cleaning method. The unusual resistance vs length profile of the sample can be seen once the sample is measured after the last heat treatment in vacuum.

Figure 4.3 shows the final measurement in a single plot. The first visible aspect of the plot is the constant resistance region of $60k\Omega$ that goes up to $15\mu m$. The points scattered above and below the plateau are pads that are connected by multiple ribbons (lower resistance) or longer single ribbons (higher resistance) which can be identified individually

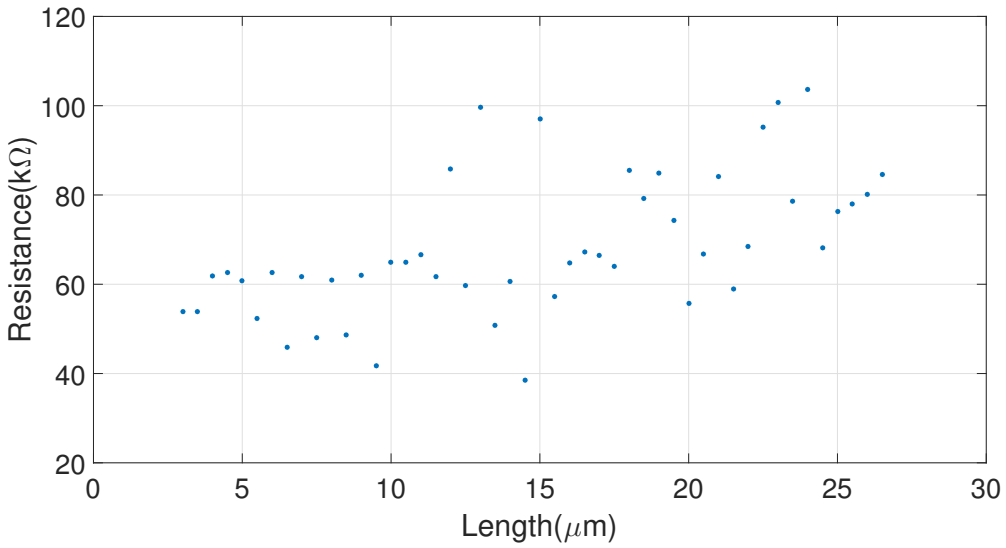

Figure 4.3: Isolated plot of the data "After Anneal" from Figure 4.2. The constant resistance region that goes up to roughly $15\mu m$. The resistance plateau also includes the contact resistance, which will be calculated in detail later in this chapter.

(detailed later in this chapter). To illustrate this effect a sketch of the ribbon distribution and the mask design is given in Figure 4.4.

Figure 4.4 (a) shows the details of the mask design and the distribution of the natural steps. the corresponding circuit diagram is given in Figure 4.4 (b). In order to have a negligible effect from parallel resistances R_1 and R_2, their total $R_1 + R_2$ should be on the order of few $M\Omega$, since the ribbon resistance is approximately on the order of $100k\Omega$ and the total parallel resistance is approximately $(R_1+R_2)/2$. Individual measurement of these resistances give values $R_A \approx R_B \approx 100k\Omega$ and $R_1 \approx 10M\Omega, R_2 \approx 1M\Omega$. Therefore, few approximations can simplify this resistor network and validate that a single measurement over R_A is at least in 10% range of the real R_A value. Details of such a calculation and relevant approximations are given in Appendix.

The pads that are designed to connect at least a single ribbon, but for pads far apart due to the slight misalignment of the natural step direction and the mask, capturing at least a single ribbon between the pads might fail. This is illustrated in Figure 4.4 (c).

Three factors affect the measurement of resistance of a SWGNR: the mask design, the ribbon density and a successful contact to the contact pads. The asymmetrical mask design (Figure 2.2(a)) creates a network of small and large resistances, that depend on the length of the ribbons that connect the pads. From previous work [84] we expect that ribbons longer than $\approx 15\mu m$ have an exponentially large resisitance.

Another factor that affects a single resistance measurement result is the possibility of contacting or not contacting the pads. This is investigated in the next section where few natural step ribbons that connect two pads are analyzed through conductive probe microscopy and found that only one of them makes good contact to both pads.

The plateau is localized around $60k\Omega$ up to $15\mu m$ nanoribbon length. $60k\Omega$ intercept consists of $\alpha R_o + 2R_{lead} + 2R_{interface}$ giving a minimum of $R_{lead} + R_{interface} = 17.5k\Omega$ per contact. Most of this resistance can be assigned to $R_{interface}$ since the sheet resistance of aC contacts is on the order of $1k\Omega/\square$ (Figure 2.9) and the lead design is roughly 5 squares, giving $R_{interface} > 12.5k\Omega$ (measured in vacuum, the following conductive probe microscopy (below) of natural step ribbons give higher $R_{interface}$ which is attributed to air exposure).

aC forms poly-crystalline structures once exposed to high temperatures [136]. These poly-crystalline interfaces might be the underlying reason of the high $R_{interface}$. Even though aC-graphene junction is a carbon to carbon connection, it might have high resistance due to a grain boundary type of interface, similar to c-axis electrical conductivity of graphite being lower than the on axis conductivity [137] of graphite. $R_{interface}$ in our setup may even be in the form of a tunneling resistance.

The measurement shown in Figure 4.3 is the longest ballistic transport length (assumed to be all along the $15\mu m$ plateau) obtained in this study. We attribute it to clean processing and measurement conditions, along with the advantage of avoiding an etching step (No post growth process mentioned in Figure 2.3) and the improved ribbon growth methods that help containing the graphene to the sidewalls and giving narrow ribbon geometries.

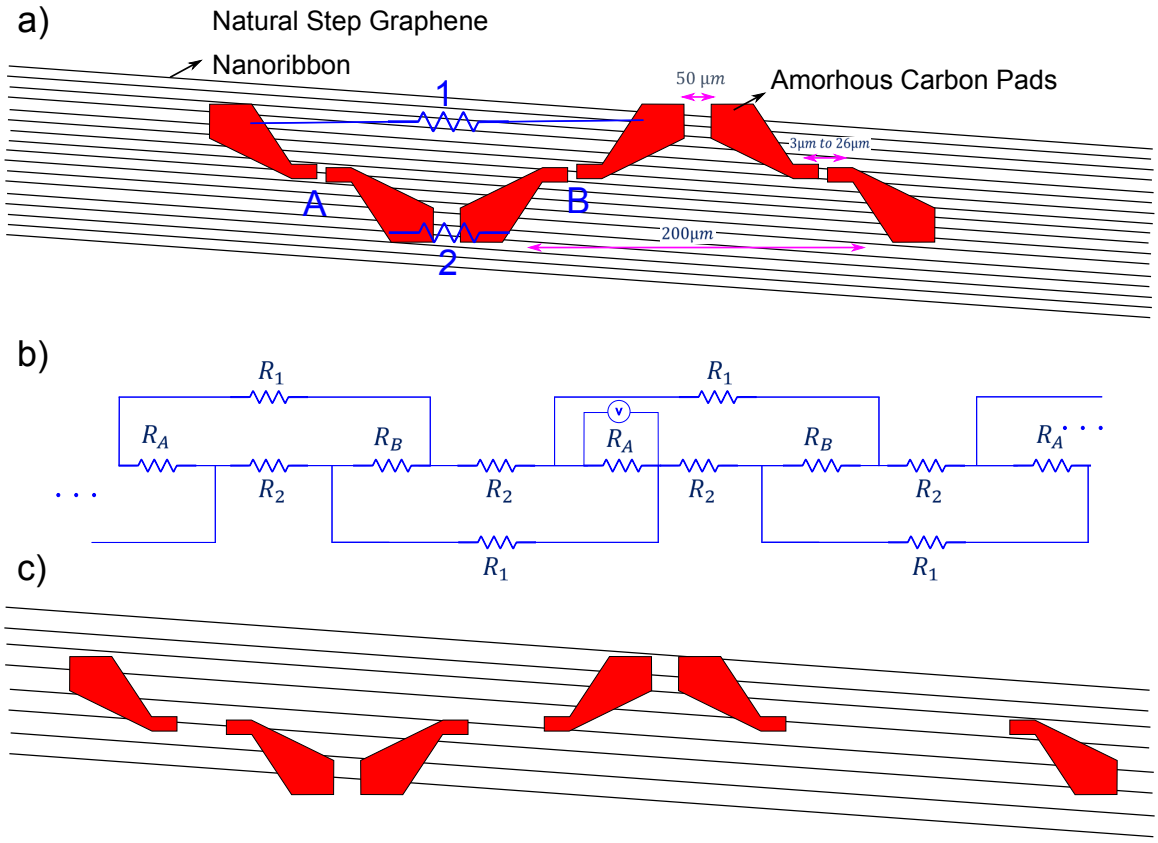

Figure 4.4: The distribution of natural step SWGNRs and contact pads on a chip. a) A unit cell of the photo-mask. Two adjacent contact pairs (R_A and R_B) are connected with a large resistance R_1 and R_2. The distance between two contact pairs is relatively long ($200\mu m$) which results in the high resistance. b) The equivalent resistor network for a series of contacts and ribbons. c) An exaggerated image of contact pad distances. After a certain distance between the pads, the chance of connecting a single ribbon from one to another decreases. For the two pairs on the left, a single ribbon connects the pads. For the two pads on the most right a single ribbon misses the shortest distance between the pads, therefore causing a larger resistance.

Mean free paths on the order of $10\mu m$ can be consistently obtained from transport measurements, this value can go higher for exceptional samples (Figure 4.3). Our measurements do not alone prove that the transport is through a single channel, but they are in line with previous results that have shown that epigraphene nanoribbons can host single channel ballistic transport [84].

Additional ribbon length vs resistance measurements are given in appendix (listed separately and not categorized along with the main thesis).

4.2 Contact Resistance and Surface Potentiometry

Beside the quantum resistance, the contact resistance to a contacted GNR comes from the lead resistance and the tunneling (interface) resistance (Figure 1.8). Normally the TLM can be used to identify the contact resistance, but the method assumes all the R_c to be the same. Also the local doping from the contacts can extend to $\approx 10nm$. In order to understand the conduction in the vicinity of contacts and to identify the contact resistance, a point probe based surface potentiometry technique can be used. This approach can also eliminate the interference of voltage probing contacts with the GNRs.

The surface potentiometry in this experiment is performed by utilizing a contact mode AFM scan with a lock-in based resistance measurement technique. Normally the resistance of a nanoribbon can be measured by applying a modulated constant current through two leads while measuring the voltage from another pair of contacts. The voltage measuring probes can be replaced with a contact mode AFM tip and this setup can work as a three point measurement system, where the low voltage end of the voltage measurement is shared with the current out lead as shown in Figure 4.5.

The AFM system by Park enables measuring voltages through a metal coated contact mode AFM tip. The details of such a setup are given in Figure 4.5. The first lock-in monitors the two point nanoribbon resistance while the second lock-in, which is phase locked to the first one, maps the potential on the surface as the AFM system scans a region.

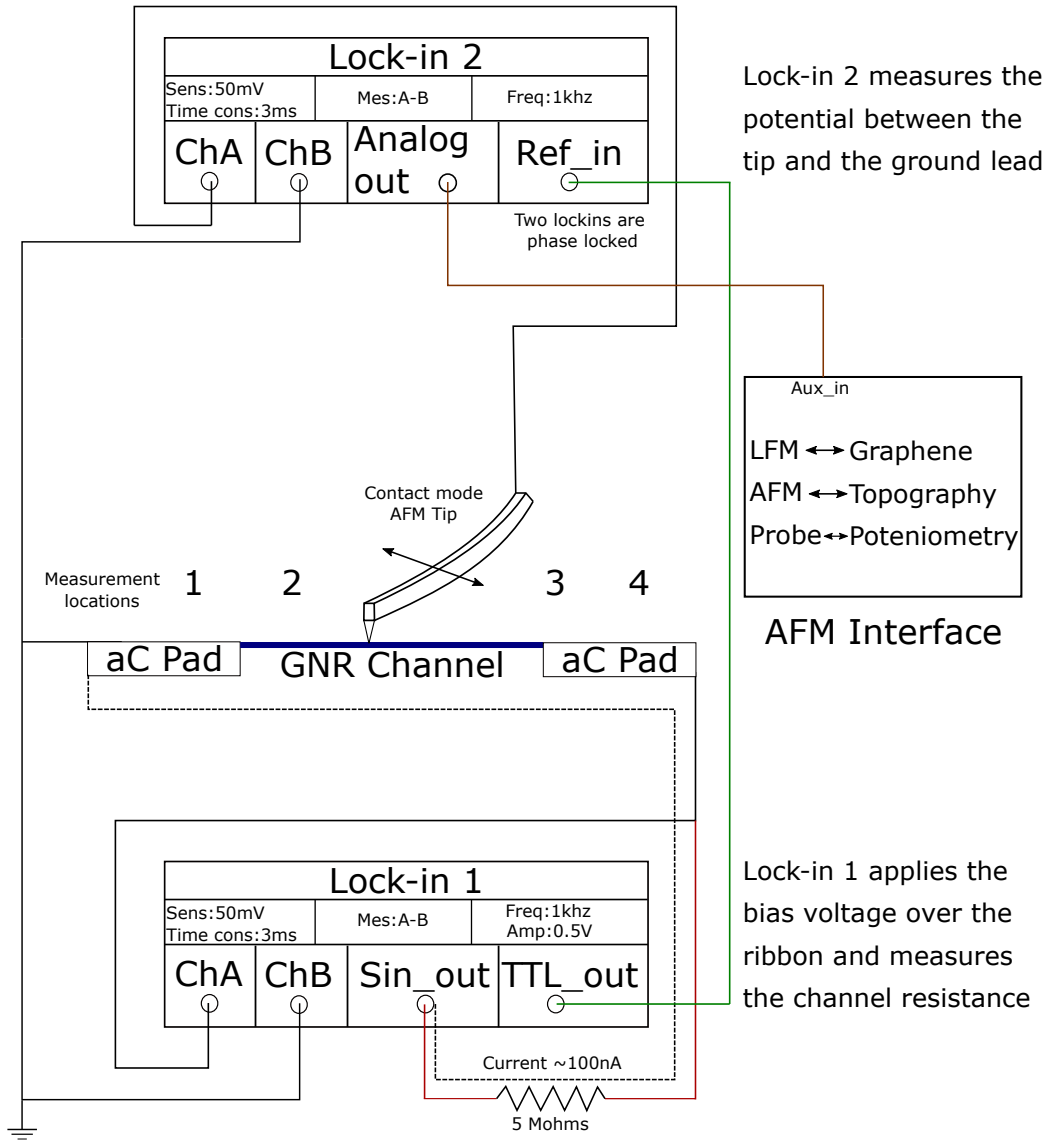

Figure 4.5: The conductive probe measurement setup. AFM in contact mode can be used with a metal coated tip to map the surface potentiometry on a biased sample. Along with the AFM and LFM data the potentiometry on the surface can be used to identify contributions of individual GNRs to the conduction. Two phase locked lock-ins can be used for this measurement. A $5M\Omega$ resistance is in series with the nanoribbon, which is on the order of $100k\Omega$, so the power supply works as a constant current source. The details of the setup and the parameters are given in appendix. The measurements 1, 2, 3 and 4 can be used to identify the contact resistances (Detailed in Figure 4.11).

The parameters for the AFM scan and the lock-in settings are given in appendix along with the explanations of further details about the setup.

As discussed in the graphene growth chapter, the conventional SWGNRs contain sidearms that create complex ribbon morphologies. Figure 4.6 (a) shows the LFM scan. Figure 4.6 (b) shows the corresponding potential map on the surface as 100 nA constant current is applied through the pads (that appear on the right and left). It can be seen that not all the sidearms interact with the SWGNR but some attached sidearms can cause shorts and create scattering centers. In order to evaluate these statements, another contacted nanoribbon structure that is free of sidearms was built for comparison (Figure 4.7).

Figure 4.6 (c) shows the voltage line profile along the ribbon. This profile is presented to show how sidearms affect the mean free path of the ribbon. The slopes change at certain points as indicated by the vertical blue lines, but remarkably, the slope change is mainly due to few short circuiting sidearms. We see that sidearms have otherwise very little effect on transport and a jump in voltage as expected for an invasive contact is not observed. If the attached sidearms acted like invasive probes, then they would add a total NxR_o to the resistance (N here is the number of sidearms).

Natural steps can have SWGNRs that are free of sidearms, but they come at the cost of having dense SWGNR arrays. Figure 4.7 (a) shows the LFM scan of a contacted natural step ribbon. The SiC chip is first pre-annealed to obtain natural steps and the SWGNRs are grown on them as explained in the graphene growth chapter.

SWGNRs grown on pre-annealed natural steps can get as narrow as 20 nm. This is mainly due to the presence of small steps ($10nm$ or less) hosting GNRs. Natural step SWGNRs do not preserve their width uniformly over long lengths and discontinuities can be observed. Narrow ribbons also have the problem of not contacting well to the aC contacts. Due to the poor contact, many of the natural GNRs that connect the two pads in the AFM image (Figures 4.7 and 4.8) don't make electrical contact to both pads. They may just act as equipotentials, if they are only connected to one pad. The possibility of making

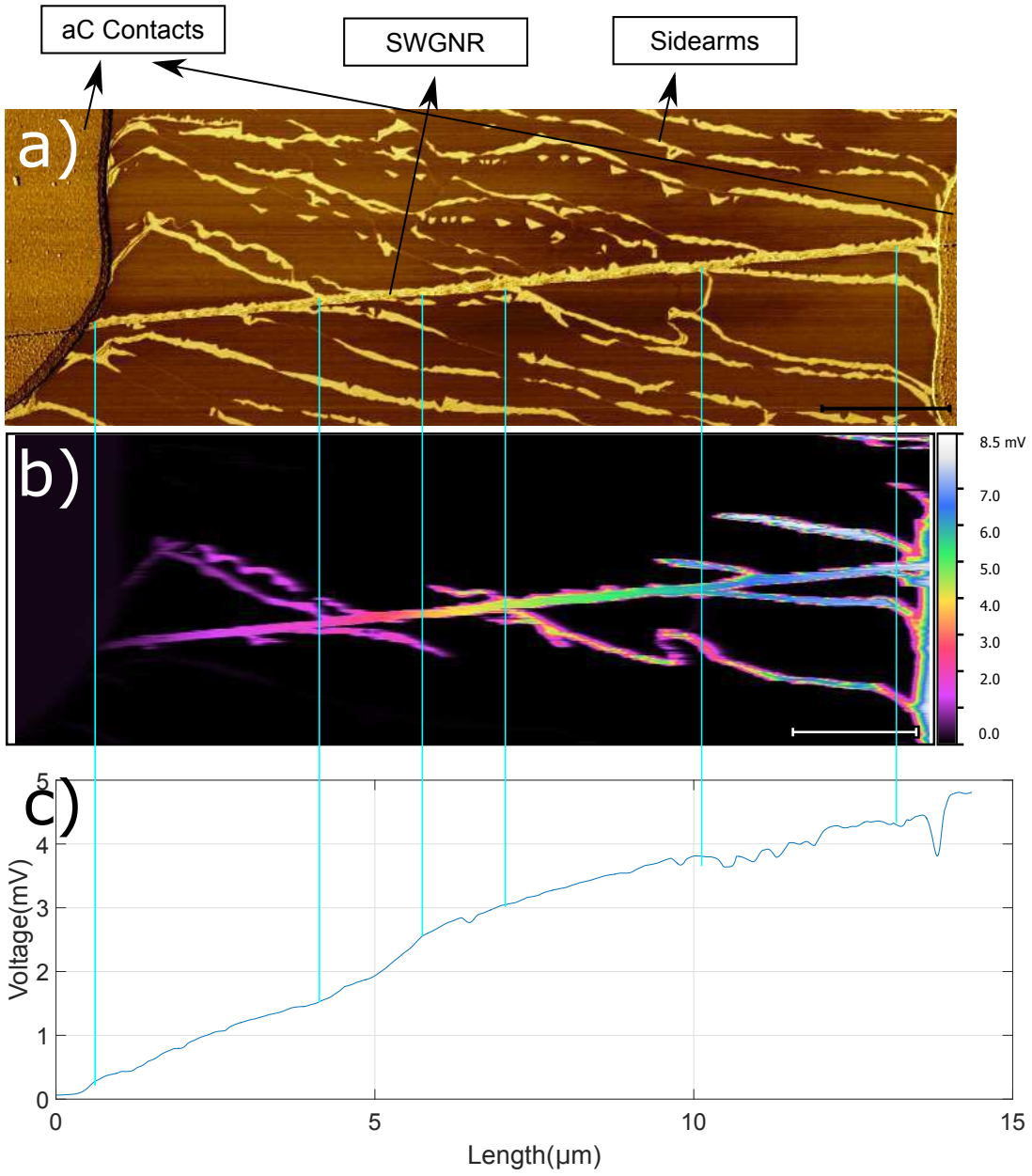

Figure 4.6: (a)LFM image of an SWGNR with aC leads. Dense sidearm formations that are attached to the main SWGNR are visible. (b) Surface potentiometry that is obtained with the conductive probe scanning method outlined in Figure 4.5. The potentiometry data can be mapped to the LFM data to identify which ribbon formations are involved in the conduction. (c) The corresponding voltage profile along the ribbon to see the effect of sidearms on the voltage distribution of the ribbon. The measurement can also be used to find the contact resistances and the mean free path of the main SWGNR. The scale bars are $2\mu m$ long.

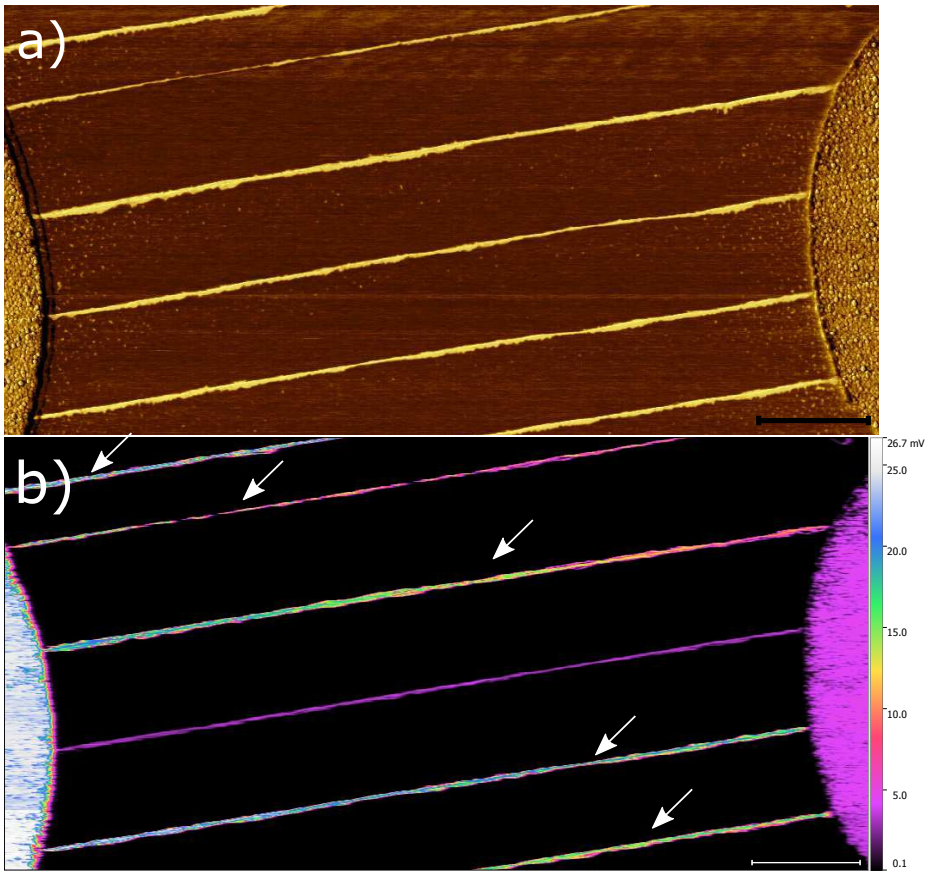

Figure 4.7: (a)LFM image of a natural step SWGNR with aC leads. Dense nanoribbon arrays connect the pads in multiple points. (b) Surface potentiometry of the same nanoribbon. Color gradients can tell which ribbons are attached to both of the contacts. The scale bars are $2\mu m$ long.

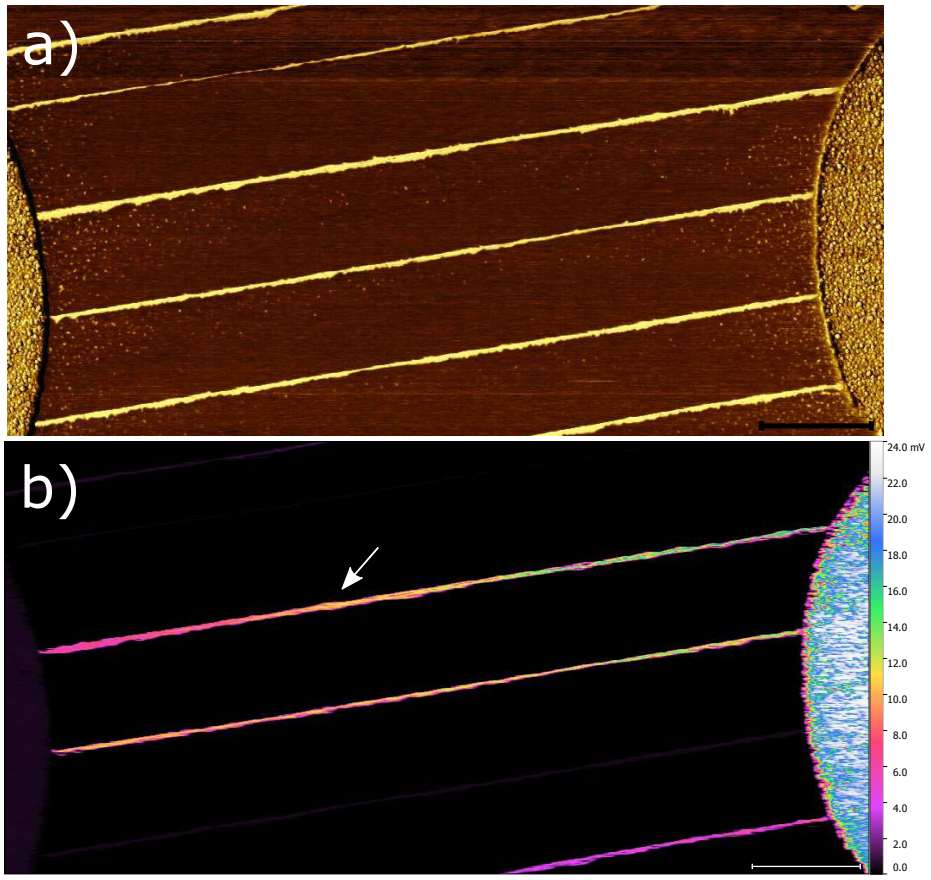

Figure 4.8: (a)LFM image of the same natural step SWGNR in Figure 4.7. (b) Surface potentiometry of the nanoribbon and its contacts. The current is switched to the opposite direction so the contrast similar to Figure 4.7 (b) can be obtained. The comparison of both figures enables us to identify which nanoribbons are attached to both of the pads. The scale bars are $2\mu m$ long.

good contacts to both pads is low due to the narrow ribbon geometry.

In order to understand which natural step ribbon is connected to which pad in Figure 4.7, the bias voltage can be flipped (Figure 4.8) and both cases can be compared.

A ribbon that is attached to only one pad has a constant voltage value on it, since no current flows through it. It simply acts like an equipotential line and preserves the voltage of the only pad that it is connected to. If the ribbon has a color gradient on it, it means that it is connected to both of pads and it enables current flow through it. This procedure has also been tested for the SWGNR shown in Figure 4.6, but it is already obvious from the color gradient in Figure 4.6 that the nanoribbon is continuous and it merges into both of the

contacts.

Flipping the bias of the nanoribbon shown in Figure 4.7 shows that only one of the five nanoribbons (marked with arrows in Figure 4.7) that were bright in in Figure 4.7 is also bright in Figure 4.8. Looking at the topography of the same regions shows that this step is also the tallest structure and so it hosts the widest SWGNR ($15nm$ tall and $60nm$ wide with a 14° facet angle at the steepest point). Both potentiometry results are separately plotted together for comparison in Figure 4.9 and the only contacting ribbon is marked with an arrow.

Since the current amplitude is known from the circuit given in Figure 4.5 ($100nA$) and is the same through the nanoribbons, a voltage measurement can also reveal the resistance of the nanoribbons. Figure 4.10 shows the line profile taken on the ribbon. The jumps at the ends correspond to the tunneling resistances may be related to the contact-nanoribbon interface.

Mean free paths can be obtained from the line profiles given in Figure 4.10. By using the approximation $\frac{\Delta L}{\Delta R/R_o}$, mean free paths of $4.4\mu m$ and $4.3\mu m$ can be obtained for SWGNRs and natural step nanoribbons respectively. However an analysis of the number of active channels needs to be made to validate this calculation.

The contact resistance overall consists of the lead (R_{lead}) and the interface resistances ($R_{interface}$). R_{lead} is a result of the resistivity of the lead material and the design of the contact. $R_{interface}$ is a result of the interface effects.

By looking at the cross-section of the graphene/contact potentiometry interfaces individual interface and lead resistances can be obtained. Figure 4.5 shows points marked as 1,2,3,4 on the nanoribbon and its contacts, voltage profiles between points 1-2 and 3-4 are extracted to find the resistances at these points.

In Figures 4.12 and 4.13, the cross sectional voltage profiles are presented. In Figures 4.12 (left) the voltage profile in the vicinity of the left contact is shown. The voltage values measured at the left and right of the contact interface (right below 0.2mV and 0.9

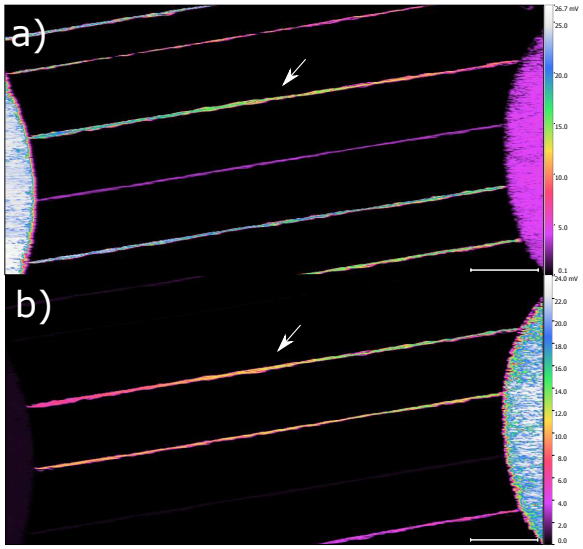

Figure 4.9: Combined potentiometry images from Figure 4.7 (a) and Figure 4.8 (b). The only ribbon that makes contacts to both pads is marked. The scale bars are $2\mu m$ long.

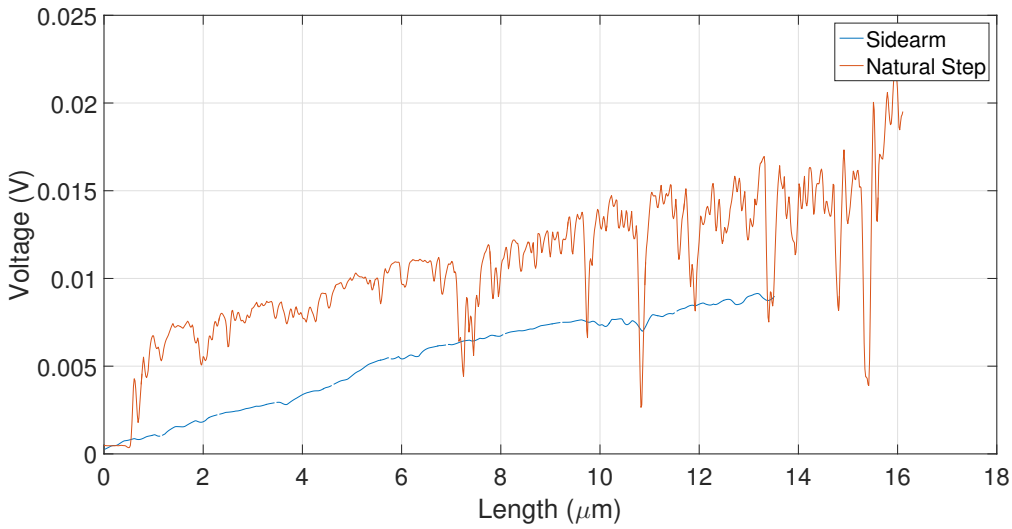

Figure 4.10: The voltage difference between the contacts are slightly higher for the natural step case due to the whole system having a higher resistance. this mainly stems from tunneling resistance which can be seen as a potential jump at contacts for the natural step ribbons at $0.4\mu m$ and $15.5\mu m$. Also the nanoribbon is narrower compared to the same amount of current is run through both nanoribbons (100 nA). for the case of Natural steps the contact resistance is higher on both ends, the jumps at $0.8\mu m$ and $15.5\mu m$ are due to contact resistances. The contact resistance for the natural step is smaller due to the SWGNR being wider.

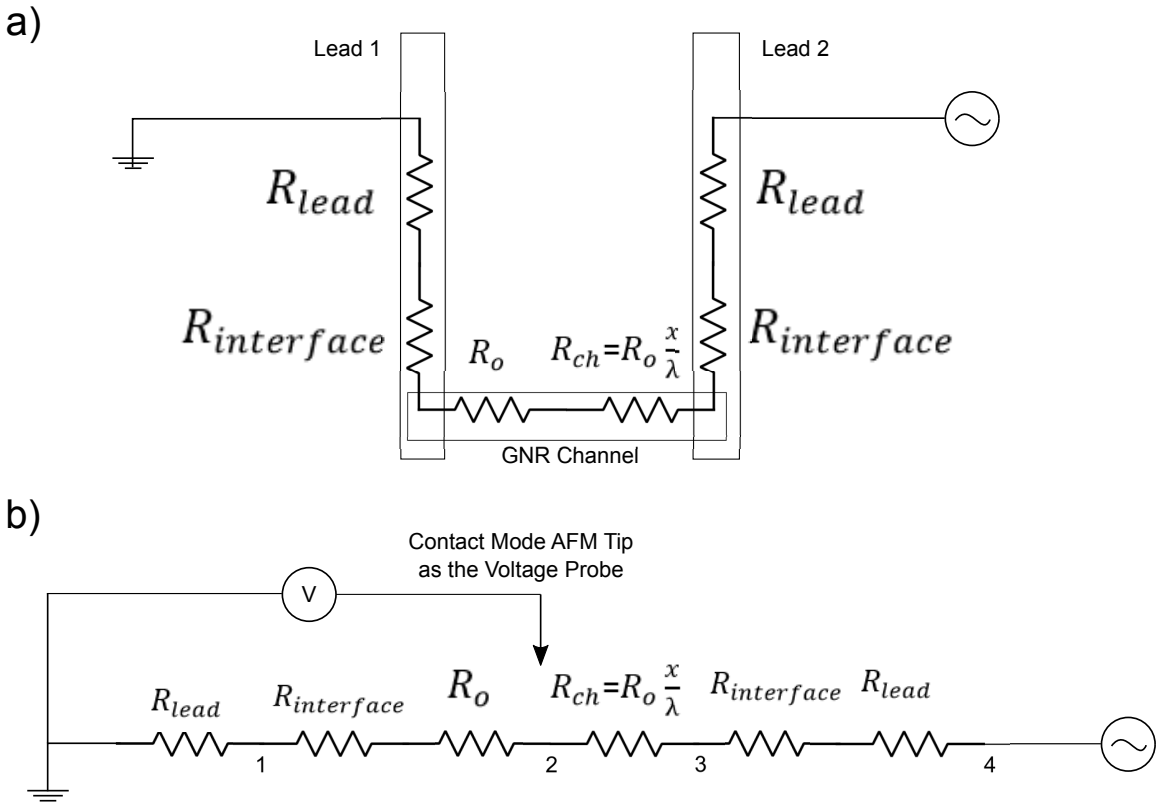

Figure 4.11: (a) The equivalent circuit of a two point GNR with a single channel. (b) The schematic of a conductive probe spectroscopy. Resistances from the labeled points (1-2-3-4) to the left can be measured and the corresponding variables between the points can be identified. λ in the drawings represents the long length mean free path Λ_{max}.

mv) are given and they can be used to identify resistances at points labeled as 1 and 2 in Figure 4.11. The plateau on the left (Figures 4.12 (left)), below 0.2mV, gives us the voltage measurement at point 1 shown in Figure 4.11 (b), which can help us to find R_{lead}. The plateau on the right of the same figure corresponds to the voltage measurement at point 2 in Figure 4.11 (b). This gives us $R_{lead} + R_{interface} + \alpha R_o$. R_{lead} can be read as $1.2k\Omega$ which is low since the aC sheet resistance is on the order of $1k\Omega/\Box$ (Figure 2.9). From the voltage reading on the right of the same plot, $R_{lead} + R_{interface} + \alpha R_o = 8.8k\Omega$, which gives $R_{interface} + \alpha R_o = 7.6k\Omega$. This means even for the case of $R_{interface} = 0$, $\alpha R_o = 7.6k\Omega$ indicating that there are at least four channels are involved in the transport since $R_{interface} + R_o/N = 7.6k\Omega$ should be considered, which gives $N > 3.2$.

The right plot in Figure 4.12 shows the voltage profile in the vicinity of the left contact (of the ribbon given in Figure 4.6). The profile can be used to identify resistances labeled as 3 and 4 in Figure 4.11. From the readings of 8.8 mV and 9.6 mV it can be concluded that $R_{lead}+R_{interface}+R_{channel}+R_o/N = 88k\Omega$ and $2R_{lead}+2R_{interface}+R_{channel}+R_o/N = 96k\Omega$, which gives $R_{channel} = 79.2k\Omega$. By using $R_{channel}$, and taking N as 4, the average mean free path can be calculated as $\frac{\Delta L}{N\Delta R/R_o} = 13.5\mu m/(4x79.2k\Omega/25.8k\Omega) = 1.1\mu m$. Note that this is a minimum value. If there are 4 channels, then from previous measurement, we assume only 2 modes have a long mean free path, then the mean free path of these channels is twice as long.

In the case of the natural step nanoribbon, Figure 4.13 can be used. Following a similar calculation to the SWGNR for the natural step ribbons give $R_{lead} = 5k\Omega$ and $R_{lead} + R_{interface} + \alpha R_o = 70k\Omega$, so $R_{interface} + R_o/N = 65k\Omega$ (α is taken as $1/N$). This means that if $R_{interface}$ is low, we may have a single channel transport. However, the narrow ribbon width might result in high $R_{interface}$ as well. The right side of the same voltage profile gives $R_{lead}+R_{interface}+R_{channel}+R_o/N = 160k\Omega$, so $R_{channel} = 90k\Omega$ if $N = 1$. The last measurement on the right lead gives $2R_{lead} + 2R_{interface} + R_{channel} + R_o/N = 200k\Omega$, which gives (for $N = 1$) $R_{interface} = 40k\Omega$. Since $R_{interface} + R_o/N = 65k\Omega$

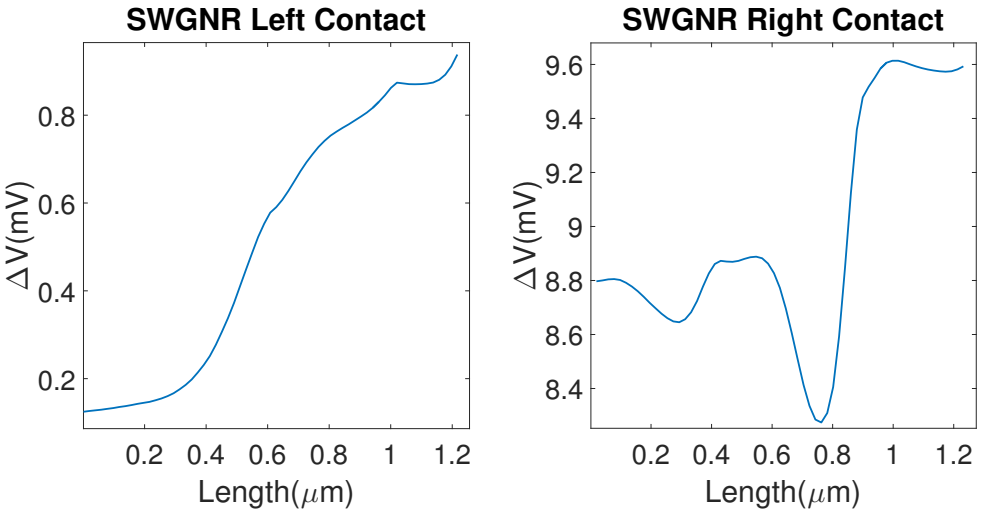

Figure 4.12: Line profiles of surface potentiometries in the contact area for the sidearm ribbon (Figure 4.6). These measurements can be used to identify R_{lead} and $R_{channel}$ separately. Left: The voltage profile of the in the vicinity of the left contact. The voltage values measured at the left and right of the contact interface (at 0.1mV and 0.9 mv) can be used to identify resistances labeled as 1 and 2 in Figure 4.11. Right: Similarly to the resistances labeled as 3 and 4 in Figure 4.11 can be identified.

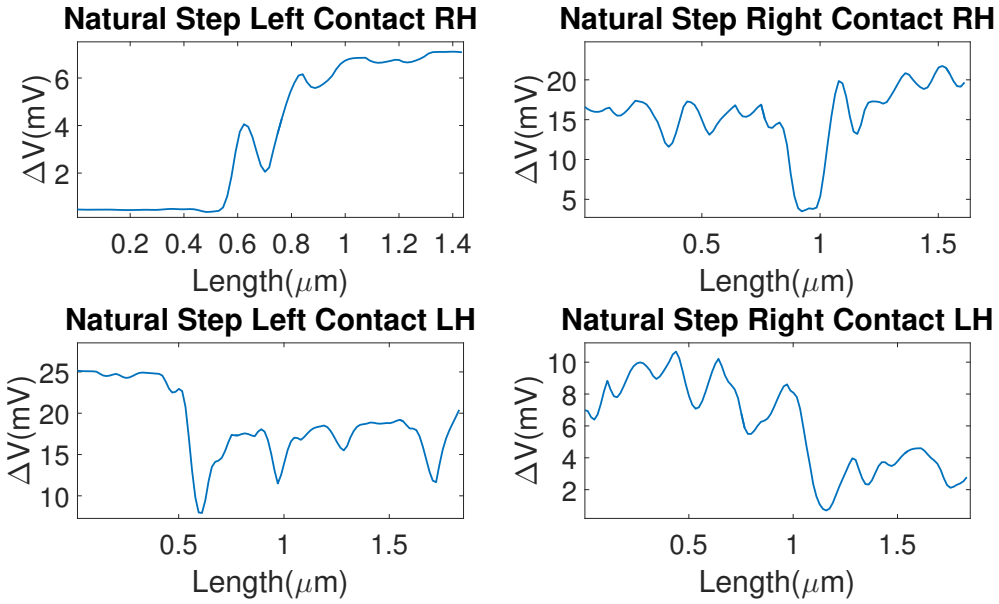

Figure 4.13: Line profiles of surface potentiometries in the vicinity of the contact interfaces of potentiometries given in Figures 4.7 and 4.8. The high voltage end is on the right contact for the top plots and at the left contact for the bottom plots. Similarly to Figure 4.12, top left plot gives voltage values measured at the left and right of the contact interface which can be used to identify resistances labeled as 1 and 2 in Figure 4.11 and top right plot gives the resistances labeled as 3 and 4 in Figure 4.11. The same calculation can be made for the other two profiles.

is found from the first measurement, we get $R_o/N = 25k\Omega$, which justifies the estimation $N \approx 1$. Following the same calculation from the left side gives a similar result. The mean free path that can be obtained from this $R_{channel}$ is $15\mu m/(90k\Omega/25.8k\Omega) = 4.3\mu m$, considering a single channel transport. Even though both nanoribbons have mean free paths in the ballistic range, the mean free path of the natural step SWGNR is found to be nearly four times higher than the average (i.e. minimum) $1.1\mu m$ of the SWGNR after the correction coming from the number of channels. This means that single channel ballistic transport can be obtained by improving the morphological confinement of the graphene ribbon and the mean free path can go from $\approx 1.1\mu m$ to $4.3\mu m$ as calculated above.

Conventionally tight binding calculations of narrow ribbons with different chiralities show the dependence of the conduction on the edge termination [51, 52]. Even though the edge termination of SWGNRs are shown to be aligned with the step direction on SiC [84],

no dependence of the the ribbon conduction on the edge termination have been observed in the course of this thesis. In agreement with previous measurements [83], the minimum width of the ribbons investigated was on the order of 40 nm. This might be too wide to see the edge effect on the transport. The width limit where the bandgap for AC ribbons is predicted [52] to be on the order of 12-13 atoms. But the ribbon edge length doesn't seem to affect the transport as much as it should if it were a relevant parameter.

One important difference in ribbon morphologies between Figure 4.6 and Figure 4.7 is the length of the edges. For the same bulk lengths, the edge lengths are quite different due to the sidearm formations that extends the edges. One dimensional transport nature [84] of the GNRs indicate that the transport might be carried over the edges of graphene. However, our measurement show two ribbon cases, where the nanoribbon length is the same but, the edge length is significantly different, yet they both give mean free paths in the ballistic regime (Figure 4.10). The negligence to the edge disorder in the surface potentiometry (Figure 4.6 and Figure 4.7) shows that the transport phenomena is not localized to the edge, but this may also be related to the SWGNR ribbon having more ribbons involved in the conduction.

Conductive probe measurements are performed at room temperature in air. Therefore, the resistance values compared to Figure 4.3 is relatively higher. The contact problem of natural steps discussed in the last part of the mean free path measurements can be seen in the conductive probe measurements of natural step ribbons (Figure 4.9).

4.3 Temperature Dependence

Temperature dependence measurements are performed in a CryoIndustry cryocooler. The setup has the ability to go from 420 K to 1.6 K and fields up to 9T are possible. Temperatures above 300 K are mostly used for cleaning purposes before the main measurement.

The effect residues that come from the nano-fabrication and air exposure can be lowered from the sample by annealing it in vacuum. In Figure 4.14 six aC contacted ribbons

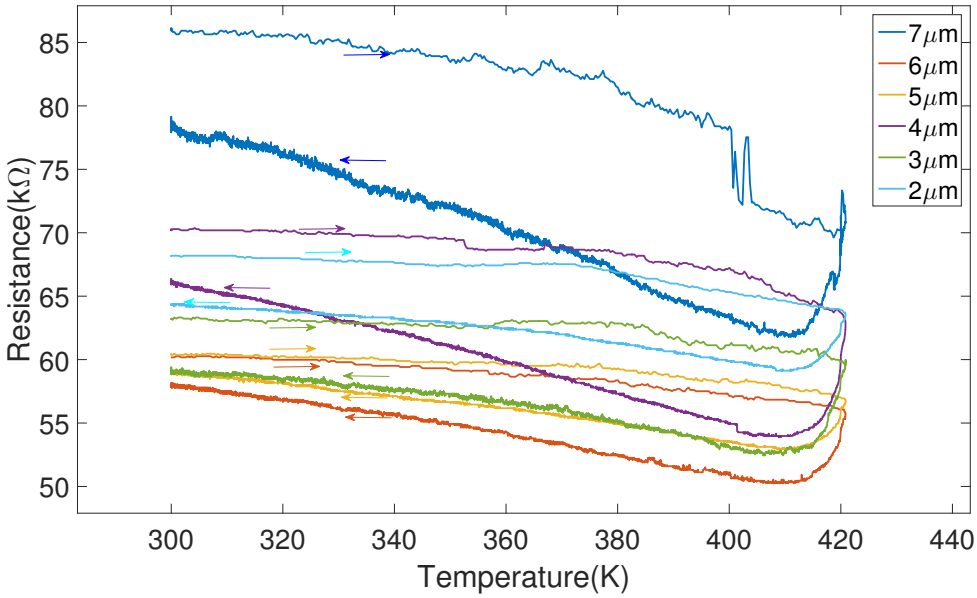

Figure 4.14: Temperature vs resistance (two point) profile of six aC contacted SWGNRs as they are annealed in vacuum inside the cryostat chamber. Ribbon lengths range from $2\mu m$ to $7\mu m$ starting from the least resistive to the most resistive nanoribbon. The first annealing of a sample generally decreases the resistance nearly by 10% as the samples cool back to the room temperature. Heating and cooling rates are $1°C/min$.

with lengths from $2\mu m$ to $7\mu m$ are annealed in vacuum up to 420 K in the cryostat. The resistances drop nearly by 10% as the samples cool back to 300 K. This drop in resistance is attributed to cleaning / degassing the GNRs. The samples can be heated up to higher temperatures multiple times till the resistance no longer decreases, which does not happen unless the samples are heated above $300°C$. The saturation indicates that the degassing of residues is completed. The higher annealing temperatures can be obtained in the vacuum probe station.

Higher temperature measurements are made in the vacuum probe station where the temperature can be raised up to $400°C$ and the cleaning effect can be observed along with high temperature characteristics of the nanoribbon. Since the two effects are occurring simultaneously, first, the samples are heated for cleaning. After the cool down, the resistance value is generally lower than the initial one (like in Figure 4.14). Second, the sample is heated again and the high temperature characteristics are observed. If the resistance value remains

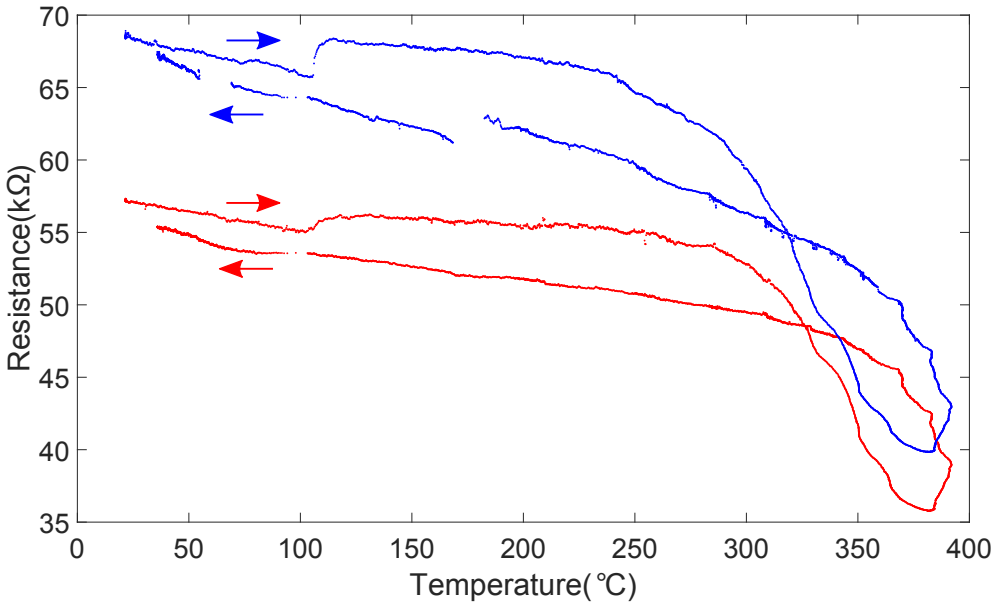

Figure 4.15: Temperature dependent two point resistance measurements of two aC contacted SWGNRs (300 nm (red) and 400 nm long (blue), the shorter one with the lower resistance) as they are annealed in the vacuum probe chamber for the second time. The initial resistance is recovered, which means that the degassing phase is over. The geometries can be seen from Figure 3.23 (c)-(d). The temperature rate was not controlled which may be the reason behind the differences in the traces.

the same after the cool down then it can be concluded that the degassing phase is complete and the observed temperature dependence is an intrinsic feature of the nanoribbon.

Figure 4.16 shows the resistance vs temperature plots of ribbons with aC and metal (Au/Pd) contacts. aC contacted nanoribbons are fabricated in two and four point setups. The resulting increase in the resistance of short aC contacted nanoribbons is a combined effect of both the contact resistance and nanoribbon properties.

The sheet resistance of aC increases upon cooling (Figure 2.9). Therefore, it is expected to have an increase in the overall resistance as aC contacted nanoribbons are cooled. However, all the nanoribbons shown in Figure 4.16 (a) are aC contacted and the resistance increases only for the short nanoribbons ($< 450nm$).

Figure 4.16 (b) shows four point measurements for a metal contacted nanoribbon. Unlike the aC contacted nanoribbons, the three shortest nanoribbons ($300nm$, $400nm$ and $600nm$) are the ones that are the least affected from the temperature change.

The trade off between the two methods is that aC contacted nanoribbons are high temperature compatible and can be annealed at $1000°C$, which means degassing (cleaning) can be done at a greater magnitude. However, as shown in Figure 4.16 two point aC contacted short GNRs have additional resistance increase at low temperatures. Metal contacts are not high temperature compatible, which prevents them from being heated up to higher temperatures that aC nanoribbons can be heated up to. Especially Au contacts are known to form beads that diffuse along the GNR above certain temperatures.

During the fabrication of aC nanoribbons, the contacts are either deposited before the graphene growth and they are exposed to graphene growth temperatures ($\approx 1550°C$) or they are deposited after the growth and the whole setup is annealed at $1000°C$. This temperature is high enough to lower the resistance of aC material through the formation of nano-crystals inside the amorphous structure of aC, but it may not be enough to create a robust contact to graphene. Interface effects between graphene and aC contacts might play a role in the high resistance as well.

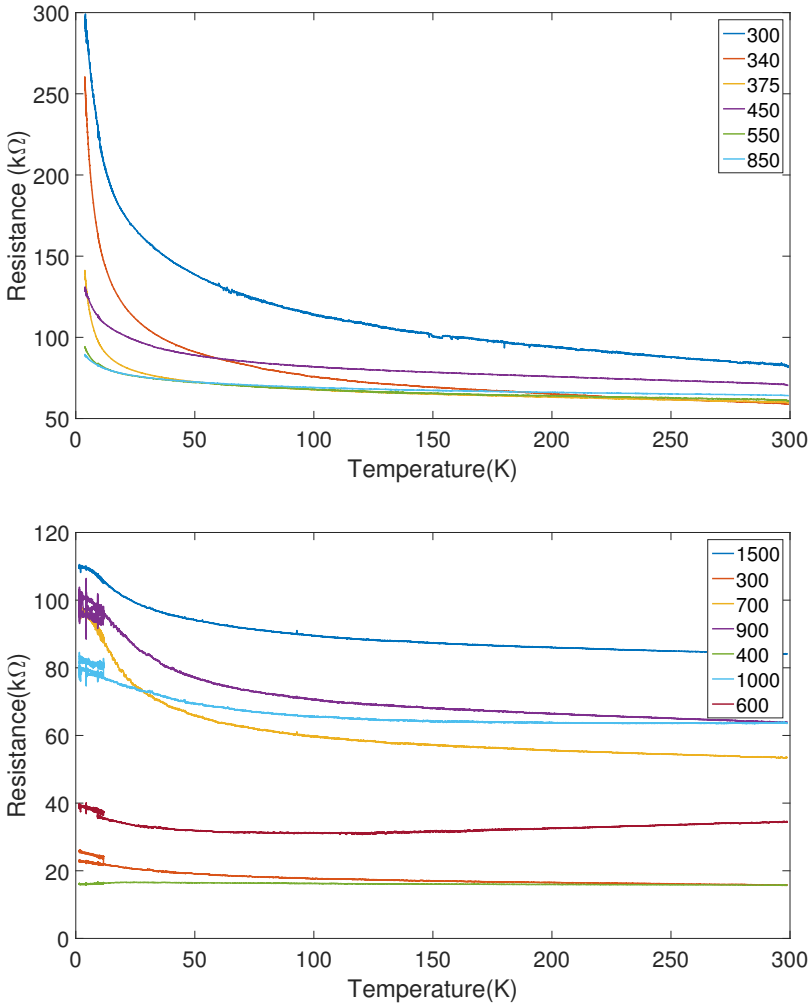

Figure 4.16: (a) Two point measurements of six aC contacted nanoribbons from Figure 3.23. The increase in resistance is a combined result that comes from aC contacts and the short GNRs. (b) Four point resistance vs temperature measurements of metal (Au/Pd) contacted ribbons. The geometry is similar to the one given in Figure 2.5.

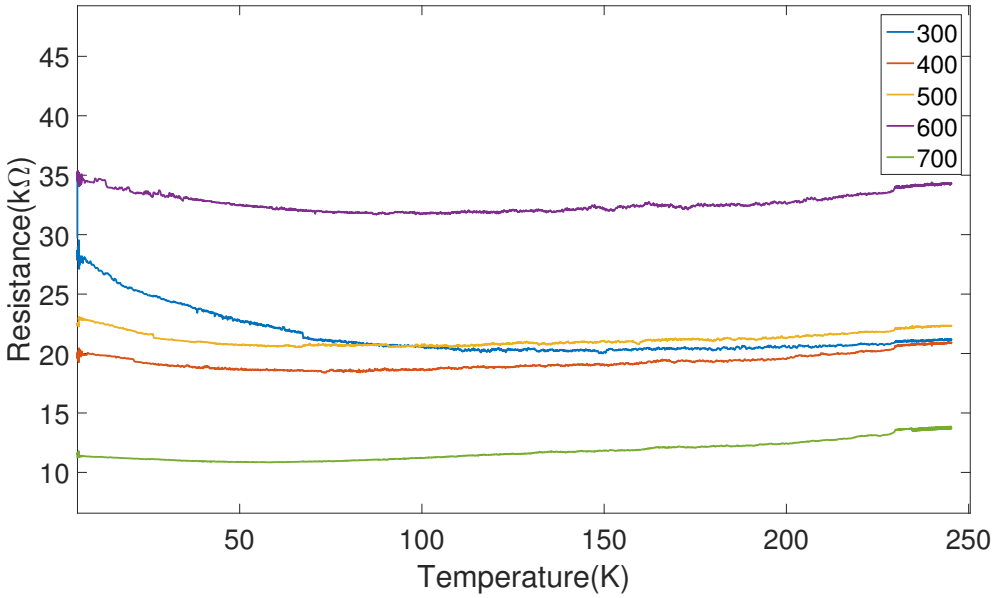

Figure 4.17: Another set of four point resistance vs temperature measurements of metal contacted graphene ribbons with lengths ranging from 300 nm to 600nm. SWGNRs are grown with the combined etching and annealing technique (Figure 3.19). For the values below $25k\Omega$ multi-channel transport is possible. The geometry is similar to the one given in Figure 2.5.

The temperature dependent measurements done on nanoribbons that are more confined (similar widths $\approx$ $100nm$, but higher morphological confinement to the sidewall, Figure 3.19) are given in Figure 4.17. The resistance has an unusual and relatively consistent temperature dependence.

CHAPTER 5
CONCLUSION

Epigraphene on SiC offers the graphene crystal on an insulating substrate. Its one dimensional counterpart SWGNRs can be grown with high scalability on the same platform. SWGNRs exhibit exceptional transport features in UHV conditions. In order to utilize these features into contacted graphene nanoribbons and harvest their benefits, a new fabrication method needs to be developed for the material. In this thesis we report epitaxial GNRs (with contacts fabricated on them) that perform in the ballistic regime with mean free paths on the order of $10\mu m$ at room temperature.

The fabrication process flow that leads to ballistic GNRs with contacts is presented. The fabrication starts with the consistent confined SWGNR growth method that is obtained in several ways. First the conventional SWGNR methods are investigated, then the natural steps of the SiC crystal are utilized for ribbon formation through an annealing technique. Finally the annealing technique is combined with the conventional SWGNR growth to obtain confined ribbons.

A lift off technique for amorphous carbon contacts are developed to prevent the conventional etching of amorphous carbon contacts. With the new contact fabrication method, on the order of fifty nanoribbons with different lengths are produced on separate chips to investigate the ballistic transport. Mean free paths on the order of $10\mu m$ are obtained in a vacuum probe measurement setup that is built for this experiment.

Conductive probe measurements are used to analyze the effect of the edge morphology on the transport. For two ribbons with same lengths but extremely different edge formations, it is shown that mean free paths can be improved four times from $1.1\mu m$ to $4.3\mu m$. Similarly, the number of channels involved in the transport can go from four to one upon increased morphological containment. This means by accommodating improved morpho-

logical confinement of SWGNRs, we were able to increase quantum confinement of our nanoribbons and obtain increased mean free paths.

Overall arrays of contacted epigraphene nanoribbons that perform in the ballistic regime at room temperature are fabricated. The exceptional room temperature ballistic transport feature of epigraphene nanoribbons now can be further analyzed with contacts while preserving the ballistic transport properties.

Appendices

APPENDIX A
LITHOGRAPHY TECHNIQUES

Lithography is the process process of masking a sample for a follow up deposition or etching step. A shadow mask (which maybe ideal for the case of graphene) can be placed on the sample and the process can be carried over it for large scale features. However, due to its practicality and due to challenges of making a hard mask and preserving it on the sample, polymer based lithography techniques are mainly used in the fabrication of electronics. In this technology, first the surface is coated with an organic photoresist with a spin coater. The sample is placed on a rotating platform and high rotational speeds (1000 rpm to 5000 rpm) are applied on order of a minute. This results in micron thick uniform resist profiles over the sample. Baking the sample at temperatures on the order of $100\,^{\circ}C$ for a minute dries the resist over the surface and increases its durability. An adhesion promoter might be needed before the spin coat to make sure that the resist sticks on the surface.

The way photoresists are used in creating patterns is as follows: Due to their chemical properties, once exposed to a certain UV spectrum line (for photoresists) or to an electron beam (E beam resists) resists change their solubility [138] in solvents (developers). Resists can work the opposite way, where they can be initially insoluble and their solubility can be recovered once they are exposed. This defines the negative or the positive photoresists, their polarity. The control over the solubility feature can be utilized to create patterns if the exposure can be confined to areas of interest. Once partially exposed, the sample can be put into a developer solution for selective cleaning of certain areas. After doing the actual fabrication step in these areas (etching or depositing) a hard remover, like acetone, can be used to clean all polymers. The leftover areas end up having the shape of the exposure pattern. The selective exposure is done with a hard mask (typically chromium on quartz) for photolithography or with directed and controlled e beam exposure via an SEM, a beam

blanker and a controlling software.

The precision of photolithography depends on the mask aligner and the mask feature size. Features obtained with photolithography, contrary to its industrial versions that reach down to nanometers, is on the order of a micrometer. It produces quick patterns for large scales; but alignment, feature size, and design flexibility are limited by the mask aligner, the mask production limits (The minimum feature size the mask supplier can produce on your mask) and the mask availability (every new pattern needs a new mask). Once the pattern is selected, it can be obtained with either positive or negative photo-resists.

Negative resists develop patterns in areas that are not exposed to the UV light source, and positive works the opposite way. SC1813 from Micro Chem is used as the positive photo resist and NR9 from Futurrex is used as negative resist. Both resists are designed for the 365 nm wavelength line and both can be developed with MF 319 developer from Micro Chem. Different spin coat recipes can be chosen for different thickness of resists. 1 to 2 μm thicknesses can be obtained by spin coating at 4000 rpm for one minute. SC1813 needs to be heat treated at $180\ ^{\circ}C$ for one minute and NR9 at $115\ ^{\circ}C$ for one minute again. Exposed samples can be developed in MF 319 for 25 secs for SC1813 and 8 seconds for NR9. After the development, the samples should be rinsed with dionized water for at least 15 seconds.

Either negative or positive resist can be used for SWGNR mesa production. Mesas or trenches can be obtained from the same mask with different resists and they work the same way since the sidewall is the area of interest for SWGNR growth and the flat parts of the chip don't play a significant role.

SEM lithography is used with methyl methacrylate (MMA) and Poly(methyl methacrylate) (PMMA) (both from Micro Chem) bilayer resist combinations. PMMA and MMA are commercially available in different densities (conventionally called thickness). Spin coat recipes can change for different thicknesses of resists and suggested spin coat recipes can vary (most resists have short shelf life). A deformed resist can show up as bad liftoff or as

not so sharp resist profiles. Similar to changing the spin coat recipe, baking temperatures can be adjusted as well (for the case of bad liftoff or not lifting off resist after cleaning). After the application of e-beam on the spin coated samples with the use of JEOL JSM 5900 and the software NPGS by JC Nabity Lithography Systems, exposed samples are developed in 1:4 MIBK:IPA (Micro Chem developer) solution for 25 seconds. Developed patterns are rinsed with IPA for another 15 seconds. Feature sizes down to 100 nm can be achieved in this setup. With over exposure and shadow deposition methods this limit can be pushed to 50 nm.

After the development, UV ozone cleaner is used (if necessary) to remove suspected resist residues in the developed area. 1 minute UV exposure in a PSD-UV4 system (by Novascan) is applied on patterned samples.

The term SEM lithography is used rather than E-beam lithography because the term E-beam lithography is used for another advanced machinery (JEOL JBX 9300 FS) where the feature size can be much smaller (down to 5 nm) and the patterning is faster.

APPENDIX B

THE GROWTH FURNACE AND THE ANNEALING FURNACE

A definitive model of graphene growth on SiC can be challenging just like any other crystal growth modelling; but for the purposes of estimating and establishing the temperature ranges and the time periods that give monolayer graphene growth, some models can be tested.

Figure 3.3 shows the experimental setup and the variables involved with it. $R_{SiVapor}$ is the Si sublimation rate from SiC. This variable can be replaced with a constant, Si vapor pressure dependent value, but because of having the system in non-equilibrium, it is more convenient to have a rate variable rather than a static offset. This rate variable should be a function of the inner pressure(P_{in}) and the temperature(T). $R_{SiEscape}$ is the escape rate of the Si vapor from the system through the hole.

The problem of gas flowing through a constriction is similar to the Venturi effect and may even be an example of a Choked flow for high speed gas flow (which might be the case since the pressure difference is greater than the outside pressure at growth temperatures ($P_{in} - P_{out} >> P_{out}$)). This can be identified by looking at the Si vapor pressures at different temperatures.

The study by Lilov, SK [139] investigates Si vapor pressures over SiC at elevated temperatures ($1500°C$ to $3100°C$). The vapor pressure rises very quickly after $1500°C$ and low temperature and high temperature dependencies differ significantly. Figure B.1 shows that the vapor pressure can be proportional to $(T/T_o)^{19.5}$ ($T_o = 1960°C$) above T_o and $(T/T_o)^{28}$ below. This shows that around graphene growth temperatures the Si sublimation rate can increase drastically by small variations in the temperature. This especially shows the importance of having a confinement since it suppresses the Si sublimation.

In the case where the inner pressure is dominated by the Si sublimating from the SiC

Table B.1: The list of variables involved in the Confinement Controlled Sublimation method (Figure 3.3). $A_{SiWalls}$ has dimensions of pressure and the rate variables have dimensions of N/t (N=particle number).

Variables	Proportionality
$A_{SiWalls}$	Constant after t_o
$R_{SiVapor}$	$\propto T^{14}$
P_{in}	$A_{SiWalls} + \frac{\int (R_{SiVapor}(P_{in},T) - R_{SiEscape}) dt * R * T}{V}$
P_{out}	$10^{-6} mbar$
$R_{SiEscape}$	$R_{SiVapor}$

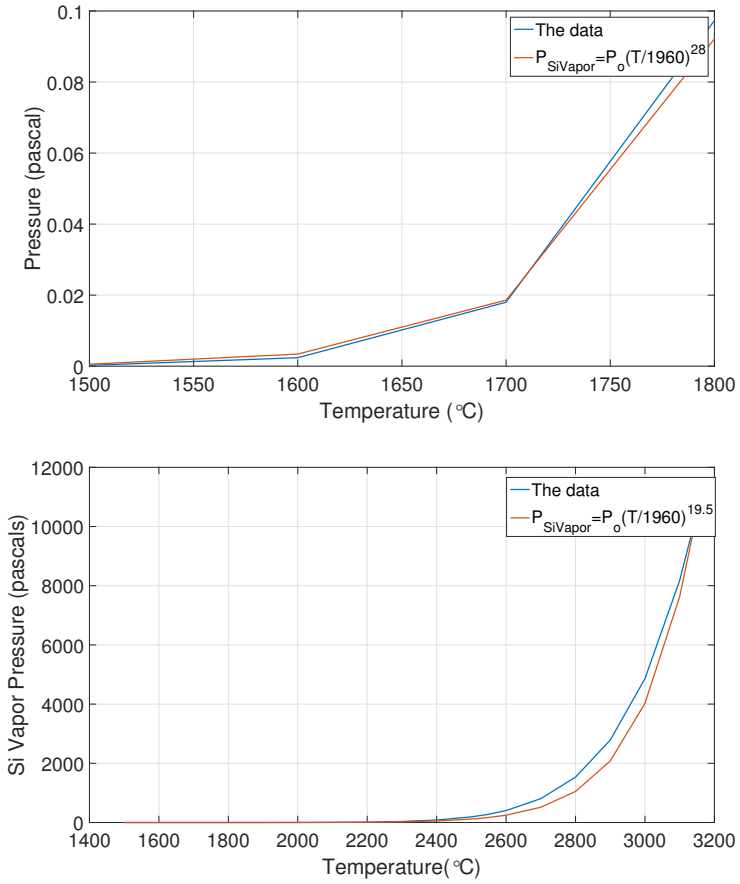

Figure B.1: Top: Low temperature dependence of Si vapor pressure. Bottom: Higher temperatures. P_o is 1 pascal. Data is taken from [139].

chip, $R_{SiEscape}$ can be assumed to be same as $R_{SiVapor}$.

The flow rate for the Venturi effect is given as:

$$R = A_1\sqrt{\frac{2}{\rho}\frac{(p_1 - p_2)}{(\frac{A_1}{A_2})^2 - 1}}, \tag{B.1}$$

Where R is the flow rate, ρ is the density of the gas, A_1 and A_2 are the cross sectional areas inside the crucible and the hole respectively. Since $P_{in} - P_{out} >> P_{out}$, the term $p_1 - p_2$ can be approximated to p_1. Also the approximation $(\frac{A_1}{A_2})^2 - 1 \approx (\frac{A_1}{A_2})^2$ can be made since $A_1 >> A_2$. The equation then becomes:

$$R \approx A_1\sqrt{\frac{2}{\rho}\frac{p_1}{(\frac{A_1}{A_2})^2}} = A_2\sqrt{\frac{2p_1}{\rho}}, \tag{B.2}$$

Assuming that the number of particles inside the crucible is constant instantaneously, using the ideal gas law one can replace the pressure term with $\frac{NRT}{V}$, which gives a square root temperature dependence to the rate variable R. However, since the vapor pressure inside increases as $(T/T_o)^{28}$, the instantaneous increases in the rate due to the particle addition can be neglected and only the temperature dependent increase in pressure P_{in} needs to be considered. Previous study shows that the equilibrium happens quickly inside the crucible with in 5 ms [103].

The flow rate can be estimated to be proportional to the square root of the Si vapor pressure from equation B.2, therefore $R \propto T^{14}$. The amount of Si sublimated from the SiC surfaces during a monolayer growth on Si-face can be calculated by looking at the graphene amount on both surfaces. Assuming monolayer graphene growth on Si face and three layers of graphene on C-face, considering the buffer layer as well, the total thickness of SiC to be thermally decomposed can be taken as 3.75 nm (.75 nm x 5). The filling factor of the SiC crystal (4H and 6H) is 0.74 and half of the atoms are Si. For a chip size of 3 mm x 4 mm, an estimate of Si atoms that will leave the chip is on the order of 2.45e15 atoms. If the decomposition happens in one minute, then the rate is 4.08e13 atoms/sec.

Figure B.2: The shrunk shape and size of SiC stacks show that SiC can be melted at $1740°C$ in six hours in the confinement controlled sublimation setup. The melting point of SiC under atmospheric pressure is $2730°C$.

In order to establish the rate of 4.08e13 atoms/sec from equation B.2, the density needs to be estimated and then the growth temperature that leads to monolayer graphene, can be guessed. Getting the pressure info from Figure B.1 (a) as 2e-3 pascal and knowing that $A_2 = 5e - 5m^2$ from the crucible design,

Knowing that $1550°C$ gives monolayer graphene on the Si-face, the required density ρ can be calculated. Then this value can be used to estimate the required time for a given temperature or the temperature required for a given time.

Additionally, to show the capability of the confinement controlled sublimation setup, we show in Figure B.2 that a SiC stack was melted at $1740°C$ in six hours. Initially the SiC chips were clear transparent and after the melting they have obtained the yellow color. For comparison, the melting point of SiC under atmospheric pressure is $2730°C$.

APPENDIX C

LATERAL FORCE MICROSCOPY

LFM is quite similar to non contact-AFM, except the position sensitive photo detectors are aligned laterally (compared to vertically aligned topography detectors(A-B)) to receive the reflecting laser beam from the cantilever. The force constant of the tip can be first set to 4 nN and can be increased to 6nN range as the tip wears out.

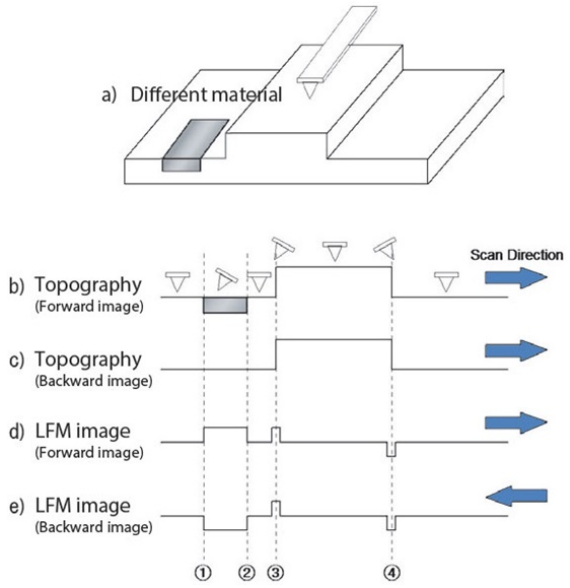

Figure C.1: A diagram of LFM vs topography signals. As the tip scans a low friction region (labeled as ”Different Material” in the drawing))on a flat area, topography does not pick up a signal. The LFM signal picked up over topographic features can be removed by subtraction of back and forth LFM scans. The subtracted data gives the contrast over the low or high friction region. Reprinted from [140], Copyright 2018 by Park Systems.

APPENDIX D

CONDUCTIVE PROBE MICROSCOPY

Conductive probe microscopy is a three probe measurement system where the surface potentiometry of a nanoribbon can be made with a contact mode AFM tip. A bias voltage applied on the nanoribbon through its two contacts and the potential between the AFM tip and the second contact is recorded (Figure 4.5). One to one matching of this potentiometry data to other contact mode AFM measurements (topography, error signal (morphology) and lateral force (surface friction)) can help identifying the transport features of the surface material.

Tuning of the parameters (Figure 4.5) in conductive probe microscopy is critical for a clear contrast in the voltage reading. AFM scan frequency for a single line can be set anywhere between 0.1 Hz to 0.3 Hz for $10\mu m$ scan length (faster scans decreases tip lifetime and slower scans suffer from thermal expansion). This means one line can be scanned back and forth in the range of 3 to 10 seconds. A high resolution AFM image needs at least 512 pixels. This corresponds to 20.00 ms to 6.50 ms tip time per a single pixel.

The time spent over a single pixel is a critical parameter, since this is the only time frame that a voltage measurement can be collected for the location. In order to get a low variation in the measurement, averaging of few measurements need to be considered. For a lock-in based measurement technique, this s established by default; however the time spent on a single pixel should be larger than the integration time of the lock-in. For example; for a scan that is $15\mu m$ long, a scan frequency of 0.2 Hz can be picked. This will correspond to roughly 10 ms tip time over a pixel for a 512 pixels (30 nm/pixel). Next,the time constant of the lock-in (the integration - averaging time) needs to be less than 10 ms, so it can be set to 5 ms. The last parameter is the modulation frequency of the lock-in, which should be less than the time constant. 1kHz modulation frequency can be chosen since it corresponds

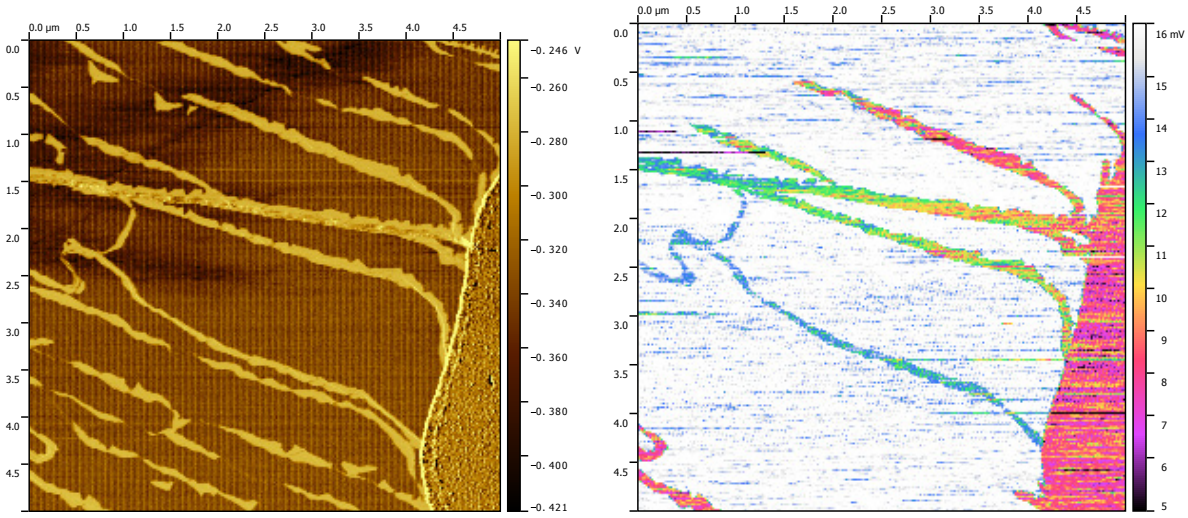

Figure D.1: LFM map and the potentiometry of the graphene ribbon - amorphous carbon interface. One to one mapping enables detecting which ribbon patches are active in the transport. Conductive probe measurement on the contact interface can also help identification of the contact resistance. The color scale is inverted for a better contrast.

to a period of 1 ms, which is less than the time constant.

The noise in the potentiometry measurement can be lowered by choosing a higher modulation frequency, however increasing the modulation frequency, increases the interface resistance (see Contact Resistance and Surface Potentiometry in Chapter 4).

The conductive probe spectroscopy needs to be performed with a lock-in modulation frequency of 1kHz, which is two orders of magnitudes higher than the modulation frequency used for conventional measurements($\approx 17Hz$). The high frequency causes a 30% increase in the overall resistance, but the high frequency is necessary to work along with AFM scan speeds and to avoid drifting of the sample that emerges in case of a slow scan as mentioned above.

APPENDIX E

THE CIRCUIT DIAGRAMS

In this section the circuit diagrams that explain the resistor network model that was mentioned in the Transport Measurements Chapter are presented. transport phenomena are presented.

Figure E.1 shows a series of approximations that are made to simplify the circuit and the calculations. The average measured resistance values for the resistors are $R_A \approx R_B \approx 100k\Omega$ and $R_1 \approx 10M\Omega, R_2 \approx 1M\Omega$. Considering these measured values, the approximations in Figure E.1 can be made, giving the final circuit (Figure E.1 (g)). A two point measurement over R_A would be be affected by the parallel resistors $(R_1 + R_2)/2$, but since the parallel resistances are at least ten times larger, a change more than 10% in R_A measurement is avoided.

The process start with the simple circuit that is shown in Figure E.1 (a) and the resulting resistor network shown in Figure E.1 (b). Using the relation $R_1 + R_2 \ll R_A$ a series of approximations lead to the circuit given in figure E.1 (g).

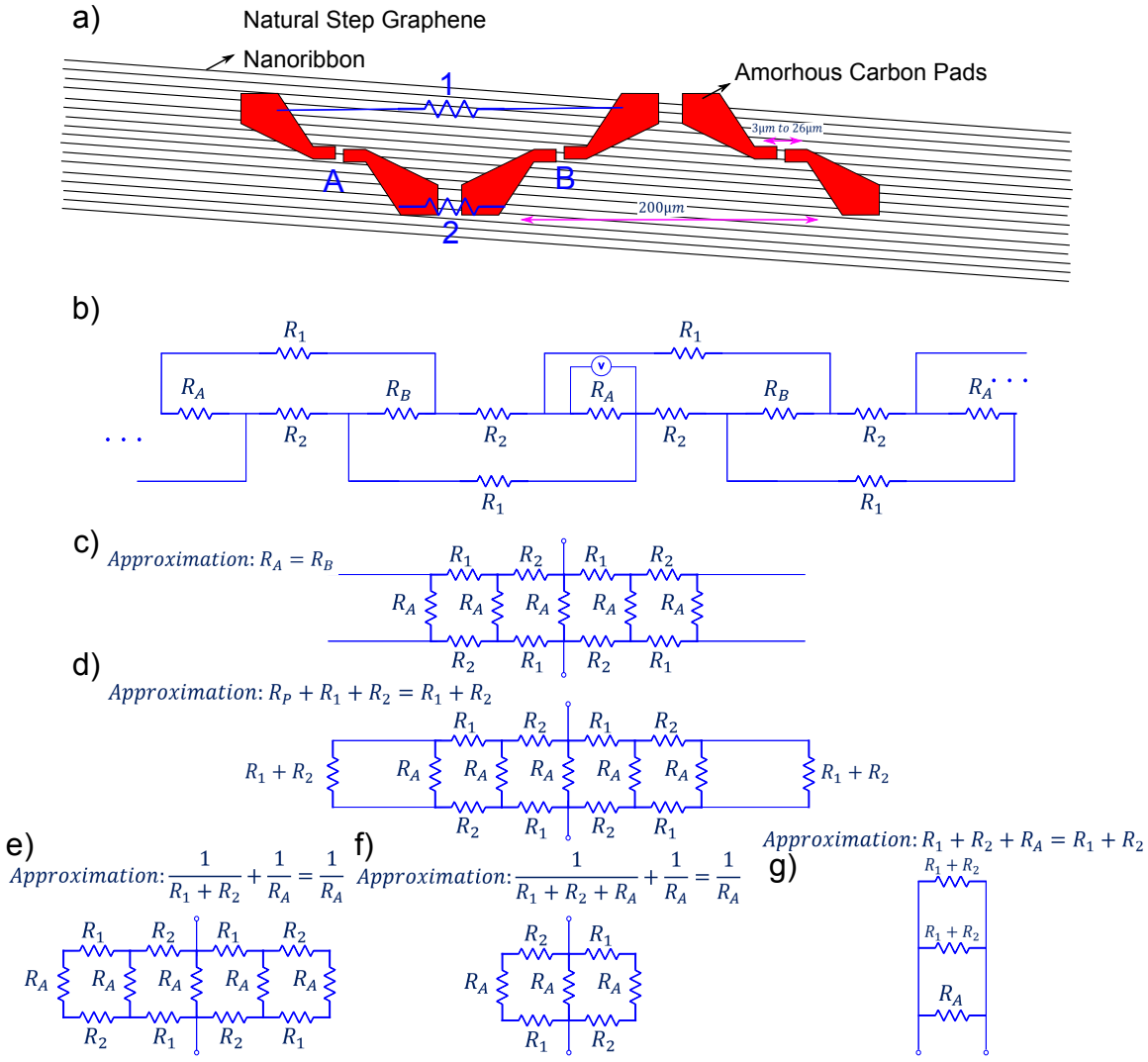

Figure E.1: (a) The contact patterns and the distribution of the natural step ribbons. b) the equivalent resistor network. c) After the first approximation $R_A = R_B$ the circuit simplifies to a three variable network. d) Since the repeating circuit will have a small value to due to many parallel circuits, its contribution R_p can be ignored in the series circuit $R_1 + R_2 + R_p$. e) Since $R_1 + R_2 + R_A \ll R_A$ the equivalent parallel resistance can be approximated to R_A. f) Similar to d) the equivalent parallel resistance is approximated to R_A. g) The two series resistances $R_1 + R_2 + R_A$ are approximated to $R_1 + R_2$.

APPENDIX F

THE AUTOMATED VACUUM PROBE STATION

During this PhD work I built an automated probe station to perform transport measurements in vacuum on contacted GNRs. The setup consists of a vacuum chamber attached to a turbo pump. Inside the chamber there are four micro-manipulators with x-y-z piezo controllers (SL-06 from the company SmartAct) provided with electrical probes and connected by feed through bnc connections. A home made heating element (can heat up to $450°C$), a camera and a LabVIEW program to automatically move the probes.

Once the sample is placed inside the chamber on the copper element, the transparent plexiglass cover is closed and the chamber can be pumped down to $10^{-6}mbar$. The change in resistance during this period can be recorded. An average resistance drop up to 50% is usually observed in graphene samples. The vent inlet can also be used to inject of various gases to the chamber.

The heating element consists of a copper piece that is insulated by a BN coating and a twisted (and also BN coated) chromium wire that surrounds it. The heat insulation layer consists of Sodium Silicate as high temperature glue and Perlite as the filling and insulating medium. The insulation layer is necessary since the micro-manipulators are designed to perform below $40°C$. We have tested that the insulation amount is sufficient to safely operate the manipulators. The heating area can be safely heated up to $400°C$.

Due to high number of measurements needed in periodic arrangement of contacts, I wrote a LabVIEW program to automatically move the probes from one set of contacts to another automatically. The LabVIEW program can control each probe with 50 nm accuracy. Upon establishing a contact with pads the voltage measurements from the connected Lock-in amplifiers can be read through GPIB connections. The sample temperature can also be recorded through a thermocouple connection. Along with all these features, the

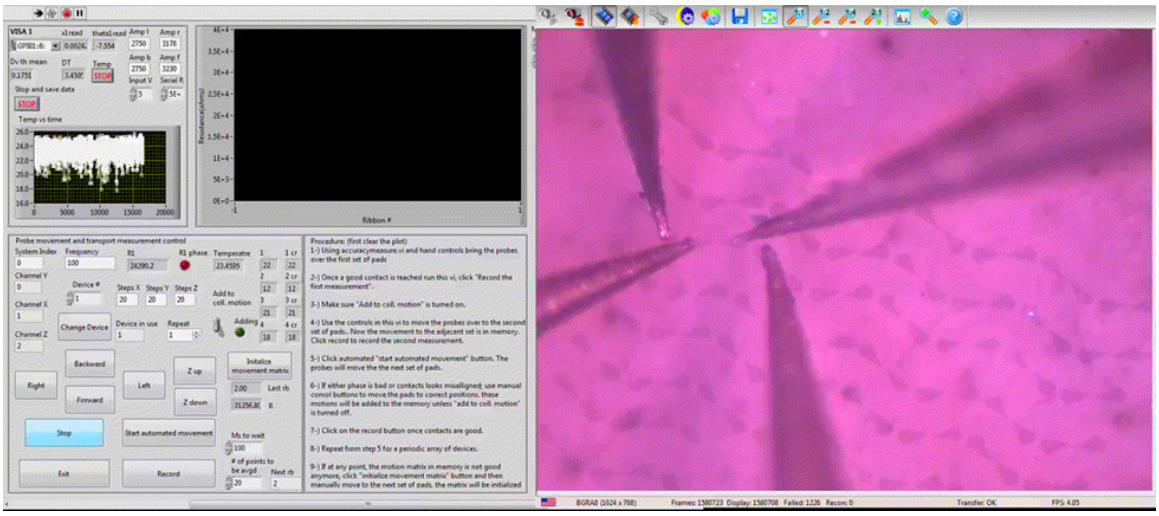

Figure F.1: The LabVIEW interface of the automated vacuum probe station and the simultaneous imaging of the probes.

automation program shown in Figure F.1 can take the periodicity of the pad pattern as an input and move the tips automatically to their next location between the measurements. Therefore it significantly decreases the time spent on taking measurements considering each chip has nearly 100 nanoribbons and contact pairs on it and overall the course of this study, nearly 12000 individual nanoribbons are measured.

The automated probes station also has a copper bridge that is attached to both the sample holder and the feed-through connection that goes outside of the chamber. In further development a cold head-He compressor combination setup can be attached to this bridge to cool the sample below 10 K. Therefore combined with the heating element, a temperature range from 10K to 700K can be established in this setup.

APPENDIX G
ADDITIONAL RIBBON MEASUREMENTS

Numerous GNR measurements have been performed, but due to sidewalls, alignment problems and different levels of contamination a large variation in the measurements was observed. Most of such measurements are disregarded, since the following improved fabrication techniques increased the consistency of the results. However, I present here some of the earlier measurements I made in order to show the variation and discuss how much the improved factors affect the result.

The fist resistance vs length data (Figure G.1) contains sidearms. It is important to test whether these sidearms create scattering centers or short the nanoribbon by creating a resistor network. Both of such intrusions would complicate the problem and make it harder to draw a conclusion on the ribbons' electronic properties.

The data sets also are presented to show the effect of edge termination. Four sets of ZZ and AC ribbons are plotted together and only in the short length scales (Figure G.1) a difference in the resistance vs length profile can be observed. ZZ ribbons seem to linearly extrapolate to $25k\Omega$ while AC ribbons seem to have an increasing slope below $7\mu m$. Even though sidearms are observed for these samples and the orientation of these sidearms are attributed to the difference in the resistance, the short circuiting effect of the sidearms was not concluded. Therefore this data set is presented as the only transport measurement that shows a difference between AC and ZZ ribbons.

The second data set (Figure G.2) is from short ribbons with metal contacts. Metal is deposited after the graphene growth, therefore the contamination effects are higher than the aC contacted nanoribbons.

The last data set shows the four point measurements of the ribbons that were previously presented in the temperature dependent measurements section (Figure 4.16 (c) and (d)).

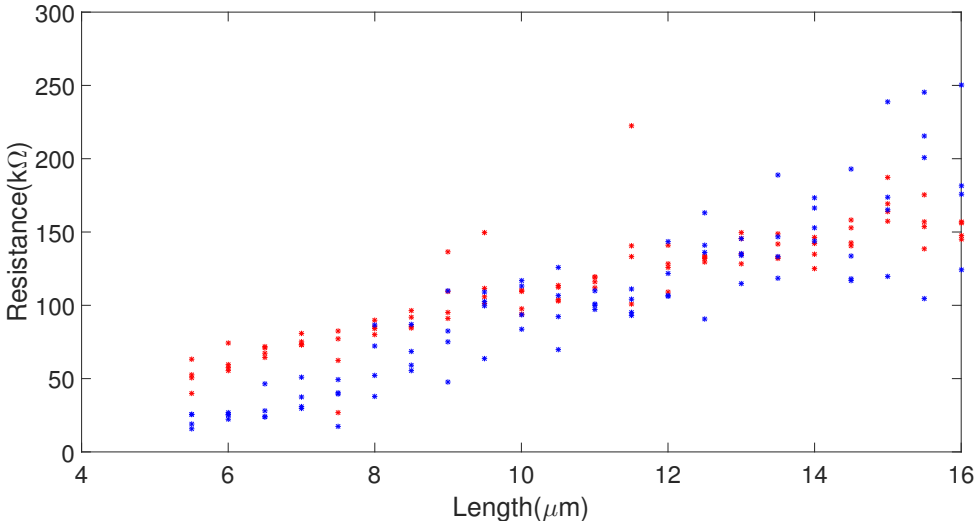

Figure G.1: Zoomed in version of the previous figure shows the difference in short lengths between the two directions. ZZ ribbons are red while AC ribbons blue.

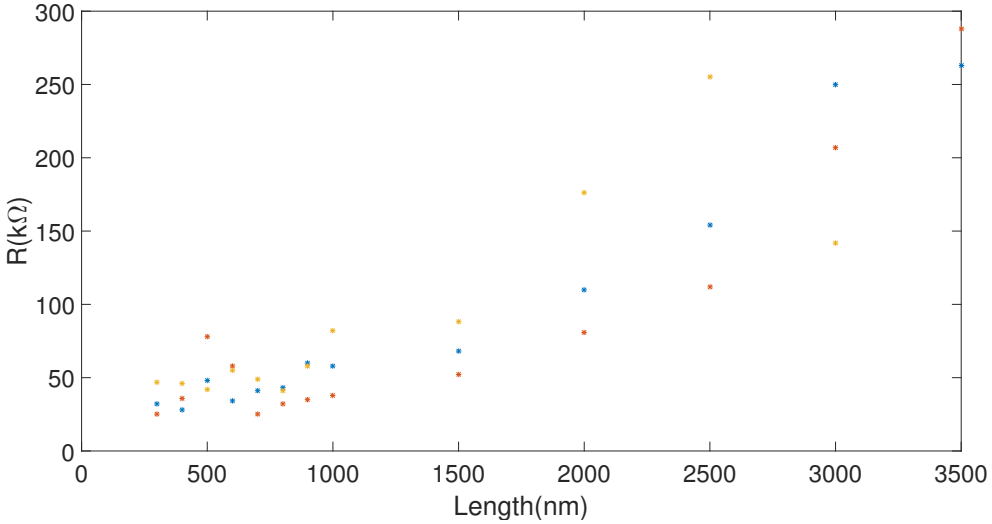

Figure G.2: Four point measurements of short ribbons with Au/Pd contacts. The samples suffer from post growth fabrication residues, so the longer lengths are highly resistive.

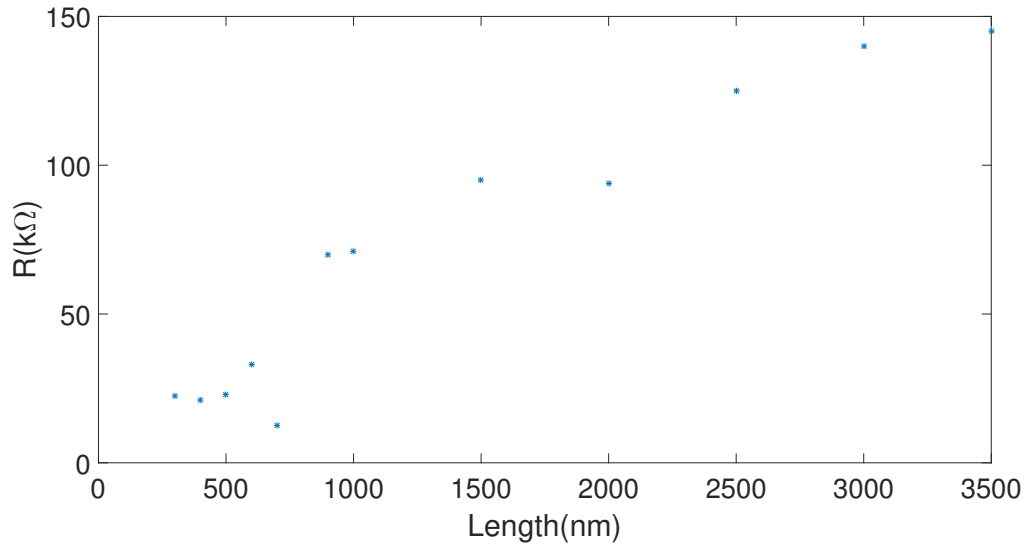

Figure G.3: Room temperature four point measurements of short ribbons with Au/Pd contacts that were given in Figure 4.16 (c) and (d). The samples were annealed at 420 K prior to the cooling in the cryostat. The conventional annealing temperature $400°C$ was not reached for the given ribbons, because it is problematic with gold contacts and it can not be established with the heating restrictions in the cryostat.

Gold contacts are known to dissipate over graphene if the samples are annealed above $100°C$. This is an observed effect on GNRs with Au contacts and there is not a reference of a systematic study of this effect, but the motion of gold clusters on graphene upon heating is reported [141]. Therefore we avoid annealing metal contacted GNRs, in return we can not obtain relatively clean and impurity free GNRs. This is why mostly amorphous carbon contacted nanoribbons were preferred in the course of this study.

The mask design that allows placement of both ZZ and AC ribbons on the same chip is given in Figure G.4. This mask design allows similar coverage of graphene to be obtained on the sidewalls on both AC and ZZ ribbons, so the effect of the ribbon direction on the transport can be tested. However, as mentioned earlier, the dominating factor on the morphological confinement is the density and the direction of natural steps of a chip. Due to all these factors, for the measurements in the main text, masks with single ribbon directions are chosen.

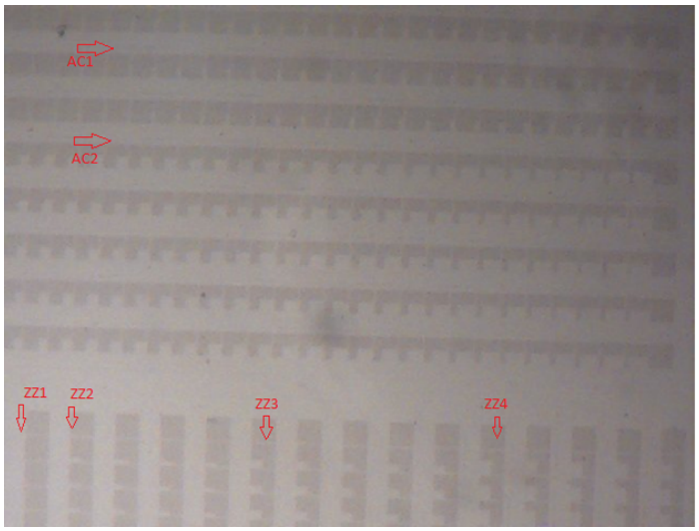

Figure G.4: The chip design for the following figures. Mesas etched in the AC and ZZ directions are not visible in the image, but the increasing separation between the pads can be seen. Each nanoribbon length is repeated at least four times. Contacts are made of amorphous carbon.

APPENDIX H

MAGNETO-RESISTANCE

Ribbons with different contacts at various lengths are measured at low temperature to see the effect of magnetic field on the nanoribbon resistance.

For nanoribbon lengths that are longer than $1\mu m$ a set of MR measurements are performed at 1.78K (Figure H.1). The changes upon the same magnetic field sweep (8T to -8T) (Figure H.1 bottom right) are $\%9.6, \%9.6, \%6.8, \%8.9, \%10.1$ for nanoribbon lengths $1.5\mu m, 2\mu m, 2.5\mu m, 3\mu m$ and $3.5\mu m$. Except the $\%6.8$ change, the MR response may be saturating for these length scales.

The last measurement combines the gate voltage variation and the external magnetic field sweep. The gate built over the nanoribbon includes an oxide layer that is deposited with and ALD system after a thin seed layer Al deposition as explained in the second chapter. Deposited Al_2O_3 is roughly 25 nm thick.

Firstly, we observe that the gate affects the resistance, highly charges graphene and causes electron doping. Charge traps over the GNR result in unusual resistance patterns upon sweeping the gate voltage. In order to test the presence of charge traps, the gate voltage is swept at different magnetic field values. If these features were affected by the applied field then they can be linked to the magnetic structure of the material. Figure H.2 shows the gate voltage sweep and step-wise increased magnetic field values. The same nanoribbons from Figure H.1 are used. The color scale as an indicator of the magnetic field is not given, because the goal of this observation is to observe shifts (laterally) in the peaks that emerge in the gate voltage sweep. No such shift is observed when the external field is changed. The only change in the resistance is due to MR that was shown in Figure H.1. The overall resistance during a sweep drops as the magnetic field is increased but the positions of the resistance peaks are preserved. Also no charge neutrality point is present in gated

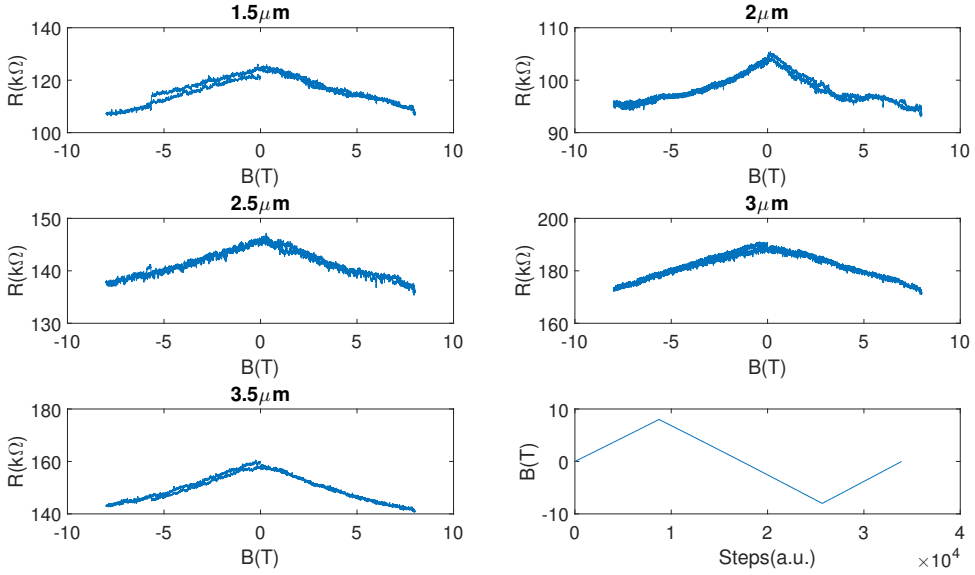

Figure H.1: Magneto-resistance plots of four point metal contacted long SWGNRs. The magnetic field variation can be seen from the bottom right figure. The maximum and minimum points are 8T and -8T. The temperature is 1.78 K.

ribbons. Charge neutrality has been observed only in a few samples for gated GNRs during the course of this study.

More detailed MR and spin transport measurements that includes spin injection to GNRs with magnetic leads can be found in [142].

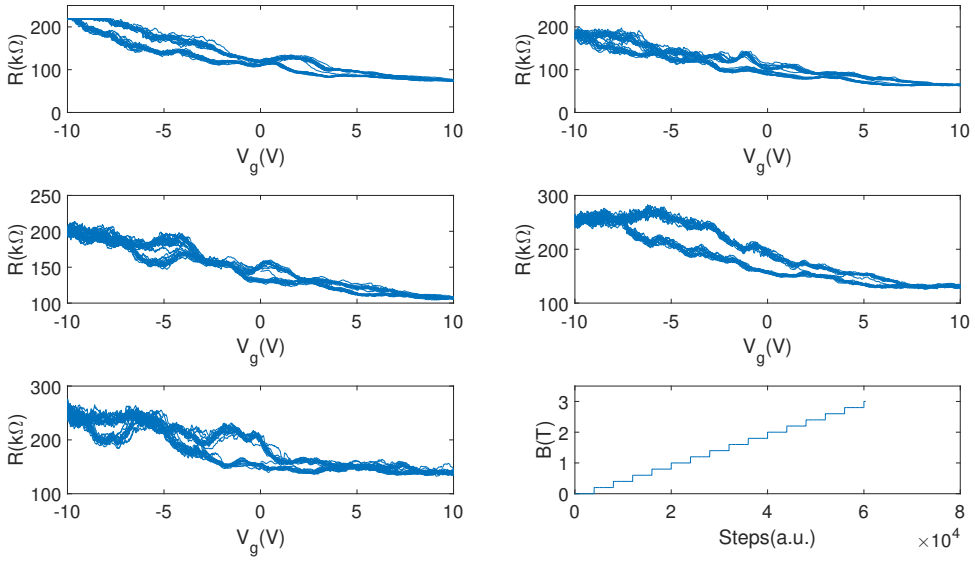

Figure H.2: Gate scans of nanoribbons (from Figure H.1) while the magnetic field is increased in steps. The gate voltage is scanned from -10V to 10V at each step of the magnetic field. The purpose of this measurement is to see whether these resistance features that appear during a gate scan are magnetic field dependent parameters or not. The color scale (for magnetic field) is not added but the magnetic field variation can be seen from the bottom right figure. A total of fifteen gate sweeps are made at different magnetic fields ranging from 0 to 3 T. The temperature is 1.6 K.

REFERENCES

[1] P Drude, "On the electron theory of metals," *Ann Phys*, vol. 1, pp. 566–613, 1900.

[2] H. K. Onnes, "The superconductivity of mercury," *Comm. Phys. Lab. Univ. Leiden*, vol. 122, p. 124, 1911.

[3] M. von Laue, "Concerning the detection of x-ray interferences," *Nobel lecture*, vol. 13, 1915.

[4] W. H. Bragg and W. L. Bragg, "The reflection of x-rays by crystals," *Proceedings of the Royal Society of London. Series A, Containing Papers of a Mathematical and Physical Character*, vol. 88, no. 605, pp. 428–438, 1913.

[5] C. Kittel, *Introduction to Solid State Physics*. Wiley, 2005.

[6] N. W. Ashcroft and N. D. Mermin, *Solid State Physics*. Brooks Cole, 1976.

[7] F. Bloch, "Über die quantenmechanik der elektronen in kristallgittern," *Zeitschrift für Physik A Hadrons and Nuclei*, vol. 52, no. 7, pp. 555–600, 1929.

[8] V. Ginzburg and L. Landau, "On the theory of superconductivity," *J. Exptl. Theoret. Phys.(USSR)*, vol. 20, p. 1064, 1950.

[9] J. Bardeen, L. N. Cooper, and J. R. Schrieffer, "Theory of superconductivity," *Physical Review*, vol. 108, no. 5, p. 1175, 1957.

[10] K. Von Klitzing, "The quantized hall effect," *Reviews of Modern Physics*, vol. 58, no. 3, p. 519, 1986.

[11] L. D. Landau and E. M. Lifshitz, *Quantum mechanics: non-relativistic theory*. Elsevier, 2013, vol. 3.

[12] H. L. Stormer, D. C. Tsui, and A. C. Gossard, "The fractional quantum hall effect," *Reviews of Modern Physics*, vol. 71, no. 2, S298, 1999.

[13] R. F. Curl and R. E. Smalley, "Probing c60," *Science*, vol. 242, no. 4881, pp. 1017–1022, 1988.

[14] S. Iijima and T. Ichihashi, "Single-shell carbon nanotubes of 1-nm diameter," *Nature*, vol. 363, no. 6430, p. 603, 1993.

[15] R. de Picciotto, H. Stormer, L. Pfeiffer, K. Baldwin, and K. West, "Four-terminal resistance of a ballistic quantum wire," *Nature*, vol. 411, no. 6833, pp. 51–54, 2001.

[16] P. Poncharal, C. Berger, Y. Yi, Z. Wang, and W. A. de Heer, "Room temperature ballistic conduction in carbon nanotubes," *The Journal of Physical Chemistry B*, vol. 106, no. 47, pp. 12 104–12 118, 2002.

[17] J. Bardeen and W. H. Brattain, "The transistor, a semi-conductor triode," *Physical Review*, vol. 74, no. 2, p. 230, 1948.

[18] H. N. Khan, D. A. Hounshell, and E. R. Fuchs, "Science and research policy at the end of moores law," *Nature Electronics*, vol. 1, no. 1, p. 14, 2018.

[19] M. Orlita, C. Faugeras, P. Plochocka, P. Neugebauer, G. Martinez, D. K. Maude, A.-L. Barra, M. Sprinkle, C. Berger, W. A. De Heer, *et al.*, "Approaching the dirac point in high-mobility multilayer epitaxial graphene," *Physical review letters*, vol. 101, no. 26, p. 267 601, 2008.

[20] W. Contributors, *Allotropes of carbon — wikipedia, the free encyclopedia*, [Online; accessed 22-January-2018], 2018.

[21] "The structure of graphite," *Proceedings of the Royal Society of London A: Mathematical, Physical and Engineering Sciences*, vol. 106, no. 740, pp. 749–773, 1924.

[22] J Hass, W. De Heer, and E. Conrad, "The growth and morphology of epitaxial multilayer graphene," *Journal of Physics: Condensed Matter*, vol. 20, no. 32, p. 323 202, 2008.

[23] P. R. Wallace, "The band theory of graphite," *Physical Review*, vol. 71, no. 9, p. 622, 1947.

[24] J. Slonczewski and P. Weiss, "Band structure of graphite," *Physical Review*, vol. 109, no. 2, p. 272, 1958.

[25] A. N. Pasupathy, R. C. Bialczak, J. Martinek, J. E. Grose, L. A. Donev, P. L. McEuen, and D. C. Ralph, "The kondo effect in the presence of ferromagnetism," *Science*, vol. 306, no. 5693, pp. 86–89, 2004.

[26] P. Jarillo-Herrero, S. Sapmaz, C. Dekker, L. P. Kouwenhoven, and H. S. van der Zant, "Electron-hole symmetry in a semiconducting carbon nanotube quantum dot," *Nature*, vol. 429, no. 6990, pp. 389–392, 2004.

[27] C. Dekker, S. Tans, M. Devoret, H Dai, R. E. Smalley, A Thess, and L. Georliga, "Individual single-wall carbon nanotubes as quantum wires," *Nature 386 (6624), 474-477.(1997)*, 1997.

[28] M. Bockrath, D. H. Cobden, P. L. McEuen, N. G. Chopra, A. Zettl, A. Thess, and R. E. Smalley, "Single-electron transport in ropes of carbon nanotubes," *Science*, vol. 275, no. 5308, pp. 1922–1925, 1997.

[29] D.-M. Chen, P. M. Shenai, and Y. Zhao, "Tight binding description on the band gap opening of pyrene-dispersed graphene," *Physical Chemistry Chemical Physics*, vol. 13, no. 4, pp. 1515–1520, 2011.

[30] "Dirac cones in graphene," *TU Delft OpenCourseWare*, Topology in Condensed Matter, Course Materials, Readings, Accessed: 2018-01-25.

[31] L. Brey and H. A. Fertig, "Electronic states of graphene nanoribbons studied with the dirac equation," *Phys. Rev. B*, vol. 73, p. 235 411, 23 2006.

[32] J. McClure, "Diamagnetism of graphite," *Physical Review*, vol. 104, no. 3, p. 666, 1956.

[33] Y. Zhang, J. P. Small, M. E. Amori, and P. Kim, "Electric field modulation of galvanomagnetic properties of mesoscopic graphite," *Physical review letters*, vol. 94, no. 17, p. 176 803, 2005.

[34] M. S. Dresselhaus, G. Dresselhaus, and P. C. Eklund, *Science of fullerenes and carbon nanotubes: their properties and applications*. Academic press, 1996.

[35] C Thomsen, S Reich, and J Maultzsch, "Carbon nanotubes: Basic concepts and physical properties," *Revista de Plasticos Modernos*, 2004.

[36] E Kogan, V. Nazarov, V. Silkin, and M Kaveh, "Energy bands in graphene: Comparison between the tight-binding model and ab initio calculations," *Physical Review B*, vol. 89, no. 16, p. 165 430, 2014.

[37] S. Sharapov, V. Gusynin, and H Beck, "Magnetic oscillations in planar systems with the dirac-like spectrum of quasiparticle excitations," *Physical Review B*, vol. 69, no. 7, p. 075 104, 2004.

[38] C. Berger, Z. Song, T. Li, X. Li, A. Y. Ogbazghi, R. Feng, Z. Dai, A. N. Marchenkov, E. H. Conrad, P. N. First, *et al.*, "Ultrathin epitaxial graphite: 2d electron gas properties and a route toward graphene-based nanoelectronics," *The Journal of Physical Chemistry B*, vol. 108, no. 52, pp. 19 912–19 916, 2004.

[39] C. Berger, Z. Song, X. Li, X. Wu, N. Brown, C. Naud, D. Mayou, T. Li, J. Hass, A. N. Marchenkov, E. H. Conrad, P. N. First, and W. A. de Heer, "Electronic confinement and coherence in patterned epitaxial graphene," *Science*, vol. 312, no. 5777, pp. 1191–1196, 2006.

[40] Y. Zhang, Y.-W. Tan, H. L. Stormer, and P. Kim, "Experimental observation of the quantum hall effect and berry's phase in graphene," *nature*, vol. 438, no. 7065, p. 201, 2005.

[41] K. S. Novoselov, A. K. Geim, S. Morozov, D. Jiang, M. Katsnelson, I. Grigorieva, S. Dubonos, Firsov, and AA, "Two-dimensional gas of massless dirac fermions in graphene," *Nature*, vol. 438, no. 7065, pp. 197–200, 2005.

[42] Y. Zhang, V. W. Brar, F. Wang, C. Girit, Y. Yayon, M. Panlasigui, A. Zettl, and M. F. Crommie, "Giant phonon-induced conductance in scanning tunnelling spectroscopy of gate-tunable graphene," *Nature Physics*, vol. 4, no. 8, p. 627, 2008.

[43] T. Ohta, A. Bostwick, T. Seyller, K. Horn, and E. Rotenberg, "Controlling the electronic structure of bilayer graphene," *Science*, vol. 313, no. 5789, pp. 951–954, 2006.

[44] Y. Zhang, T.-T. Tang, C. Girit, Z. Hao, M. C. Martin, A. Zettl, M. F. Crommie, Y. R. Shen, and F. Wang, "Direct observation of a widely tunable bandgap in bilayer graphene," *Nature*, vol. 459, no. 7248, p. 820, 2009.

[45] J. L. Dos Santos, N. Peres, and A. C. Neto, "Graphene bilayer with a twist: Electronic structure," *Physical review letters*, vol. 99, no. 25, p. 256 802, 2007.

[46] H. Aoki and M. S. Dresselhaus, *Physics of Graphene*. Springer Science & Business Media, 2013.

[47] Y. Cao, V. Fatemi, S. Fang, K. Watanabe, T. Taniguchi, E. Kaxiras, and P. Jarillo-Herrero, "Unconventional superconductivity in magic-angle graphene superlattices," *Nature*, 2018.

[48] Y. Cao, V. Fatemi, A. Demir, S. Fang, S. L. Tomarken, J. Y. Luo, J. Sanchez-Yamagishi, K. Watanabe, T. Taniguchi, E. Kaxiras, *et al.*, "Correlated insulator behaviour at half-filling in magic-angle graphene superlattices," *Nature*, 2018.

[49] T. G. Pedersen, C. Flindt, J. Pedersen, N. A. Mortensen, A.-P. Jauho, and K. Pedersen, "Graphene antidot lattices: Designed defects and spin qubits," *Physical Review Letters*, vol. 100, no. 13, p. 136 804, 2008.

[50] N. Shima and H. Aoki, "Electronic structure of super-honeycomb systems: A peculiar realization of semimetal/semiconductor classes and ferromagnetism," *Physical review letters*, vol. 71, no. 26, p. 4389, 1993.

[51] K. Nakada, M. Fujita, G. Dresselhaus, and M. S. Dresselhaus, "Edge state in graphene ribbons: Nanometer size effect and edge shape dependence," *Physical Review B*, vol. 54, no. 24, p. 17 954, 1996.

[52] Y.-W. Son, M. L. Cohen, and S. G. Louie, "Energy gaps in graphene nanoribbons," *Phys. Rev. Lett.*, vol. 97, p. 216 803, 21 2006.

[53] Y.-W. Son, M. L. Cohen, and S. G. Louie, "Half-metallic graphene nanoribbons," *Nature*, vol. 444, no. 7117, pp. 347–349, 2006.

[54] J. Cai, P. Ruffieux, R. Jaafar, M. Bieri, T. Braun, S. Blankenburg, M. Muoth, A. P. Seitsonen, M. Saleh, X. Feng, *et al.*, "Atomically precise bottom-up fabrication of graphene nanoribbons," *Nature*, vol. 466, no. 7305, p. 470, 2010.

[55] K. Wakabayashi, Y. Takane, M. Yamamoto, and M. Sigrist, "Edge effect on electronic transport properties of graphene nanoribbons and presence of perfectly conducting channel," *Carbon*, vol. 47, no. 1, pp. 124–137, 2009.

[56] D. A. Areshkin, D. Gunlycke, and C. T. White, "Ballistic transport in graphene nanostrips in the presence of disorder: Importance of edge effects," *Nano letters*, vol. 7, no. 1, pp. 204–210, 2007.

[57] B. Biel, F. Garcia-Vidal, A. Rubio, and F. Flores, "Anderson localization in carbon nanotubes: Defect density and temperature effects," *Physical review letters*, vol. 95, no. 26, p. 266 801, 2005.

[58] S. Latil, S. Roche, D. Mayou, and J.-C. Charlier, "Mesoscopic transport in chemically doped carbon nanotubes," *Physical review letters*, vol. 92, no. 25, p. 256 805, 2004.

[59] M. Y. Han, B. Özyilmaz, Y. Zhang, and P. Kim, "Energy band-gap engineering of graphene nanoribbons," *Physical review letters*, vol. 98, no. 20, p. 206 805, 2007.

[60] C. G. Kang, J. W. Kang, S. K. Lee, S. Y. Lee, C. H. Cho, H. J. Hwang, Y. G. Lee, J. Heo, H.-J. Chung, H. Yang, *et al.*, "Characteristics of cvd graphene nanoribbon formed by a zno nanowire hardmask," *Nanotechnology*, vol. 22, no. 29, p. 295 201, 2011.

[61] D Basu, M. Gilbert, L. Register, S. K. Banerjee, and A. H. MacDonald, "Effect of edge roughness on electronic transport in graphene nanoribbon channel metal-oxide-semiconductor field-effect transistors," *Applied Physics Letters*, vol. 92, no. 4, p. 042 114, 2008.

[62] F Cervantes-Sodi, G Csanyi, S Piscanec, and A. Ferrari, "Edge-functionalized and substitutionally doped graphene nanoribbons: Electronic and spin properties," *Physical Review B*, vol. 77, no. 16, p. 165 427, 2008.

[63] Q. Yan, B. Huang, J. Yu, F. Zheng, J. Zang, J. Wu, B.-L. Gu, F. Liu, and W. Duan, "Intrinsic current- voltage characteristics of graphene nanoribbon transistors and effect of edge doping," *Nano letters*, vol. 7, no. 6, pp. 1469–1473, 2007.

[64] N. A. Poklonski, E. F. Kislyakov, S. A. Vyrko, O. N. Bubel, and S. V. Ratkevich, "Electronic band structure and magnetic states of zigzag graphene nanoribbons: Quantum chemical calculations," *Journal of Nanophotonics*, vol. 6, no. 1, p. 061 712, 2012.

[65] J. P. Llinas, A. Fairbrother, G. B. Barin, W. Shi, K. Lee, S. Wu, B. Y. Choi, R. Braganza, J. Lear, N. Kau, *et al.*, "Short-channel field-effect transistors with 9-atom and 13-atom wide graphene nanoribbons," *Nature communications*, vol. 8, no. 1, p. 633, 2017.

[66] C. Bronner, R. A. Durr, D. J. Rizzo, Y.-L. Lee, T. Marangoni, A. M. Kalayjian, H. Rodriguez, W. Zhao, S. G. Louie, F. R. Fischer, *et al.*, "Hierarchical on-surface synthesis of graphene nanoribbon heterojunctions," *ACS nano*, 2018.

[67] M. Sprinkle, M. Ruan, Y. Hu, J Hankinson, M. Rubio-Roy, B. Zhang, X. Wu, C. Berger, and W. A. De Heer, "Scalable templated growth of graphene nanoribbons on sic," *Nature Nanotechnology*, vol. 5, no. 10, pp. 727–731, 2010.

[68] H. Nakagawa, S. Tanaka, and I. Suemune, "Self-ordering of nanofacets on vicinal sic surfaces," *Physical review letters*, vol. 91, no. 22, p. 226 107, 2003.

[69] R. M. Jacobberger, B. Kiraly, M. Fortin-Deschenes, P. L. Levesque, K. M. McElhinny, G. J. Brady, R. R. Delgado, S. S. Roy, A. Mannix, M. G. Lagally, *et al.*, "Direct oriented growth of armchair graphene nanoribbons on germanium," *Nature communications*, vol. 6, p. 8006, 2015.

[70] J. Kunc, Y. Hu, J. Palmer, Z. Guo, J. Hankinson, S. H. Gamal, C. Berger, and W. A. De Heer, "Planar edge schottky barrier-tunneling transistors using epitaxial graphene/sic junctions," *Nano letters*, vol. 14, no. 9, pp. 5170–5175, 2014.

[71] A. M. Ionescu and H. Riel, "Tunnel field-effect transistors as energy-efficient electronic switches," *nature*, vol. 479, no. 7373, p. 329, 2011.

[72] V. Katkov and V. Osipov, "Planar graphene tunnel field-effect transistor," *Applied Physics Letters*, vol. 104, no. 5, p. 053 102, 2014.

[73] J. Park, A. N. Pasupathy, J. I. Goldsmith, C. Chang, Y. Yaish, J. R. Petta, M. Rinkoski, J. P. Sethna, H. D. Abruña, P. L. McEuen, *et al.*, "Coulomb blockade and the kondo effect in single-atom transistors," *Nature*, vol. 417, no. 6890, p. 722, 2002.

[74] D Deniz, P Gartland, and D Davidovic, "Emerging magnetic effects of au break junctions with embedded ni nanoparticles," *Journal of Nanoscience with Advanced Technology*, vol. 1, no. 2, pp. 1–5, 2015.

[75] Y. Lu, B. Goldsmith, D. R. Strachan, J. H. Lim, Z. Luo, and A. Johnson, "High-on/off-ratio graphene nanoconstriction field-effect transistor," *Small*, vol. 6, no. 23, pp. 2748–2754, 2010.

[76] K. A. Ritter and J. W. Lyding, "The influence of edge structure on the electronic properties of graphene quantum dots and nanoribbons," *Nature materials*, vol. 8, no. 3, p. 235, 2009.

[77] P. Gallagher, K. Todd, and D. Goldhaber-Gordon, "Disorder-induced gap behavior in graphene nanoribbons," *Physical Review B*, vol. 81, no. 11, p. 115 409, 2010.

[78] M. Y. Han, J. C. Brant, and P. Kim, "Electron transport in disordered graphene nanoribbons," *Physical review letters*, vol. 104, no. 5, p. 056 801, 2010.

[79] H. A. Nilsson, P. Caroff, C. Thelander, E. Lind, O. Karlström, and L.-E. Wernersson, "Temperature dependent properties of insb and inas nanowire field-effect transistors," *Applied Physics Letters*, vol. 96, no. 15, p. 153 505, 2010.

[80] W. S. Hwang, P. Zhao, K. Tahy, L. O. Nyakiti, V. D. Wheeler, R. L. Myers-Ward, C. R. Eddy Jr, D. K. Gaskill, J. A. Robinson, W. Haensch, *et al.*, "Graphene nanoribbon field-effect transistors on wafer-scale epitaxial graphene on sic substrates," *APL materials*, vol. 3, no. 1, p. 011 101, 2015.

[81] G. Liang, N. Neophytou, D. E. Nikonov, and M. S. Lundstrom, "Performance projections for ballistic graphene nanoribbon field-effect transistors," *IEEE Transactions on Electron Devices*, vol. 54, no. 4, pp. 677–682, 2007.

[82] M. Ruan, "Structured epitaxial graphene for electronics," *Georgia Institute of Technology*, 2012.

[83] M. Ruan, Y. Hu, Z. Guo, R. Dong, J. Palmer, J. Hankinson, C. Berger, and W. A. De Heer, "Epitaxial graphene on silicon carbide: Introduction to structured graphene," *MRS bulletin*, vol. 37, no. 12, pp. 1138–1147, 2012.

[84] J. Baringhaus, M. Ruan, F. Edler, A. Tejeda, M. Sicot, A. Taleb-Ibrahimi, A.-P. Li, Z. Jiang, E. H. Conrad, C. Berger, *et al.*, "Exceptional ballistic transport in epitaxial graphene nanoribbons," *Nature*, vol. 506, no. 7488, pp. 349–354, 2014.

[85] R. Landauer, "Electrical transport in open and closed systems," *Zeitschrift für Physik B Condensed Matter*, vol. 68, no. 2-3, pp. 217–228, 1987.

[86] S. Datta, *Electronic transport in mesoscopic systems*. Cambridge University Press, 1997.

[87] H. Heinrich, G. Bauer, and F. Kuchar, *Physics and technology of submicron structures: proceedings of the fifth international winter school, Mauterndorf, Austria, February 22-26, 1988*. Springer Verlag, 1988, vol. 83.

[88] D. Gall, "Electron mean free path in elemental metals," *Journal of Applied Physics*, vol. 119, no. 8, p. 085 101, 2016.

[89] J. Baringhaus, "Mesoscopic transport phenomena in epitaxial graphene nanostructures : A surface science approach," *Hannover : Technische Informationsbibliothek u. Universitätsbibliothek*, 2015.

[90] K. Wakabayashi, Y. Takane, and M. Sigrist, "Perfectly conducting channel and universality crossover in disordered graphene nanoribbons," *Physical Review Letters*, vol. 99, no. 3, p. 036 601, 2007.

[91] R. Landauer, "Spatial variation of currents and fields due to localized scatterers in metallic conduction," *IBM Journal of Research and Development*, vol. 1, no. 3, pp. 223–231, 1957.

[92] N. Mott, "Conduction in non-crystalline materials: Iii. localized states in a pseudogap and near extremities of conduction and valence bands," *Philosophical Magazine*, vol. 19, no. 160, pp. 835–852, 1969.

[93] M Büttiker, "Four-terminal phase-coherent conductance," *Physical review letters*, vol. 57, no. 14, p. 1761, 1986.

[94] L. Malard, M. Pimenta, G Dresselhaus, and M. Dresselhaus, "Raman spectroscopy in graphene," *Physics Reports*, vol. 473, no. 5-6, pp. 51–87, 2009.

[95] A. C. Ferrari, J. Meyer, V Scardaci, C Casiraghi, M. Lazzeri, F. Mauri, S Piscanec, D. Jiang, K. Novoselov, S Roth, *et al.*, "Raman spectrum of graphene and graphene layers," *Physical review letters*, vol. 97, no. 18, p. 187 401, 2006.

[96] T. Mohiuddin, A Lombardo, R. Nair, A Bonetti, G Savini, R Jalil, N. Bonini, D. Basko, C Galiotis, N Marzari, *et al.*, "Uniaxial strain in graphene by raman spectroscopy: G peak splitting, grüneisen parameters, and sample orientation," *Physical Review B*, vol. 79, no. 20, p. 205 433, 2009.

[97] I. Childres, L. A. Jauregui, M. Foxe, J. Tian, R. Jalilian, I. Jovanovic, and Y. P. Chen, "Effect of electron-beam irradiation on graphene field effect devices," *Applied Physics Letters*, vol. 97, no. 17, p. 173 109, 2010.

[98] G. Lu, L. E. Ocola, and J. Chen, "Reduced graphene oxide for room-temperature gas sensors," *Nanotechnology*, vol. 20, no. 44, p. 445 502, 2009.

[99] D. B. Farmer, R. Golizadeh-Mojarad, V. Perebeinos, Y.-M. Lin, G. S. Tulevski, J. C. Tsang, and P. Avouris, "Chemical doping and electron-hole conduction asymmetry in graphene devices," *Nano Letters*, vol. 9, no. 1, pp. 388–392, 2008.

[100] M. Ishigami, J. Chen, W. Cullen, M. Fuhrer, and E. Williams, "Atomic structure of graphene on sio2," *Nano letters*, vol. 7, no. 6, pp. 1643–1648, 2007.

[101] A Pirkle, J Chan, A Venugopal, D Hinojos, C. Magnuson, S McDonnell, L Colombo, E. Vogel, R. Ruoff, and R. Wallace, "The effect of chemical residues on the physical and electrical properties of chemical vapor deposited graphene transferred to sio2," *Applied Physics Letters*, vol. 99, no. 12, p. 122 108, 2011.

[102] J. A. Robinson, M. LaBella, M. Zhu, M. Hollander, R. Kasarda, Z. Hughes, K. Trumbull, R. Cavalero, and D. Snyder, "Contacting graphene," *Applied Physics Letters*, vol. 98, no. 5, p. 053 103, 2011.

[103] J. M. Palmer, "Pre-growth structures for high quality epitaxial graphene nanoelectronics grown on silicon carbide," PhD thesis, Georgia Institute of Technology, 2014.

[104] V. Prudkovskiy, K. Katin, M. Maslov, P Puech, R. Yakimova, and G Deligeorgis, "Efficient cleaning of graphene from residual lithographic polymers by ozone treatment," *Carbon*, vol. 109, pp. 221–226, 2016.

[105] M. Her, R. Beams, and L. Novotny, "Graphene transfer with reduced residue," *Physics Letters A*, vol. 377, no. 21-22, pp. 1455–1458, 2013.

[106] K. Kumar, Y.-S. Kim, and E.-H. Yang, "The influence of thermal annealing to remove polymeric residue on the electronic doping and morphological characteristics of graphene," *Carbon*, vol. 65, pp. 35–45, 2013.

[107] Z. Cheng, Q. Zhou, C. Wang, Q. Li, C. Wang, and Y. Fang, "Toward intrinsic graphene surfaces: A systematic study on thermal annealing and wet-chemical treatment of sio2-supported graphene devices," *Nano letters*, vol. 11, no. 2, pp. 767–771, 2011.

[108] L. Ponomarenko, R. Gorbachev, G. Yu, D. Elias, R Jalil, A. Patel, A Mishchenko, A. Mayorov, C. Woods, J. Wallbank, *et al.*, "Cloning of dirac fermions in graphene superlattices," *Nature*, vol. 497, no. 7451, p. 594, 2013.

[109] C. Dean, L Wang, P Maher, C Forsythe, F Ghahari, Y Gao, J Katoch, M Ishigami, P Moon, M Koshino, *et al.*, "Hofstadters butterfly and the fractal quantum hall effect in moiré superlattices," *Nature*, vol. 497, no. 7451, p. 598, 2013.

[110] J. V. Gigliotti, "Integrated dielectrics for protection and gating of epitaxial graphene devices," PhD thesis, Georgia Institute of Technology, 2017.

[111] M. Kruskopf, K. Pierz, S. Wundrack, R. Stosch, T. Dziomba, C.-C. Kalmbach, A. Müller, J. Baringhaus, C. Tegenkamp, F. J. Ahlers, *et al.*, "Epitaxial graphene on sic: Modification of structural and electron transport properties by substrate pretreatment," *Journal of Physics: Condensed Matter*, vol. 27, no. 18, p. 185 303, 2015.

[112] V. Borovikov and A. Zangwill, "Step bunching of vicinal 6h sic (0001) surfaces," *Phys. Rev. B*, vol. 79, p. 245 413, 24 2009.

[113] A. R. Powell and L. B. Rowland, "Sic materials-progress, status, and potential roadblocks," *Proceedings of the IEEE*, vol. 90, no. 6, pp. 942–955, 2002.

[114] W. A. De Heer, C. Berger, M. Ruan, M. Sprinkle, X. Li, Y. Hu, B. Zhang, J. Hankinson, and E. Conrad, "Large area and structured epitaxial graphene produced by confinement controlled sublimation of silicon carbide," *Proceedings of the National Academy of Sciences*, vol. 108, no. 41, pp. 16 900–16 905, 2011.

[115] J. Hass, F. Varchon, J. E. Millán-Otoya, M. Sprinkle, N. Sharma, W. A. de Heer, C. Berger, P. N. First, L. Magaud, and E. H. Conrad, "Why multilayer graphene on 4h sic(000-1) behaves like a single sheet of graphene," *Phys. Rev. Lett.*, vol. 100, p. 125 504, 12 2008.

[116] P. Poncharal, A. Ayari, T. Michel, and J.-L. Sauvajol, "Effect of rotational stacking faults on the raman spectra of folded graphene," *Phys. Rev. B*, vol. 79, p. 195 417, 19 2009.

[117] B. Partoens and F. M. Peeters, "From graphene to graphite: Electronic structure around the k point," *Phys. Rev. B*, vol. 74, p. 075 404, 7 2006.

[118] I. Palacio, A. Celis, M. N. Nair, A. Gloter, A. Zobelli, M. Sicot, D. Malterre, M. S. Nevius, W. A. De Heer, C. Berger, *et al.*, "Atomic structure of epitaxial graphene sidewall nanoribbons: Flat graphene, miniribbons, and the confinement gap," *Nano letters*, vol. 15, no. 1, pp. 182–189, 2014.

[119] A. Celis, M. Nair, A. Taleb-Ibrahimi, E. Conrad, C. Berger, W. de Heer, and A. Tejeda, "Graphene nanoribbons: Fabrication, properties and devices," *Journal of Physics D: Applied Physics*, vol. 49, no. 14, p. 143 001, 2016.

[120] V. Borovikov and A. Zangwill, "Step-edge instability during epitaxial growth of graphene from sic (0001)," *Physical Review B*, vol. 80, no. 12, p. 121 406, 2009.

[121] F. Ming and A. Zangwill, "Phase field modeling of submonolayer epitaxial growth," *Physical Review B*, vol. 81, no. 23, p. 235 431, 2010.

[122] ——, "Model for the epitaxial growth of graphene on 6 h-sic (0001)," *Physical Review B*, vol. 84, no. 11, p. 115 459, 2011.

[123] ——, "Model and simulations of the epitaxial growth of graphene on non-planar 6h–sic surfaces," *Journal of Physics D: Applied Physics*, vol. 45, no. 15, p. 154 007, 2012.

[124] M. Hupalo, E. H. Conrad, and M. C. Tringides, "Growth mechanism for epitaxial graphene on vicinal 6h sic (0001) surfaces: A scanning tunneling microscopy study," *Phys. Rev. B*, vol. 80, p. 041 401, 4 2009.

[125] A Nakajima, H Yokoya, Y Furukawa, and H Yonezu, "Step control of vicinal 6h–sic (0001) surface by h 2 etching," *Journal of applied physics*, vol. 97, no. 10, p. 104 919, 2005.

[126] S. Nie, C. Lee, R. M. Feenstra, Y Ke, R. Devaty, W. Choyke, C. Inoki, T. Kuan, and G. Gu, "Step formation on hydrogen-etched 6h-sic (0 0 0 1) surfaces," *Surface Science*, vol. 602, no. 17, pp. 2936–2942, 2008.

[127] W. Norimatsu and M. Kusunoki, "Growth of graphene from sic (0001) surfaces and its mechanisms," *Semiconductor Science and Technology*, vol. 29, no. 6, p. 064 009, 2014.

[128] J Baringhaus, J Aprojanz, J Wiegand, D Laube, M Halbauer, J Hübner, M Oestreich, and C Tegenkamp, "Growth and characterization of sidewall graphene nanoribbons," *Applied Physics Letters*, vol. 106, no. 4, p. 043 109, 2015.

[129] M Topsakal and S Ciraci, "Domain formation on oxidized graphene," *Physical Review B*, vol. 86, no. 20, p. 205 402, 2012.

[130] X. Yu, C. Hwang, C. M. Jozwiak, A Köhl, A. K. Schmid, and A. Lanzara, "New synthesis method for the growth of epitaxial graphene," *Journal of Electron Spectroscopy and Related Phenomena*, vol. 184, no. 3-6, pp. 100–106, 2011.

[131] C. Celebi, C. Yanık, A. G. Demirkol, and I. I. Kaya, "The effect of a sic cap on the growth of epitaxial graphene on sic in ultra high vacuum," *Carbon*, vol. 50, no. 8, pp. 3026–3031, 2012.

[132] J. Palmer, J. Kunc, Y. Hu, J. Hankinson, Z. Guo, C. Berger, and W. A. de Heer, "Controlled epitaxial graphene growth within removable amorphous carbon corrals," *Applied Physics Letters*, vol. 105, no. 2, p. 023 106, 2014.

[133] T. Ohta, N. C. Bartelt, S. Nie, K. Thürmer, and G. Kellogg, "Role of carbon surface diffusion on the growth of epitaxial graphene on sic," *Physical Review B*, vol. 81, no. 12, p. 121 411, 2010.

[134] J Tersoff, D. Jesson, and W. Tang, "Running droplets of gallium from evaporation of gallium arsenide," *Science*, vol. 324, no. 5924, pp. 236–238, 2009.

[135] C. Beenakker and H. van Houten, "Quantum transport in semiconductor nanostructures," in *Solid state physics*, vol. 44, Elsevier, 1991, pp. 1–228.

[136] A. C. Ferrari and J. Robertson, "Interpretation of raman spectra of disordered and amorphous carbon," *Physical review B*, vol. 61, no. 20, p. 14 095, 2000.

[137] D. Tsang and M. Dresselhaus, "The c-axis electrical conductivity of kish graphite," *Carbon*, vol. 14, no. 1, pp. 43–46, 1976.

[138] C. G. Willson, R. R. Dammel, and A. Reiser, "Photoresist materials: A historical perspective," in *Metrology, Inspection, and Process Control for Microlithography XI*, International Society for Optics and Photonics, vol. 3050, 1997, pp. 38–52.

[139] S. Lilov, "Study of the equilibrium processes in the gas phase during silicon carbide sublimation," *Materials Science and Engineering: B*, vol. 21, no. 1, pp. 65–69, 1993.

[140] "Lateral force microscopy (lfm)," *Park AFM*, Topology in Condensed Matter, Course Materials, Readings, Accessed: 2018-01-25.

[141] E. Panizon, R. Guerra, and E. Tosatti, "Ballistic thermophoresis of adsorbates on free-standing graphene," *Proceedings of the National Academy of Sciences*, vol. 114, no. 34, E7035–E7044, 2017.

[142] J. H. Hankinson, "Spin dependent current injection into epitaxial graphene nanoribbons," PhD thesis, Georgia Institute of Technology, 2015.

VITA

”I’ve found a remarkable proof of this fact, but there is not enough space in the margin to write it.”

Pierre De Fermat

”[Galois’] argument is neither sufficiently clear nor sufficiently developed to allow us to judge its rigor” – ”We would then suggest that the author should publish the whole of his work in order to form a definitive opinion.”

Comments of Simeon Denis Poisson in the rejection letter of Evariste Galois’ paper.